CRYSTALLIZATION OF MAGNESIUM SIALON LIQUIDS AND GLASSES.

by Graeme Leng-Ward

A thesis submitted to the Council for National Academic Awards for the degree of Doctor of Philosophy.

Sponsored by the Polytechnic of Wales, Pontypridd, Mid-Glamorgan, in collaboration with Lucas Syalon Limited.

March 1983.

CONTENTS.

CHAPTER SIX.

DIFFRACTION STUDIES OF β"-MAGNESIUM SIALON.

. . .

List of Figures.

List of Tables.

. . .

Acknowledgements.

I sincerely thank Dr.S.Wild for his encouragement and enthusiasm during the supervision of this work.

My sincere gratitude to Dr.M.H.Lewis for his guidance in TEM techniques and discussions which greatly contributed to this work.

My thanks are also due to:

Mr R.J.Lumby for the supply of silicon nitride powder, discussions, and visit to Lucas Industries.

Miss C.Tyndall, Mr R.Jenkins and Mr B.Minty of the Polytechnic of Wales for their help in SEM and X-ray diffraction work, and Mr.R.Thornton for guidance with the word processor.

Mr G.Smith and Mr M.Thornton , Physics Department, Warwick University, for help in preparing specimens and operating the TEM.

Declaration.

I declare that, with the exception of the assistance acknowledged, this thesis is a result of my own studies.

This thesis has not been accepted for any other award or degree and is not concurrently being submitted in candidature for any other award or degree.

Signed: Graeme Lengthward

Date: 1/3/83

Abstract.

CRYSTALLIZATION OF MAGNESIUM SIALON LIQUIDS AND GLASSES.

by Graeme Leng-Ward.

Previous reports on the solubility of magnesium in β'-sialons have been conflicting. The present work shows conclusively that metastable crystalline β"-magnesium sialons do exist and can be formed by two distinct crystallization mechanisms:

(1) Low temperature annealing of quenched MgSiAlON (3M/4X) glasses containing precipitated β-Si_3N_4/β'sialon nuclei which must be present for epitaxial nucleation and growth to proceed. The degree of β" crystallization which can be achieved is sensitive to both composition and impurity levels and complete crystallization (>90%) can be achieved only for compositions within the 3M/4X plane using high purity starting materials.

(2) Coupled growth with forsterite from MgSiAlON (3M/4X) liquids producing low magnesium content β" in a 'eutectic' microstructure.

β"-magnesium sialons have a range of compositions within the 3M/4X plane of the Mg-Si-Al-O-N system, with compositions of high magnesium content tending to exist in a limited composition range indicative of a 'phenacite' type metal atom ordering between (Mg,Al) and Si, as confirmed by the existence of additional 'superlattice' reflections in electron diffraction photographs.

The metastable nature of B"-magnesium sialons means that they tend to transform to stable crystalline products at high temperatures. The range of β" composition gives a corresponding range of thermal stability, with high magnesium content β" stable only up to 1120 ^{o}C, while B" crystals with lower magnesium levels are able to exist up to 1350^{o}C.

A previously unknown MgSiAlON phase, termed Q-phase, has been crystallized as a secondary phase from MgSiAlON liquids in the 3M/4X plane in association with forsterite.

. . .

CHAPTER ONE.

SILICON NITRIDE CERAMICS.

1.1 GENERAL.

During the past twenty years silicon nitride has received considerable attention as a potential high temperature structural material because of its excellent combination of thermal, chemical and mechanical properties. Its intrinsic properties ie. low thermal expansion and moderate elastic modulus, minimize stresses developed during severe thermal transients and its thermal shock properties are therefore better than many other ceramics (1,2,3)

There are major difficulties in sintering Si_3N_4 to full density. Si_3N_4 is a covalently bonded solid (~70% covalency) and consequently a large amount of energy is required for the formation and motion of structural defects which permit sintering by diffusion. Deeley et al (4) found that densification could be accomplished by hot pressing Si_3N_4 powders containing an MgO densification aid. Terwilliger and Lange (5) showed that Si_3N_4 powder together with 5 wt% MgO could be pressureless sintered to high density in the temperature range 1500-1700^oC using long sintering periods at the lower temperature or short sintering periods at the higher temperatures. At above 1700^oC decomposition occurs and weight losses prevent complete sintering (5,6).

Wild et al (7) suggested a liquid-phase sintering mechanism in their discussion of the role of MgO additions in hot pressed Si_3N_4, the liquid being a nitrogen containing magnesium silicate liquid. Densification of Si_3N_4 powder containing an additive is generally attributed (6) to the presence of a liquid formed by the reaction of

all the constituents above a eutectic temperature, ie.

$$Si_3N_4 + y\ SiO_2 + z\ (\text{metal oxide}) + \text{impurities}$$

$$\text{-------}\rightarrow \quad (1-x)\ Si_3N_4 + (x+y+z)\ \text{liquid.} \qquad . \ . \ .(1)$$

(SiO_2 is normally present in the Si_3N_4 powder as a surface layer on each Si_3N_4 particle).

Jack and Hampshire (11) suggested that the liquid promotes densification via the following stages (using Kingery's model of liquid-phase sintering);

(i) particle rearrangement --- where the rate and extent of shrinkage depends upon the viscosity and volume of liquid, and then ;

(ii) solution-precipitation mechanism --- involving solution of the less stable, more soluble α-Si_3N_4 starting powder and its precipitation (11,12) as the less soluble, more stable β'-Si_3N_4, followed by,

(iii) coalescence --- involving elimination of closed porosity.

Thus the liquid acts as a flux by which pores are removed and provides a medium which facilitates diffusion and mass transport during the $\alpha \rightarrow \beta$ transformation. The temperature of liquid formation, the viscosity of the liquid, and the degree of wetting by the liquid will vary with different additives. Hence the relative contributions to the densification process of stages (i) and (ii) will vary (9,11). Many compounds have been found to act as suitable densification aids, the most effective being MgO, Y_2O_3 and CeO_2 (8,9,10).

Upon cooling the residual oxynitride liquid solidifies forming an

intergranular glassy phase. This has been clearly demonstrated by a number of workers. For example Drew and Lewis (13), using TEM on thin films of hot pressed Si_3N_4 with MgO additions, have shown that many grains are adjacent to a small volume of non-crystalline phase, the amount of the latter decreasing with decreasing amounts of MgO. These observations support earlier work of a similar nature by Evans and Sharp (14). More recent work by Clarke and Thomas (15) employing high resolution TEM lattice fringe imaging has shown that a thin (10-20 $\mathring{A}$) glassy phase exists between most Si_3N_4 grains in many different Si_3N_4 systems. Lou et al (16), in a similar study claim that the glassy phase forms a continuous grain boundary film surrounding all of the grains. The presence of this intergranular glass unfortunately has a deleterious effect on the high temperature strength of the material (7,17).

Krivanek et al (18) found that the experimentally determined yield temperatures for two commercial hot pressed and two sintered silicon nitrides correlated with the estimated softening temperatures of the intergranular glass compositions, which is clear evidence for the central role played by glassy phases in determining the high temperature mechanical properties of these materials.

In particular, the reduction in the fracture strength at high temperatures seems to be caused by the sub-critical growth of inherent flaws in the material due to stress-enhanced grain boundary sliding at the flaw tip (20). Grain boundary sliding also causes the material to creep under an applied stress at high temperatures (21,22). The rate of grain boundary sliding at a given temperature is inversely related to the viscosity of the grain boundary glass phase, so that impurities such as Ca which concentrate in the residual glass and lower its viscosity have a deleterious effect on the material's mechanical

properties (23).

The lower additive levels needed to manufacture a fully dense Si_3N_4 solid by hot pressing compared with pressureless sintering (1 to 5 wt% for hot pressing and 5-15 wt% for pressureless sintering (18)), mean that hot pressing gives a superior product because there is less residual glass phase. Larger additive levels are necessary in pressureless sintering in order to provide a sufficient volume of the sintering liquid at temperature, whereas densification may be achieved under pressure with a smaller liquid volume. Because only simple shapes can be fabricated by hot pressing and more complex shapes require very expensive machining on diamond impregnated wheels, much effort is being directed to develop pressureless sintering techniques in order to produce engineering materials at a realistic economic level.

With pressureless sintering volatilization has presented serious problems in both controlling the composition of the reaction products and in achieving satisfactory densification, although, Popper et al. (19) have shown that these problems can be partly resolved by embedding the powder compacts in a suitable powder bed.

The possibility of having better control of the amount and composition of the intercrystalline phase, has been realized following the discovery by Jack and Wilson (24) and Oyama (25) of highly substituted β-Si_3N_4 materials. These materials are formed by reacting Si_3N_4 with Al_2O_3 and AlN, and, also normally involve the presence of sintering aids such as yttria and magnesia. Investigations of the high temperature chemistry and the phase relationships in such complex multicomponent systems requires a clear and systematic method of representing all the possible compositions which can occur within the system. . .

1.2 REPRESENTATION OF MULTICOMPONENT SILICON NITRIDE BASED SYSTEMS.

Gauckler et al (26) were the first to point out that the phase relations should be considered in terms of reciprocal salt reactions. Reciprocal salt systems are mixtures of components containing at least two cations (A,B) and two anions (X,Y). Such a reciprocal reaction for the Si-M-O-N four component system (6) is :

$$Si_3N_4 + \frac{6}{a}MO_{2a} \rightarrow 3SiO_2 + \frac{4}{a}M_aN_3 \quad \ldots (2)$$

where a = metal's valence state, and, where each element exhibits only its normal valency state.

The reaction products can be represented in the Si_3N_4-SiO_2-M_2O_a-M_3N_a pseudoternary system.

1.2.1 Si-Al-O-N system.

In fig 1.1 the quaternary Si-Al-O-N system is represented as a tetrahedron with the binary compounds located along the metal:non-metal joins. Using atomic % as concentration units, the pseudo-ternary system Si_3N_4-SiO_2-Al_2O_3-AlN is an irregular quadrilateral fig 1.1 (a). Assuming the valencies . Si(+4), Al(+3), O(-2), N(-3) do not change, all phases existing in equilibrium are in this plane. Using equivalent % as concentration units, as is common with reciprocal salt systems, the Si_3N_4-SiO_2-Al_2O_3-AlN pseudoternary system is conveniently a square plane, fig 1.1 (b). This reciprocal pseudoternary system can be plotted on a square, as shown in fig 1.2 (a), with Si_3N_4 at the origin and the equivalent % Al and the equivalent % O along the abscissae. Any composition point within the square is made up of a combination of 12 +ve and 12 -ve valencies.

1.2.2 Mg-Si-Al-O-N System.

The five component Mg-Si-Al-O-N system can be treated as a pseudoquaternary reciprocal salt system. A projection of the four dimensional concentration zone (27) is shown in fig 1.1 (c) with the binary compounds located on the metal:non-metal joins. The system can be represented as a regular triangular prism, based on the Si_3N_4-Si_3O_6-Al_4O_6-Al_4N_4 square with Mg in equivalent units along a third dimension, see fig 1.2 (b). The two triangular faces represent the oxide and nitride ternary systems.

. . .

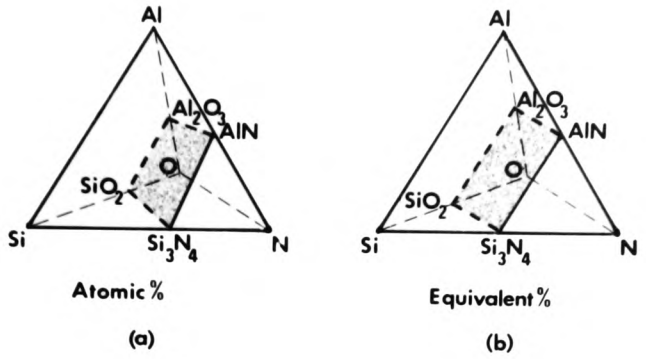

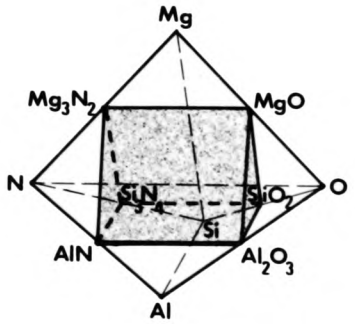

Figure 1.1

(a,b) The quaternary system Si-Al-O-N with the pseudoternary system Si_3N_4-AlN-Al_2O_3-SiO_2, after Gauckler and Petzow (27).

(c) The quinary Mg-Si-Al-O-N system with the pseudo-quaternary system MgO-Mg_3N_2-Si_3N_4-AlN-Al_2O_3-SiO_2 after Gauckler and Petzow (27).

1.3 SYSTEMS SHOWING β-Si N SOLID SOLUBILITY.

----------3-4----------

The range of high temperature materials based on Si_3N_4 has increased considerably following the discovery (24,25) that Al(+3) can substitute for Si(+4) in the β-Si_3N_4 lattice, with charge neutrality being maintained by the simultaneous replacement of N(-3) by O(-2). The solid solution produced, termed β'-sialon, has its composition given by the 'z-formula' (28):

$$Si_{6-z}Al_z\ O_z\ N_{8-z} \qquad . \quad . \quad .(3)$$

with z ranging from 0 to 4.2 (Jack (32) and Gauckler (26)).

The degree of metal atom and non-metal substitution is such that a metal atom to non-metal atom ratio (referred to as M/X in the text) of 3:4 is always maintained within the β' lattice. As the Si atoms are replaced by the larger aluminium atoms the hexagonal unit cell dimensions increase from,

$a=7.61$ Å, $c=2.91$ Å for z=0

to $a=7.71$ Å, $c=3.00$ Å for z=4.2

The isothermal behaviour diagram of the Si_3N_4-AlN-Al_2O_3-SiO_2 system at 1750°C is shown in fig 2 (a) , with β' representing β'-sialon.

β'-sialon materials can be formed by either hot pressing or pressureless sintering mixtures of Si_3N_4, AlN, SiO_2 and Al_2O_3 in the appropriate proportions taking into account the surface layer of SiO_2 usually present on the Si_3N_4 particles. Lewis et al (30) demonstrated that densification is facilitated by the formation of a liquid phase formed by an initial reaction between SiO_2 and Al_2O_3 at 1600°C. It was initially thought that, if the composition was perfectly balanced according to the z-formula, all the liquid phase should disappear just when the reaction is finished (9) giving a single phase β'-sialon with

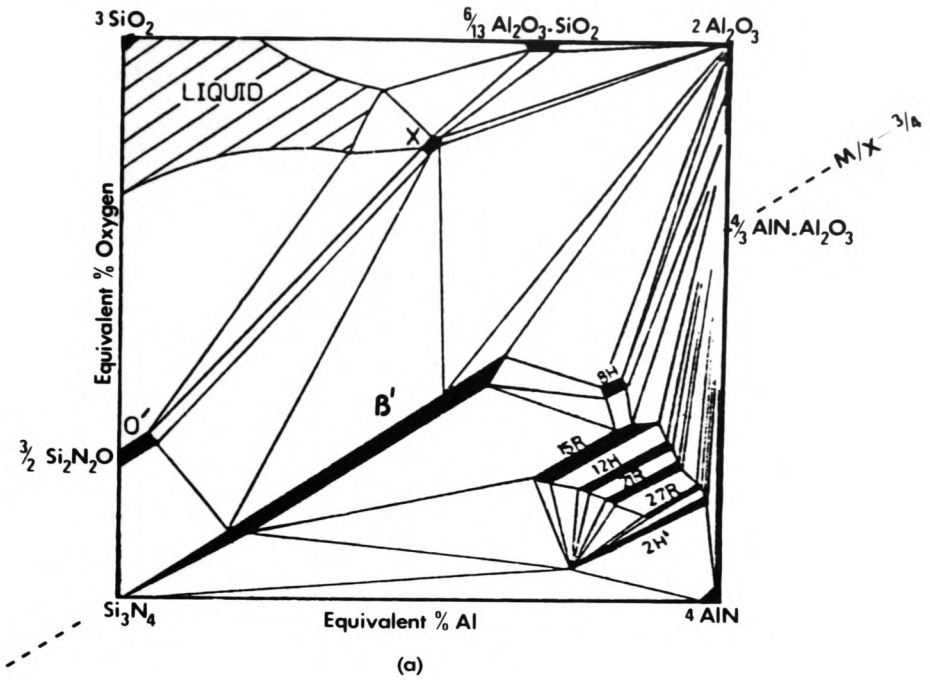

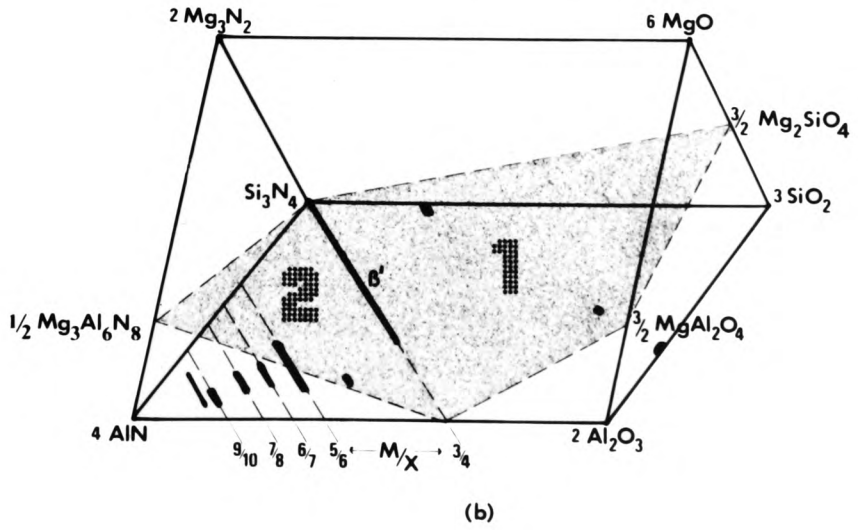

Figure 1.2

(a) Isothermal section of the system Si_3N_4-SiO_2-Al_2O_3-AlN (29), 1750°C

(b) The Mg-Si-Al-O-N system represented in 'equivalents' as a regular triangular prism (with the substitutional 3M/4X composition plane shaded 1, and the possible interstitial solid solution composition plane shaded 2).

no residual phases. However 'balanced' compositions have proved to be very difficult to densify because of:

(i) The progressive reduction in the liquid volume available to promote densification as the 'balanced' composition is approached,

(ii) The high viscosity of the liquid alumino-silicates meaning that very high temperatures are required to promote densification.

Densification can, however, be achieved at lower temperatures by using an additive such as MgO that forms a low viscosity nitrogen containing liquid Mg-alumino-silicate, and is found to markedly enhance densification. The α-Si_3N_4 --> β'-sialon transformation is similar to that discussed previously with the α-Si_3N_4 phase dissolving in the liquid and precipitating as β'-sialon.

In order to achieve ease of densification together with low residual phase content, the possibility of using an additive which is soluble in the β'-sialon structure must be considered. An ideal situation (see Lewis et al (31) and Jack (32)), would be the initial formation of a liquid phase to facilitate densification followed by suitable heat treatment in order either to :

(i) incorporate the components of the liquid into solid solution in the silicon nitride, or

(ii) crystallize out the grain boundary glass as a multicomponent β'metal sialon.

Two necessary criteria for achieving this goal are:

(A) The existence of a liquid phase with composition M_3X_4.

(B) The ability of the additional metal and non-metal atoms to substitute for, respectively, Si and N in the β'-Si_3N_4 structure.

The Si-Al-O-N system only satisfies the second criteria as the liquid region does not extend across the 3M:4X line as shown in fig 1.2 (a).

The five component Mg-Si-Al-O-N system does have an extensive liquidus region in the 3M/4X plane (see fig 1.4 a). However the evidence for the existence of β'-magnesium sialons is highly conflicting. Direct substitution of Mg for Si and Al would give rise to β'-magnesium sialons in the 3M/4X composition plane with the general formula :

$$Mg_{m/2}\ Si_{6-z+m/2}\ Al_{z-m}\ O_z\ N_{8-z} \qquad \ldots (4)$$

Jack (34) claims primarily from X-ray diffraction analysis, that there is a significant degree of Mg substitution in the β'-sialon structure ; giving an example of a β'-Mgsialon with unit cell dimensions of $a=7.79\ \mathring{A}$ and $c=3.05\ \mathring{A}$, approximately 4% greater than the limiting x=4.2 sialon. However Gauckler et al (35) claim that under the conditions studied (hot pressing at 1700°C), very little or no magnesium enters the β' lattice (ie. substitution must be if any, less than 1.5 at%.). Work by Lewis et al (36) on the crystallization of Mg-containing phases in β'-sialon ceramics tends to support Gauckler's findings. Using TEM and EDAX Lewis claims that Mg shows only a very small solubility in β'sialon crystals (just detectable above the background in the EDAX spectrum), and is mainly segregated in the glassy 'matrix' phase.

It is also possible that Mg enters the β' lattice forming an interstitial solid solution, with Al(+3) replacing the Si(+4) in tetrahedral sites and positive charge deficiences compensated for by incorporating Mg (+2) in interstitial sites. If formed this would give

rise to compositions with the general formula :

$$Mg_{x/2}\ Si_{6-x-z}\ Al_{x+z}\ O_z\ N_{8-z} \quad \ldots (5)$$

These compositions lie in the second shaded triangular composition plane shown in fig 1.2 (b). However Gauckler found no evidence for the existence of interstitial solid solution or for a combination of interstitial/substitutional solid solution.

Evidence for beryllium solubility in the β-Si_3N_4 lattice was reported by Huseby et al (8) and Jack (34). Huseby et al (37) using X-ray diffraction analysis concluded that the solubility limit of Be in β-Si_3N_4 at 1780°C for the composition,

$$Si_{6-m/2}\ Be_{m/2}\ O_m\ N_{8-m} \quad \ldots (6)$$

is given by m ~ 1.44 and decreases to m ~ 0.92 at 1880°C. As Be and O are both smaller than Si and N respectively, the simultaneous substitution of Be and O for respectively Si and N in β-Si_3N_4 produces a decrease in the hexagonal unit cell dimensions. Working with the Si-Be-O-N system Greskovich (38) reported the preparation of single phase, hot pressed β'-SiBeON ceramics using high purity Si_3N_4 powder and a small amount of Be_3N_2 or $BeSiN_2$ as a densification aid. However use of the lattice fringe technique has revealed that these do contain a thin (15 Å) continuous second phase, probably glass, at some grain boundaries and triple points.

There is no reliable evidence in four component systems of any cations other than Al and Be substituting for Si, and if the system is extended to five components where four of the components are Si, Al, O and N , the fifth component may be Be (27), or Ga (39). Jack has reported (34) that there is extensive beryllium solubility in β'-

sialons. However beryllium is unsuitable for general use in ceramics because of its very high toxicity.

Over the past few years numerous workers have attempted to fabricate single phase silicon nitride materials without the presence of any residual glassy phase, but so far there are no unequivocal reports of such materials being produced. As well as the criteria already suggested as necessary for the formation of single phase B' material another factor of major importance in achieving this goal is that of maintaining complete control of the composition during the fabrication process. This is normally very difficult because of,

(i) Impurities in the starting powders (eg. variable oxygen content in Si_3N_4 powders (40), Ca which is too large to be incorporated into the B'sialon structure (13,50), impurity pick up during processing (41)).

(ii) Volatilization of components during firing (8).

(iii) The present lack of a suitable multicomponent system possessing a liquid in the 3M/4X plane.

The most effective way of approaching the fabrication of a single-phase B'-sialon ceramic is by hot-pressing a carefully balanced Si-Al-O-N composition with a small amount of Mg-additive so that the residual glass boundary exists as just a thin layer between adjacent B'-sialon grains and not at triple junctions (31). However, for fabrication by pressureless sintering, the larger volume of liquid sintering aid necessary means that such ceramics are essentially two phase materials.

Another approach would be to use an additive that promotes densification and also enables the resulting residual glassy phase to

be crystallized, not necessarily into a multicomponent B'metal-sialon, but into a secondary refractory grain boundary phase. This might alleviate the high temperature problems associated with viscous creep. In 1973 Gazza suggested (42) ; 'In considering the refractory boundary approach, the amount of additive required should be optimized rather than minimized'.

This represents a different concept in producing silicon nitride ceramics - fabricating a polyphase material rather than attempting to produce a 'pure' single phase one.

. . .

1.4 POLYPHASE SI-Al-O-N BASED MATERIALS.

In the past there has tended to be a concentration on developing high purity single phase polycrystalline materials- Al_2O_3, $MgAl_2O_4$, MgO, Si_3N_4, etc. However in many cases (43) it is possible that , compared with single-phase products, two or more phases may have the desired properties and offer more flexible preparation routes.

The use of Si-Al-O-N based compositions, rather than Si_3N_4 based, is important enabling a greater flexibility in choice of second phase composition than for materials with only Si, N, and some O impurity (see Lewis et al (31)). The fabrication of B'-sialon ceramics involves making the best compromise between the 'ease of processing' and the 'optimum high temperature mechanical properties' requirement of the product. The 'ease of processing' requirement involves using a reaction sintering process in order to fabricate complicated shapes and this in turn necessitates the presence of a liquid phase (via a suitable sintering additive) in order to give efficient densification at the firing temperature. The best compromise (31) between 'ease of

processing' and 'good high temperature properties' is likely to be achieved with an additive (or additives) which promotes crystallization of the residual phase and/or increases the viscosity of any remaining glass. However increased viscosity in the residual phase may reflect an undesirable increase in liquid-phase viscosity during processing, resulting in more difficult densification.

For low temperature applications the 'optimum high temperature property' factor could be relaxed in favour of the 'ease of processing' factor, and the material could be prepared with a large liquid content for improved sinterability.

Gazza (42) showed that Si_3N_4 could be hot pressed to a high density using Y_2O_3 rather than MgO as the densification aid. The material produced by this method has a higher strength at elevated temperatures, as the grain boundary phase in this case is a yttrium silicate glass which is more refractory than a magnesium silicate glass.

Tsuge et al (44) showed that the high temperature strength of Si_3N_4 containing 5wt % Y_2O_3 is improved by crystallizing the glass phase to form a refractory hard grain boundary phase of Si_3N_4 .Y_2O_3. Rae et al (45) found that yttrium oxide additions of greater than 10wt % to Si_3N_4 produce a series of reactions during hot pressing which lead to the formation of a crystalline yttrium silicon oxynitride (Si_3N_4 .Y_2O_3) as the final grain boundary phase. This gives the material an improved high temperature strength and creep resistance, however the thermal expansion coefficient of the yttrium silicon oxynitride is approximately twice that of β-Si_3N_4 (44) so that its presence at Si_3N_4 grain boundaries may lead to a highly stressed material with a poor resistance to thermal shock (46).

The secondary phases in many Si_3N_4 systems readily oxidize at temperatures where the oxidation of the Si_3N_4/sialon is negligible (~1000°C) (47). Polyphase materials in the Y-Si-O-N system containing $Si_3N_4.Y_2O_3$ as a secondary phase were observed to crack apart after oxidation periods at 1000°C, caused by the stresses arising from the large molar volume change (30%) occuring with the oxidation of this secondary phase to $Y_2Si_2O_7 + SiO_2$. It was found that this problem could be averted by fabricating compositions within the Si_3N_4-Si_2ON_2-Y_2O_7 compatibility triangle where formation of unstable secondary phases is avoided, and giving the most advantageous high temperature mechanical properties and oxidation resistance observed to date for Si_3N_4 alloys (47).

Lewis et al (31) pressureless sintered Si-Al-O-N compacts containing large Y_2O_3 additive concentrations. The resulting material, of near theoretical density, contained β'-sialon and a Y/Al rich 'silicate' glassy matrix in the 'as-sintered' condition. This matrix can be crystallized on heat treatment to a Si-substituted yttrium-aluminium garnet phase and the resulting material has mechanical and thermal properties comparable with the better hot-pressed sialon and Si_3N_4 ceramics, although oxidation problems are a limitation on this phase material for very high temperatures of 1300-1450°C.

Working with the Mg-Si-Al-O-N system, Weston et al (48) attempted to design a grain boundary phase for a hot pressed Si_3N_4 using a multicomponent oxide mixture as a densification aid. The additive composition was chosen to give a liquid at fabrication temperature that cools to a glass which by a suitable heat treatment fully crystallizes to cordierite, a phase they considered to be compatible with β-Si_3N_4 (ie. similar thermal expansion coefficients). However they could only

partially crystallize their grain boundary phase, with the crystalline phases produced being magnesium silicates (Mg_2SiO_4 and $MgSiO_3$) instead of cordierite ($Mg_2Al_4Si_5O_{18}$). This is because the phase relations in the 'additive only' system are considerably different from those in the 'Si_3N_4 + additive' system. No account was taken of the possibility that some of the Al and O of the additive formulation would form a solid solution with the Si_3N_4, and that the eutectic composition for the whole system , and hence the composition of the last bit of liquid to solidify (49), might be considerably different from the 'additive only' system.

Lewis et al (36) sintered an Mg-Si-Al-O-N (3M/4X) composition ceramic which contained a Si-substituted spinel as the most prominent second phase, but found that its properties were easily surpassed in sintered sialon ceramics prepared with large Y_2O_3 additions.

Clarke suggested (50) that a preliminary step in the evaluation of a new material should be an examination that determines whether the material contains an intergranular phase and, if so, its composition. By fabricating this composition, the high temperature properties (ie. glass transition temperature and viscosity in the case of a glassy phase or the eutectic temperature if it is crystalline) of the intergranular phase itself may be established. An understanding of what constitutes an unsatisfactory grain boundary phase is currently not well developed, however from the literature it is clear that the design of a grain boundary phase (51) should involve the following considerations :

(a) Crystallization must take place from a liquid that wets the sialon particles and so allows densification to take place.

(b) To fully crystallize the residual liquid its composition must lie within the stoichiometric range of the crystalline product/s.

(c) Crystallization of the residual liquid should take place without a large specific volume change that could produce internal stresses.

(d) Secondary phases should have thermal expansion coefficients similar to that of β-Si_3N_4/β'-sialon.

(e) Secondary phases should have good mechanical properties, or properties complementary to β-Si_3N_4/β'-sialon.

(f) Secondary phases should be compatible with SiO_2, the oxidation product of Si_3N_4.

The effective crystallization of the residual liquid requires close control of the liquid composition following densification, but, this compositional control may not be as critical as that required for producing a single phase product.

Following densification , if the specimen is cooled very rapidly by quenching, then the residual liquid present at fabrication temperature (composition Q) will be 'frozen' in as a glass with composition Q. However on slow cooling (49), as is usual, secondary phases may crystallise out of the residual liquid according to the subsolidus phase relations of the system, leaving the last bit of liquid to solidfy at the eutectic temperature as a glass with composition E (ie. the eutectic composition). Intermediate cooling rates will tend to give final grain boundary glass compositions intermediate between Q and E, but tending towards E (ie. a 'near eutectic' composition) as the cooling rate decreases. It is the control of these final oxynitride glass compositions which is the key to obtaining a fully crystalline grain boundary phase.

In view of the impact that the oxynitride glass boundary phase has on the properties of silicon nitride ceramics, there is clearly a need to obtain a greater understanding of the properties of these glasses.

. . .

1.5 OXYNITRIDE GLASSES.

1.5.1 Introduction.

The incorporation of nitrogen in glass was initially demonstrated by Mulfinger and Mayer (52,53), who reported in the early 1960's on the physical and chemical solubility of nitrogen in a variety of glass melts containing soda, silica, lime and boric acid. Mulfinger and Franz (54) showed that chemically dissolved nitrogen existed in the glass structure either as N-H groups or as dissolved nitrides. Small concentrations of nitrogen in oxide glasses , less than 1 at%, were reported (53,55,56) to make significant changes in glass properties, eg. increasing the softening temperature, viscosity, and resistance to devitrification.

The first suggestion that nitrogen was involved in fairly extensive oxynitride glass formation was made by Jack (32), reporting the accomodation of up to 10 at% in glasses, eg. in the Mg-Si-Al-O-N and Y-Si-Al-O-N systems. He noted that in Si_3N_4 there is a tetrahedral array of nitrogens around a central silicon, similar in structure to the SiO_4 tetrahedron in silicate glasses. The Si-N (1.74 Å), Si-O (1.62 Å), Al-O (1.75 Å) tetrahedral bond lengths (59,68) are all reasonably similar implying that on the basis of size alone there could be substitution of nitrogen for oxygen in silicate and aluminosilicate glasses.

Nitrogen, being trivalent, can link to three silicons, as compared

with a maximum of two silicons in the case of oxygen. This enables nitrogen to confer a degree of cross linking (53) in the glass structure not possible in pure oxides. This is illustrated in Risbud's (57) schematic two dimensional view of the network structure of an oxynitride glass in the Si-Metal-O-N system as shown in fig 1.3.

Recent research by Shillito et al (58), Loehman (59), and Jack et al (60) on several M-sialon glasses (M=Mg,Ca,Y,Nd) has shown that depending upon the particular system up to 17-25% at/o of the oxygen can be replaced by nitrogen, and, that these oxynitride glasses are found to have increased glass transition temperatures, higher densities, improved resistance to devitrification, higher refractive indices, increased indentation hardness and lower thermal expansion coefficients than their pure oxide analogues. These properties are generally what are to be expected if trivalent nitrogen substitutes for bivalent oxygen thus producing a more tightly-linked glass network.

Increased interest in nitrogen containing glasses has arisen as a result of the extensive work which is being carried out in the field of nitrogen ceramics. As has already been demonstrated oxides such as MgO and Y_2O_3 are being used extensively to promote liquid phase sintering in the densification of silicon nitride ceramics.

1.5.2 Silicon-Aluminium Oxynitride glasses.

Roebuck (61) has reported the formation of Si-Al-O-N glasses by rapid quenching in the SiO_2 corner of the Si-Al-O-N phase diagram, as shown in fig 1.2 (a). Loehman (59) and Jack (60) have shown that these glasses are difficult to prepare as dense glasses, tending to produce porous, frothy masses (possibly due to the loss of SiO (g) from the melt (59)).

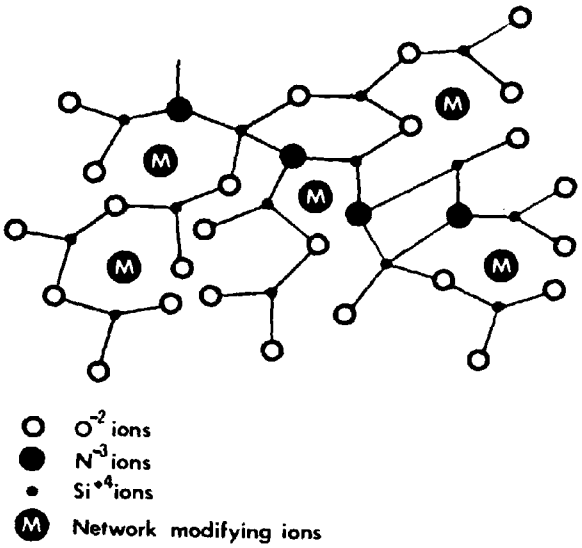

Figure 1.3

Schematic two dimensional view of the network structure of oxynitride glasses based on Si-Metal-O-N systems, after Risbud (57).

1.5.3 Magnesium Silicon Oxynitride Glasses.

Although glass formation has not been reported to occur in the MgO-SiO_2 system, the addition of a small amount of nitrogen does promote glass formation and there is a small glass forming region in the Mg-Si-O-N system (60). This small, homogenous glass forming region, fig 1.4 (a), is observed to exist by cooling appropriate compositions from 1700 ^{o}C at about 200^{o}C min^{-1}. By cooling at a slower rate or in the more SiO_2-rich region, opaque milky phase separated glasses are obtained. Shaw et al (62) has shown using TEM-microanalysis and crystallization experiments that the phase separated droplets are Si-rich with virtually no Mg, and that the matrix phase consists of approximately equal concentrations of Mg and Si, and contains most of the nitrogen.

The addition of Al to this system not only suppresses phase separation but also promotes extensive glass forming regions. The existence these regions which are completely homogenous hasbeen clearly demonstrated in work by Drew et al (60) and Shaw et al (62). Moving away from the triangular oxide face, fig 1.4 (a),the glass region is at first expanded and then gradually contracts. The limit of glassformation approximately corresponds to a composition in whichl in 5.5 oxygens have been replaced by nitrogen.

1.5.4 Yttrium Oxynitride Glasses.

The location of the glass forming region in the Y-Si-Al-O-N system is shown in fig 1.4 (b). This system is more refractory than the Mg-Si-Al-O-N system with the Y-Si-Al-O-N glasses having appreciably higher viscosities (60) than the corresponding Mg-Si-Al-O-N glasses.

1.5.5 Other systems.

Several other oxynitride glass systems have been studied , but as

yet are not so directly relevant to the densification of silicon nitride ceramics as the previous three examples. Among these are Ca, Nd, Li, La, -Si-Al-O-N systems (59,60) and M-Si-B-O-N systems (63).

1.5.6. Crystallization of oxynitride glasses.

Little work has been published on the crystallization of oxynitride glasses. Chyung and Wusirika (63), in their patent on oxynitide glass-ceramics, descibed 46 oxynitride glass compositions made from SiO_2, Al_2O_3, and Si_3N_4 plus oxides including Li_2O, BeO, MgO, Y_2O_3, La_2O_3, ZrO_2, HfO_2 and GeO_2. Although they listed the crystalline species obtained on devitrification of these glasses, they did not give any indication of the properties of the materials.

Loehman (59) has shown that devitrification of Y-Si-Al-O-N glasses (59) between 1000°C and 1200°C produces $Y_2Si_2O_7$ as the predominant phase with other phases, ie yttrium silicates, yttrium-aluminium silicates, nitrogen apatite ($Y_4Si_4O_{11}N_2$) being formed at the lower temperatures, and with some possible nitrogen substitution in the yttrium silicates.

. . .

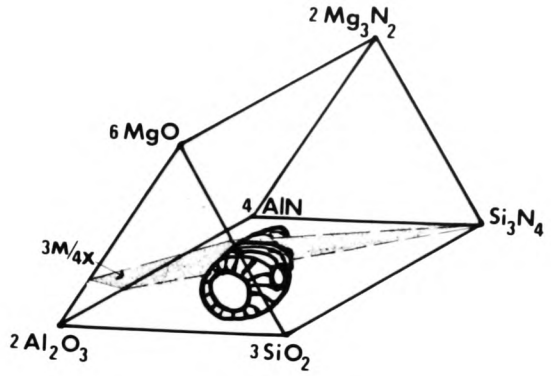

(a)

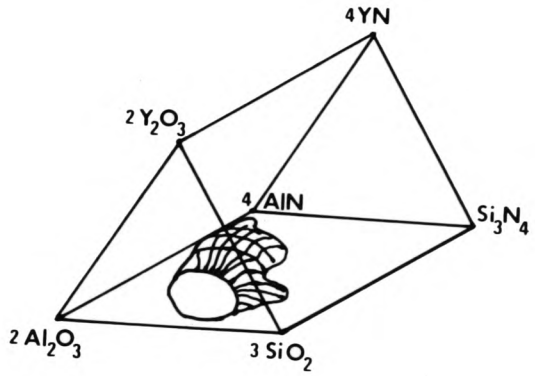

(b)

Figure 1.4

Glass forming regions at 1700°C in the (a) Mg-Si-Al-O-N system and the (b) Y-Si-Al-O-N system, after Drew et al. (60).

1.6 THE AIMS AND SCOPE OF THIS RESEARCH PROJECT.

It has been clearly demonstrated, from the reports in the literature referred to in the present chapter, that oxynitride glasses occur as intergranular phases in nitrogen ceramics. This together with the possibility of producing glass-ceramics in which the crystalline phases are refractory nitrides and oxynitrides, indicates the need to explore more fully oxynitride glass formation and in particular to investigate the crystallization behaviour of such glasses.

Presently B'-sialon ceramics densified with Y_2O_3 are providing a good compromise between 'ease of processing' and 'good high temperature properties'; for example, 'Lucas Syalon' have chosen this Y-Si-Al-O-N system for the production of high perfomance tool cutting tips, producing a B'-sialon material with a highly refractory yttrium-aluminium silicate glass matrix grain boundary phase.

In the Mg-Si-Al-O-N system however extensive liquid formation can occur at significantly lower temperatures (ie.below 1600°C) than in the Y-Si-Al-O-N system (1700°C-1800°C), which means that densification can be achieved at lower temperatures in the former system. No one has yet found however a method of effectively fully crystallizing the residual Mg-Si-Al-O-N intergranular glass.

It was therefore considered that a detailed investigation of the crystallization behaviour of Mg-Si-Al-O-N liquids and glasses with particular emphasis on those compositions in the 3M:4X plane would make a valuable contribution to both the understanding and future developement of magnesium sialon ceramics. Such a study should resolve the conflicting evidence for magnesium solubility in the B'-sialon lattice and should also provide useful guidelines for promoting the

crystallization of other nitrogen glass intergranular phases and of oxynitride glass-ceramics in general.

. . .

CHAPTER TWO.

EXPERIMENTAL TECHNIQUES.

2.1 PREPARATION AND REACTION OF Mg-Si-Al-O-N COMPOSITIONS.

A comprehensive series of compositions were made up in the 3M/4X plane of the Mg-Si-Al-O-N system represented by equation (4) on page 11. Each composition was prepared by grinding together appropriate proportions of Si_3N_4, SiO_2, MgO and Al_2O_3 powders in an AGS mortar and pestle grinding machine. These constituent powders were available as normal grade powders containing small but significant levels of impurities, and as ultrapure powders. The compositions discussed in Chapter Three are prepared from normal grade powders. In Chapter Four, where a glass has been prepared from the normal grade powders it is referred to as 'impure', and when prepared from the ultrapure grade powders it is referred to as 'pure'. The MgO, SiO_2 and Al_2O_3 powders were heated at temperatures in the region of 800-900^oC for six hours to drive off any water before weighing.

The powders were compacted into 13mm diameter cylindrical pellets at a pressure of 2.25 MN m^{-2}. The weighed pellets were packed in boron nitride powder contained in graphite crucibles and were reacted at 1600-1650^oC in a static 'oxygen free' nitrogen atmosphere (see fig 2.1 for a schematic diagram of the furnace and atmosphere control). The reaction times used were varied depending on the amount of liquid present in the pellet at reaction temperature (eg.2 hours for compositions with approximately 5% liquid, down to 12 minutes for completely liquid compositions.

A variety of cooling rates were used ;

(i) **Rapid quenching** : by allowing the graphite crucible to drop out of the vertical furnace into a liquid nitrogen bath. This gives a cooling rate of very approximately 50°C per second in the region 1650-800°C.

(ii) **Slow quenching** : by lowering the crucible down into the coolest part of the vertical alumina furnace tube.

(iii) **Slow cooling** : by slowly lowering the crucible down the vertical furnace giving a cooling rate of approximately 10°C per minute.

(iv) **Step quenching** : by dropping the graphite crucible down out of the hot zone into a cooler part of the furnace, holding at that temperature for a time, then quenching into liquid nitrogen.

The rapid quenching technique was used to solidify the liquid present at 1650°C into a glass, giving it as little chance as possible to crystallize while cooling. Subsequent annealing in order to crystallize the glass was carried out at temperatures ranging between 850°C and 1350°C in a gently flowing nitrogen atmosphere.

The slower cooling rates were used to investigate the crystallization of Mg-Si-Al-O-N liquids under cooling conditions more typically found in ceramic processing.

The characterization of the reaction product phases and the determination of their microstructure and elemental analysis was carried out using the techniques discussed in the following sections.

. . .

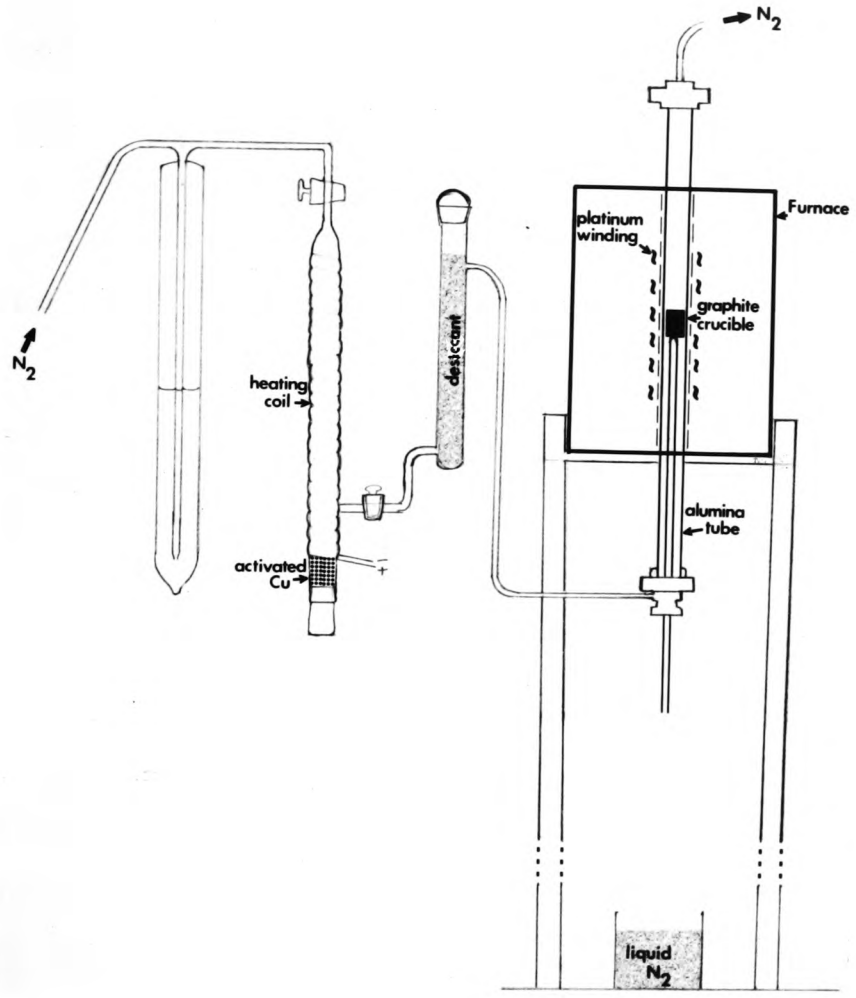

Figure 2.1

Diagram of the platinum-wound alumina tube furnace and the 'oxygen free' nitrogen atmosphere control apparatus.

2.2 X-RAY DIFFRACTION.

Crystalline phases were characterized by X-ray diffraction analysis employing a Guinier-Hagg XDC-700 focusing camera, using Cr $K\alpha$ radiation (wavelength 2.2897 $\mathring{A}$). This camera gives diffraction patterns of high resolution and low background while retaining a reasonably short exposure time(eg.~3-8 hr) through the use of a ground and curved Johansson-constructed monochromator crystal. The camera and monochromator are enclosed in an evacuable chamber to reduce air scatter. The operating principle of the Guinier camera is illustrated in fig 2.2 (a).

Specimens are prepared by dusting the powder, consisting of the sample plus an internal standard (silicon), onto a transparent adhesive film. Care must be taken to choose an adhesive film which does not interfere with the diffraction pattern from the sample and standard.

Where unit cell dimensions have been measured from the Guinier diffraction photographs, they are quoted to the last significant figure. For example, for a β'-sialon crystalline phase showing a full set of typically sharp diffraction lines, the unit cell dimensions can be calculated via a computer program and quoted to a fourth decimal place. For a B"-magnesium sialon phase, with its diffraction lines typically morediffuse, and possibly much weaker if it is a secondary phase, then the unit cell dimensions may be only quoted to two decimal places.

. . .

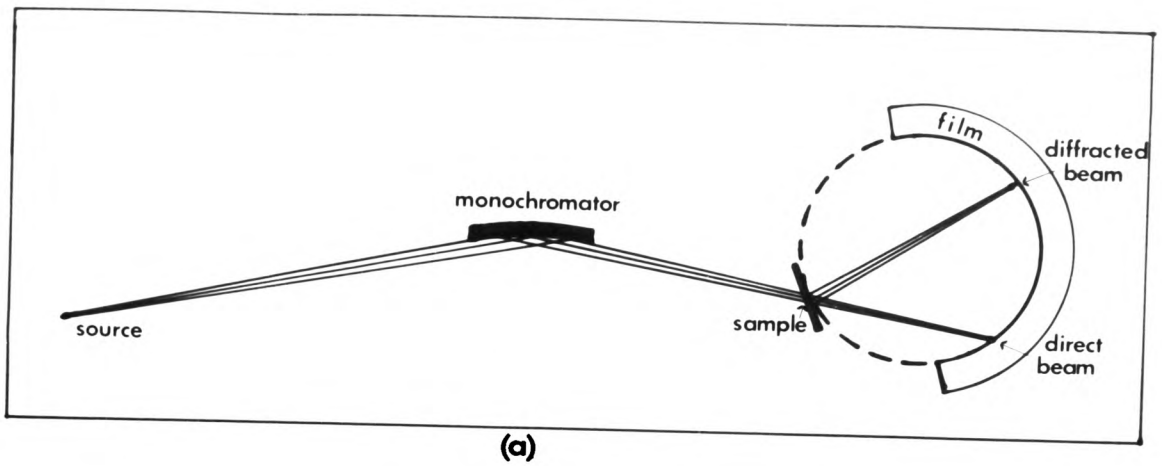

(a)

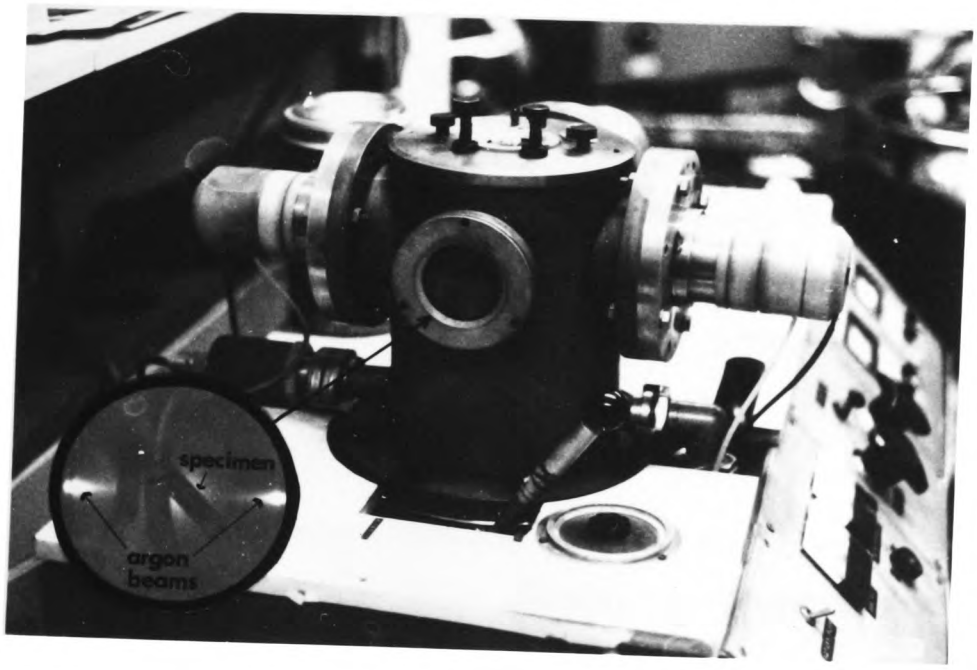

(b)

Figure 2.2

(a) The operating principle of the Guinier X-ray diffraction camera.

(b) Ion beam thinning apparatus, with (inset) through the viewing window showing the Ar beams incident on the specimen holder.

2.3 TRANSMISSION ELECTRON MICROSCOPY.

In the early 1970's 'Tighe, Barber, and Heuer et al' (64) demonstrated (following earlier work by Paulus and Reverchon (64)) that virtually any ceramic material could be thinned to electron transparency by ion-thinning techniques (foil thickness of the order of 2000 $\mathring{A}$ is required for conventional 100 KeV electron microscopes).

In this work TEM sections were prepared by lapping thin specimen plates to 60μm while attached to a glass slide, using silicon carbide abrasive paper on a polishing machine. These lapped sections were then transferred to brass rings (3mm in diameter) for ease of handling during the ion-beam thinning process and for fitting into the microscope specimen stage. The sections were thinned to perforation using 5kv Arions incident at 40 degrees to both surfaces, as illustrated in fig 2.2 (b), inset.

An alternative method used to prepare specimens of powdered forsterite and willemite, is to grind the powder crystals suspended in a methyl acetate-colloidon solution in an agate mortar, giving a suspension of very thin crystals some of which will be electron transparent. A drop of this fine suspension is then placed on a TEM copper grid which has previously had a continous carbon film deposited across it.

An electron beam passing through a thin crystal interacts with the atoms of the solid in many ways, see fig 2.3 (a) (65) :

(i) It can be scattered elastically (without energy loss), either coherently or incoherently (with loss of phase relations) ; or,

(ii) It can be scattered inelastically (with energy loss), leading to the generation of (a) characteristic X-rays, (b) secondary elec-

trons, (c) Auger electrons, (d) backscattered electrons.

In most cases, microscopists are interested in the coherently scattered (ie. Bragg-diffracted) electrons, which provide information on thenature of the crystal under observation, and onthedefects within these crystals.

The most common method of imaging in TEM involves making use of diffraction contrast; two modes of image formation are possible. In the first, the bright field technique, all diffracted beams are removed from the final image by an aperture of appropriate size, leaving only the transmitted beam to transverse the microscope; contrast developes because some features of the microstructure diffract differently from others (some contrast can also arise from mass-thickness differences). The second mode, dark field, involves forming an image with a diffracted beam only.

The TEM can be operated in the imaging mode or the diffraction mode:

(i) Imaging mode : electrons that are scattered from the same point in the specimen are brought to focus in the first image plane.

(ii) Diffraction mode : electrons that are scattered in the same direction from the specimen are brought to focus in the back focal plane. It is this pattern, formed in the back focal plane of the objective lens, that is known as the diffraction pattern and can be used to study the crystal structure and orientation of the material.

The X-rays excited in the sample by the high energy electron beam can be analyzed by a energy-dispersive or wavelength-dispersive detector, producing quantitative compositional microanalysis of the irradiated area.

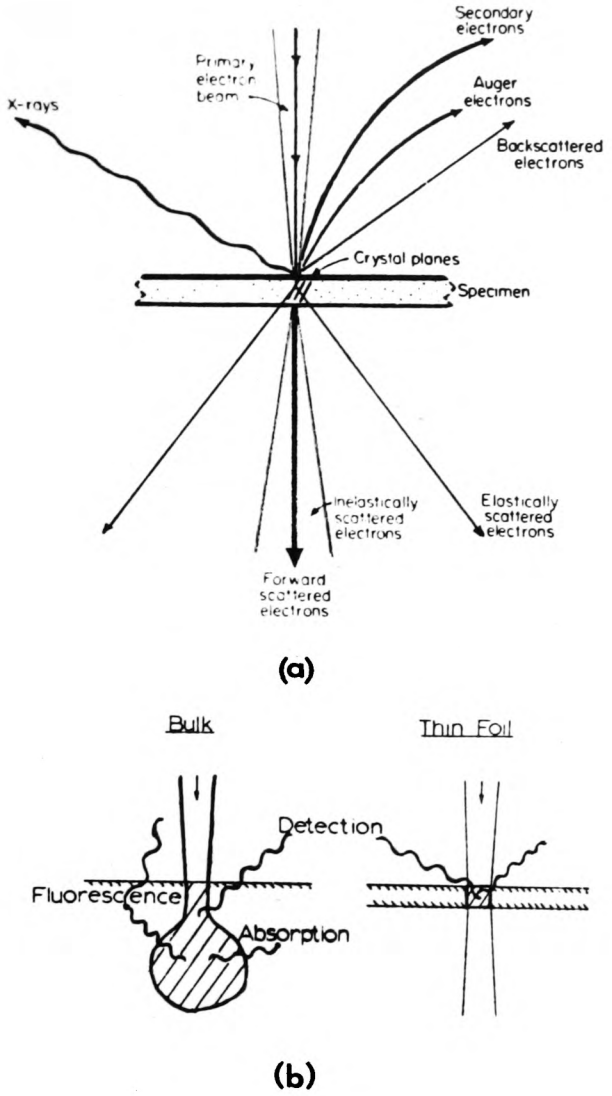

Figure 2.3

(a) Possible products of interaction of electron beam with crystalline sample (65).

(b)Schematic electron distribution in a bulk sample and a thin (1000 $\overset{o}{A}$) foil. The probability of X-ray absorption or fluorescence is small in a thin foil, after Lorimer and Cliff (67).

X-ray energy dispersive microanalysis methods, and the interpretation of electron diffraction patterns, are reviewed here with regard to, and, with examples from this research project as these techniques are used extensively through this project.

. . .

2.4 ENERGY DISPERSIVE MICROANALYSIS IN THIN TEM FILMS.

X-ray microanalysis of electron transparent thin films has two important advantages over 'bulk' analyses (ie. in the scanning electron microscope) :

(i) The ability to select areas 0.1 μm in diameter for analysis, with very limited spreading of the analyzed volume with depth below the electron beam entry surface, ie. the analyzed volume depends mainly on probe diameter and not, as in SEM, on beam penetration.

(ii) The relation of X-ray intensities to elemental concentrations can be greatly simplified by neglecting the absorption and fluorescence corrections associated with bulk-sample X-ray microanalysis. (ie. if the specimen is thin enough to carry out conventional 100 kV TEM, it is transparent to most of the primary X-rays produced by the incident electron beam, and X-ray absorption and fluorescence can, to a first approximation, be neglected, see fig 2.3 (b) (66).

The most widely accepted technique is the Cliff-Lorimer (67) approach, which uses the expression :

$$\frac{C_A}{C_B} = K_{AB} \frac{I_A}{I_B} \qquad \ldots (7)$$

where, C_A and C_B are the weight fractions of the elements A and B;
I_A and I_B are measured characterised X-ray intensities;
K_{AB} is the correction factor for ionization cross-section, fluorescent yield, and detector efficiency for X-rays from the two elements.

The constant K_{AB} varies with the operating voltage but is independent of sample thickness, composition, or orientation if the two intensities are measured simultaneously and if the thin-film criterion (no absorption or fluorescence) is satisfied. The constant K_{AB} (66) can be expressed as the ratio of individual correction factors (P) for each element, ie. $K_{AB}=P_A/P_B$. In this work the relative amounts of Mg, Al, and Si were calculated by measuring the areas of the respective peaks on the EDAX spectrum,and then dividing each element area by,(i) the appropriate P-correction factor (see Table 2.1) and (ii) by the element atomic weight giving units in molar terms rather than in weight fraction terms.

Table 2.1

P-Correction factors for 100 Kv electrons.

Element.	Atomic number.	Atomic weight.	P
Mg	12	24.312	.45
Al	13	26.982	.57
Si	14	28.086	.66

The X-ray intensities are measured by integrating (electronically) the area under the relevant peak and subtracting the background, or by alternatively using the peak heights as an estimate of the peak areas. The analysis time interval ideally should be the minimum time necessary

to give spectra peaks that have a smooth Gaussian curve like those illustrated in fig 2.4 (b). The reason for minimizing this time is to reduce the amount of radiation damage to the volume of analysis. However when a very small diameter electron probe is being used on a very fine microstructure then counting for long enough to give smooth peaks may not be possible, because there may be a very low count rate with a small probe size and there is the possibility of beam drift into an adjoining phase with time.

The constant K_{AB} can be obtained by measuring the intensity ratio in a sample of known composition which is homogeneous and closelyrelated chemically to the sample of interest. Because there is a tendency for the lighter element Mg ($K\alpha$) X-rays to be absorbed by the beryllium window of the EDAX detector, a forsterite (Mg_2SiO_4) specimen was analyzed to check the validity of the P-correction factors, Table 2.1, for determining the Mg/Si ratio of unknowns. A selection of thin clear forsterite crystals were analyzed by EDAX, one example of which is shown in fig 2.4 (a).

The mean measured molar ratio of magnesium to silicon for 12 analyses was 1.90 ± 0.04, which is less than the value of 2 expected for Mg_2SiO_4. and so an empirical correction factor of 'x 1.05' (ie. 2/1.90) was applied to all measured Mg/Si ratios with this particular EDAX unit.

EDAX equipment is presently limited to the detection of elements of atomic number greater than 10, due to fundamental problems with the production, collection, and absorption of low-energy X-rays. Hence the oxygen and nitrogen concentrations could not be measured in the MgSiAlON specimens by EDAX microanalysis.

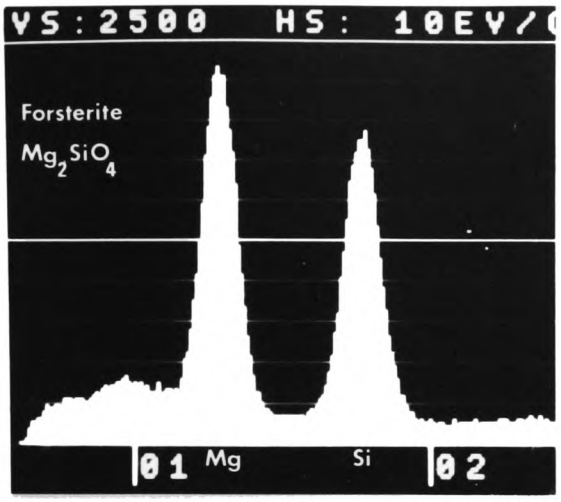

(a)

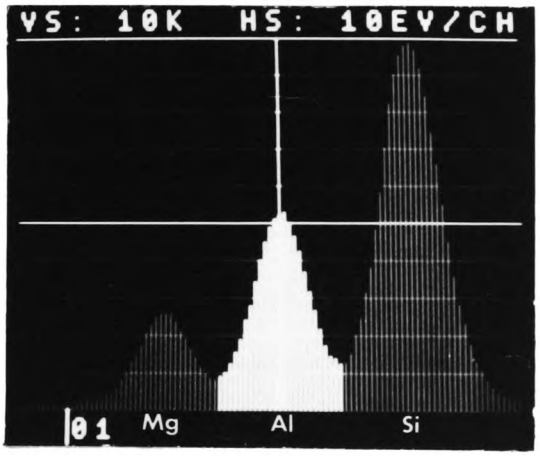

(b)

Figure 2.4

(a) EDAX spectra for Mg_2SiO_4 standard.

(b) EDAX spectra of a MgSiAlON phase with the horizontal axis expanded to show the smooth Gaussian shape of the peak curves.

2.5 ELECTRON DIFFRACTION.

2.5.1 Geometry of electron diffraction patterns.

The most convenient method for interpreting electron diffraction patterns is by means of the reciprocal lattice construction. In the ordinary lattice of the crystal, each stack of planes has a spacing which is characterized by a vector whose direction is normal to the planes and whose magnitude is indicated by the symbol d_{hkl}. If each vector is replaced by one having the same direction but a length which is the reciprocal of the original, namely d^{-1}_{hkl}, the points at the end of this collection of vectors also constitute a lattice which is called the reciprocal of the original lattice. Each point in the reciprocal space lattice therefore corresponds to a family of lattice planes of the crystal, and gives their direction and spacing.

The reciprocal lattice unit cell is defined by the vectors a^*, b^*, c^* satisfying the relations :

$$a^*.a = b^*.b = c^*.c = 1 \qquad \ldots (8)$$

$$a^*.b = b^*.c = c^*.a = a^*.c \ldots\ldots = 0 \qquad \ldots (9)$$

(all crossterms zero)

This means that a^* is normal to b and c ie. normal to the plane containing b and c, and similarly for b^* and c^*.

From the derivation of the reciprocal lattice it follows that if the crystal is rotated, the reciprocal lattice rotates with it: that is the reciprocal lattice and crystal always retain parallel orientation.

Reciprocal lattices are triclinic for triclinic crystals, monoclinic for monoclinic crystals (with b^* parallel to b of the crystal and with the angle β^* equal to 180-βdegrees), orthorhombic for orthorhombic

crystals, hexagonal for hexagonal crystals (with the sixfold reciprocal axis parallel to the crystal's sixfold axis, but with the reciprocal axes a^*_1 and a^*_2 at 60 degrees to each other, in comparison with the crystal axes a_1 and a_2 which are at 120 degrees to each other), rhombohedral for rhombohedral crystals and cubic for cubic crystals. In the case of the orthogonal lattices the axes of the reciprocal lattice are parallel to those of the crystal lattice as illustrated for the orthorhombic lattice in fig 2.5.

The reciprocal lattice concept is indispensible for interpreting electron diffraction patterns because of the convenient way in which points in reciprocal space represent the orientation and spacing of the crystal planes, the conditions under which any planes will reflect, and the position on a film at which any reflection will be found.

The condition for diffraction can be expressed in terms of a sphere in reciprocal space known as the Ewald reflecting sphere. The section of reciprocal space normal to the incident electron beam cut by the Ewald sphere is, in fact, the observed electron diffraction pattern which appears in the back focal plane of the objective lens in the TEM.

The Ewald sphere of radius λ^{-1} intersects point O at the origin of the reciprocal lattice (coordinates 000) and point G, the reciprocal lattice (coordinates hkl) whose position vector is **g**. S_0 and S are **unit** vectors in the direction of respectively the incident and diffracted beams. Now, the magnitude of the vector **g** is the reciprocal of the atom plane separation, d, in the space lattice ; from fig2.6 (a),

$$\sin\theta = \frac{OG/2}{OC} = \frac{OG}{2\,OC} = \frac{d^{-1}}{2\lambda^{-1}} \qquad \ldots (10)$$

or $2d \sin\theta = \lambda$, the Bragg equation.

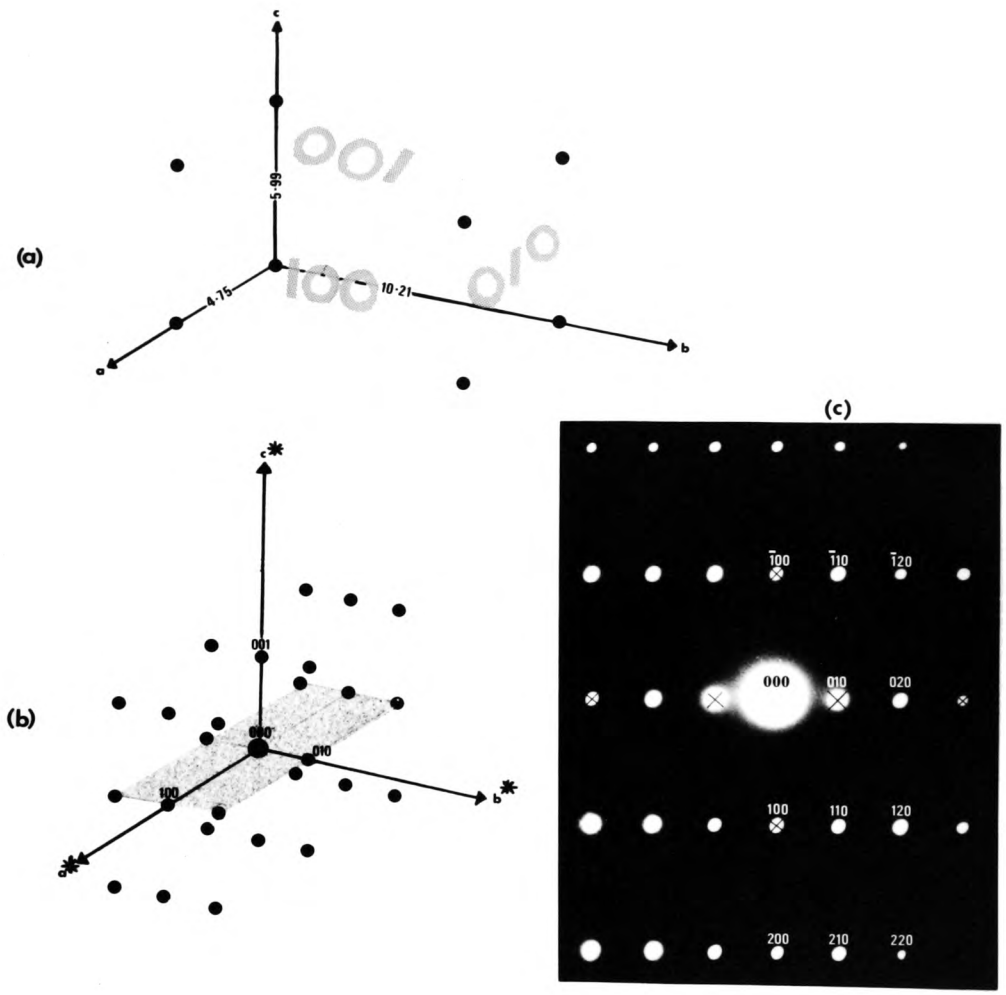

Figure 2.5

(a) Forsterite, Mg_2SiO_4, orthorhombic crystal lattice.

(b) Forsterite reciprocal lattice.

(c) Forsterite (001) electron diffraction photograph.

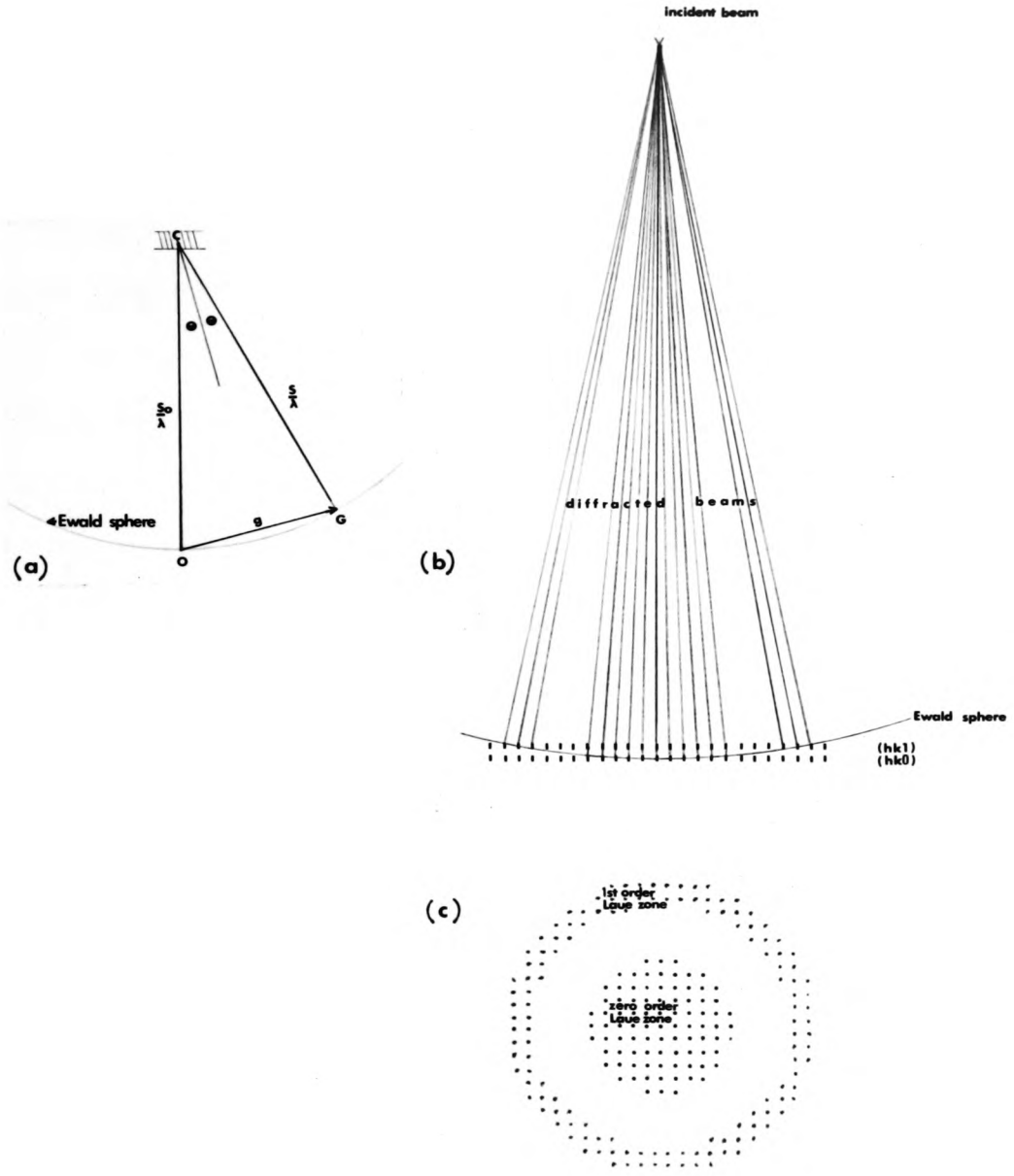

Figure 2.6

(a) The Ewald reflecting sphere construction.

(b) and (c) The effect of the curvature of the reflecting sphere.

So that, wherever the Ewald sphere touches a reciprocal point such as G, there can be a diffracted beam CG.

For 100 KEV electrons the wavelength is 0.037 $\mathring{A}$ giving an Ewald sphere radius λ^{-1} of 27 $\mathring{A}$ compared with typical reciprocal lattice vectors (d^{-1}_{hkl}) of about 0.15 $\mathring{A}$. The Ewald sphere is therefore nearly a plane section through the reciprocal lattice and in these circumstances the diffraction patterns represent plane sections of the reciprocal lattice.

The plane section appearance is enhanced by the fact that the reciprocal lattice points are extended into rods because of the thinness of the crystal so that more intersect the Ewald sphere than would otherwise be the case giving relaxation of the Bragg condition. Other factors contributing to extending the reciprocal lattice points are buckling of the specimen, the wavelength of the electrons not being strictly monochromatic, crystal imperfections such as dislocations and stacking faults, orientation effects, thermal motion and particle size broadening.

However the curvature of the reflecting sphere has important effects as shown in fig 2.6 (b) and (c). In the symmetrical (single crystal) pattern there is a tendency for the pattern to fade out with increasing θ. Spots may be formed away from the central region if the sphere cuts a second (or third) layer of the reciprocal lattice. In practice the central zero order Laue zone (arising from the reciprocal lattice plane which passes through the origin) usually occupies a large part of the recorded diffraction pattern, with possibly the first order zone just visible near to the edge of the pattern.

Indices of a diffraction pattern are assigned to the spots and the lattice orientation is determined by inspection (ie. comparing the

pattern with a model of the reciprocal lattice), or by calculating the d spacings obtained from the relation :

$$d_{hkl} = \frac{L\lambda}{R_{hkl}} \qquad \ldots (11)$$

L=effective distance (mm) from the specimen to the photographic plate.
R=distance (mm) between diffraction spot (hkl) to direct beam spot (000).
$L\lambda$ is known as the camera constant.
The above relation is derived from the Bragg equation by making a small angle approximation for theta.

2.5.2 Structure factor and double diffraction.

Before the reciprocal lattice is used for interpreting diffraction patterns it is necessary to consider which reciprocal lattice points are allowed, and which are forbidden, by considering the structure factor. For certain reciprocal lattice points, depending on symmetry, the structure factor is zero, and hence the Bragg reflection does not occur; these are termed 'systematic absences'.

The structure factor is obtained by adding together the amplitudes of waves scattered in a particular direction by atoms at different points (xyz) in the unit cell, and finding the resultant. In doing this the phase differences between the waves scattered by the atoms in the unit cell must also be taken into account. Each diffracted electron beam has the properties of a wave, with a characteristic amplitude and phase ; this information is represented by the structure factor , F_{hkl}, with the intensity, I, depending on F^2_{hkl}. If to each reciprocal lattice point there is attributed not only the coordinates hkl but also

F_{hkl}, the points of the reciprocal lattice take on added meaning, being the Fourier transform of the crystal structure. [Unfortunately dynamical scattering effects that vary greatly with crystal thickness, orientation, and perfection, can cause serious anomalies in the observed intensities of the diffraction spots in electron diffraction patterns. However the symmetry of the diffraction patterns, the systematic absences in the reflections and lattice take on added meaning, being the Fourier transform of the crystal structure] Unfortunately dynamical scattering effects that vary greatly with crystal thickness, orientation, and perfection, can cause serious anomalies in the observed intensities of the diffraction spots in electron diffraction patterns. However the symmetry of the diffraction patterns, the systematic absences in the reflections and gross differences in intensity between different groups of 'hkl' reflections can give a strong indication of the type of structure possessed by the particular compound being studied. (NB : Diffracted X-ray, electron and neutron beams are invariably called 'reflections').

In terms of crystal lattice coordinates the structure factor can be written :

$$F_{hkl} = \sum_i f_i \ (\theta) \ e^{2\pi i \ (hx + ky + lz)} \quad . \ . \ .(12)$$

The summation is over all the atoms in the unit cell, where (x,y,z) are the fractional coordinates of the i'th atom and f is the scattering factor for the i'th atom and 0 is the Bragg angle.

Fora unit cell with a centre of symmetry at the originthe sin terms cancel out and :

$$F_{hkl} = \sum_i f_i(\theta) \cos 2\pi (hx_i + ky_i + lz_i) \ . \ . \ .(13)$$

Although the allowed and forbidden points in the reciprocal lattice are given by the structure factor, certain forbidden reflections can occur on the diffraction patterns. This can be explained by the phenomenom of double diffraction resulting from diffracted beams, which are formed inside the specimen, acting as new sources for further diffraction by the crystal. Double diffraction is possible with electron diffraction because the diffraction angles are so small that they may be of the same order of magnitude as the range of orientation in the sample (less than 2 degrees). If a beam reflected by the $h_1k_1l_1$ plane, is again reflected by the $h_2k_2l_2$ plane of the same crystal, it appears on the photograph as a reflection having indices h_1+h_2 , k_1+k_2 , l_1+l_2.

The general result is that weak, and sometimes 'forbidden' spots gain intensity at the expense of the strong ones. The extra 'forbidden' spots which result from the double diffraction can be identified by translating the primary diffraction pattern, without rotation, so that its origin coincides successively with all the strong spots of the primary pattern, and observing whether any absences in the primary pattern are filled in. Such 'forbidden' reflections present along a row of spots in an electron diffraction pattern disappear if the row of spots is isolated by tilting the crystal round that row. 'Forbidden' reflections which result entirely from the choice of a non-primitive unit cell cannot occur by double diffraction.

The forsterite (001) reciprocal lattice plane is shown shaded in fig 2.5 (b) and the corresponding forsterite (001) electron diffraction pattern is shown in fig 2.5 (c). The crossed 0K0 spots, $0\bar{3}0$, $0\bar{1}0$, 010, 030, and the crossed 100 spots, $\bar{1}00$ and 100, in the photograph have

zero structure factor, but however appear in the electron diffraction photograph because of multiple diffraction.

. . .

2.6 SCANNING ELECTRON MICROSCOPY.

Microstructure and phase morphology were also determined by scanning electron microscopy (SEM). The SEM may be operated in the secondary electron mode or backscattered electron mode :

(i) Secondary electron mode :Secondary electrons are generated in a very thin surface layer by the primary electron beam, and, monitoring of these secondary electrons produces high resolution topographic contrast images of the surface relief.

This specimen surface relief can be produced by etching highly polished surfaces of the specimens. Specimens were prepared by mounting in resin on a glass slide, polishing to a 0.25 μm finish, and etching for a few seconds in a 1% HF solution (or alternately for a few minutes in hot HCl for some specimens). They were then vacuum coated with a thin gold film prior to being examined in a Cambridge Stereoscan 150 electron microscope.

(ii) Backscattered electron mode : By monitoring the back scattered electrons instead of the secondary electrons, atomic number contrast images are obtained. The optimum atomic number contrast is obtainable from electrons leaving the specimen surface in trajectories perpendicular to the surface plane. The local brightness of back scattered atomic contrast is proportional to the atomic number.

The specimens were prepared by polishing to a 0.05μm finish.

2.7 DIFFERENTIAL THERMAL ANALYSIS.

DTA was used to determine the glass transition temperature and a suitable temperature range for annealing MgSiAlON glass. In DTA the temperature of the test material is measured relative to that of an adjacent inert material (eg. Al_2O_3) while the furnace temperature is raised at a constant heating rate. Any reaction occuring in the test material involves an energy change which usually manifests itself as a thermal effect.

A glass transition temperature shows as a small endothermic step in the baseline of a DTA trace. Above the T_g, in the undercooled liquid phase, the atoms are free to make extensive translational movements; below that temperature they are immobilized except for vibrational motions about their average positions. The crystallization of a glass shows as a strong exotherm on the DTA trace. This results from the latent heat of transformation associated with the change in order occurring when the glass crystallizes and the atoms change from an irregular arrangement in space to a highly ordered regular one. The exact temperature of this crystallization peak can vary with the heating rate used ; with slow heating rates tending to lower the observed crystallization temperature.

The specimen preparation for the MgSiAlON glasses analyzed involved grinding the powdered glass to the same particle size as the Al_2O_3 reference powder ie. <300 microns.

. . .

CHAPTER THREE.

THE 3M/4X PLANE OF THE Mg-Si-Al-O-N SYSTEM.

3.1 COMPOSITION.

The 3M/4X composition plane in the Mg-Si-Al-O-N system is shown shadedin fig 1.2 (b) and drawn on its own in fig3.1.The liquid isotherms are drawn using previously published data by Jack (9) plus data obtained in the present work. The eutectic temperature is estimated to be 1425 ±10°C.

β'-sialon, forsterite and spinel are the only crystalline phases known to exist in the composition range of this 3M/4X plane phase diagram. As discussed in Chapter One the existence of magnesium substituted β'-sialon solid solution, which would exist at compositions within the area of this 3M/4X plane, has not been proved.

Initially a series of compositions were prepared in the 3M/4X composition plane, and reacted at 1650°C, to check the existing phase diagram and toascertain whether in fact any compounds do exist within this plane. The compositions investigated are mainly within the triangle bounded by the β'-sialon solid solution composition range and the composition which most easily forms a liquid (ie.theeutectic composition for the 3M/4X plane). This triangle is shown shaded in fig 3.1.

Assuming no magnesium substitution in the β'-sialon and that no phases with composition outside the 3M/4X plane are formed, compositions within this shaded 'Si_3N_4-$SiAl_2O_2N_2$-Eutectic' triangle, reacted at 1650°C and before cooling, should consist of either liquid or liquid plus β'-sialon.

Initially the two following series of compositions were reacted at 1650°C, and then quenched so as to try and solidify any residual liquid as glass :

(A) **M2, M4, M6,** (lying on a composition line passing through E, the eutectic composition)

This M series, after reaction completion and before cooling, should give a progression of 'B'-sialon plus liquid' products with the volume proportion of liquid increasing, until, at about M5 the specimen is completely liquid. The numeral after the M is equal to the 'm' in equation (4), page 11, corresponding to increasing levels of Mg relative to Al and Si.

(B) **J4, K4, L4, M4, N4, O4, P4, Q4.**

This series of compositions all have the 'm' of equation (4) equal to four giving a progression of compositions with the Mg level constant. J4, lying on the Si_3N_4-Mg_2SiO_4 tie line, contains no Al, while in K4 through to P4 the Si is progressively replaced by Al in moving towards spinel, $MgAl_2O_4$.

These two composition series were chosen to give an indication of the effect of different composition variables across the 3M/4X plane.

. . .

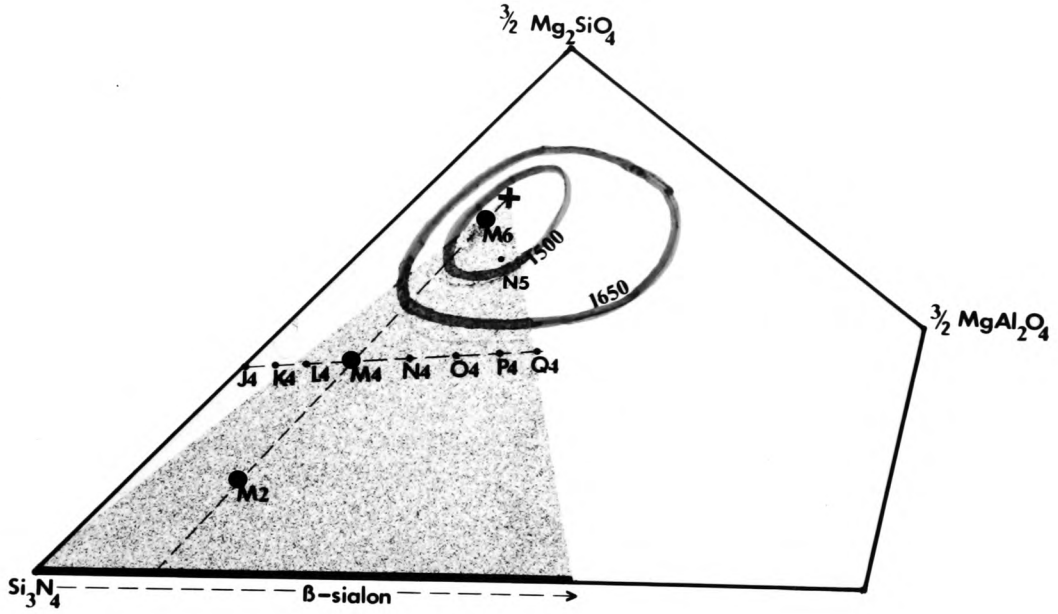

Figure 3.1

The 3M:4X plane of the Mg-Si-Al-O-N system, with all compositions given by $Mg_{m/2}Si_{6-z+(m/2)}Al_{z-m}O_zN_{8-z}$.

3.2 REACTION PRODUCTS OF COMPOSITIONS M2, M4, M6 AND THE EUTECTIC.

The M2, M4, and M6 specimens were reacted for 2 hours, 1.5 hours and 12 minutes respectively at 1650°C, and then quenched. The crystalline phase products, as determined by X-ray diffraction are presented in Table 3.1. SEM micrographs of these three specimens, polished and etched with HF, together with a section of their respective Guinier X-ray diffraction photographs, are shown in fig 3.2 (a).

Also included in Table 3.1 are the results for an M6 specimen and a eutectic composition specimen which were each reacted at 1650°C for 12 minutes and then slow quenched by lowering the crucible down into a cool part of the furnace alumina tube. Fig 3.2 (b) shows an SEM micrograph and a X-ray diffraction photograph of the slow quenched M6 specimen.

TEM micrographs of the slow quenched M6 specimen are shown in fig 3.4, together with EDAX analyses of a typical crystal and the glass matrix. Electron diffraction patterns of this specimen's hexagonal crystals are shown in fig 3.5.

TEM micrographs and their associated EDAX analyses of the M4 specimen are shown in fig 3.6.

Table 3.1

Crystalline phases present in reacted and quenched M2, M4, M6 and eutectic specimens.

Composition and cooling.	Crystalline phases.		hexagonal unitcell dimensions (A) a	c
M2 rapid quench	β'-sialon	(s)	7.631	2.930
	β"	(w)	7.825	3.068
M4 rapid quench	β'-sialon	(ms)	7.614	2.918
	β" {a}	(m)	7.814	3.069
	β" {b}	(w)	7.933	3.113
M6 rapid quench	β'-sialon	(faint tr)	-	-
	β"	(faint tr)	-	-
M6 slow quench	β'-sialon	(tr)	7.606	2.913
	β"	(ms)	7.837	3.091
eutectic slow quench	none			

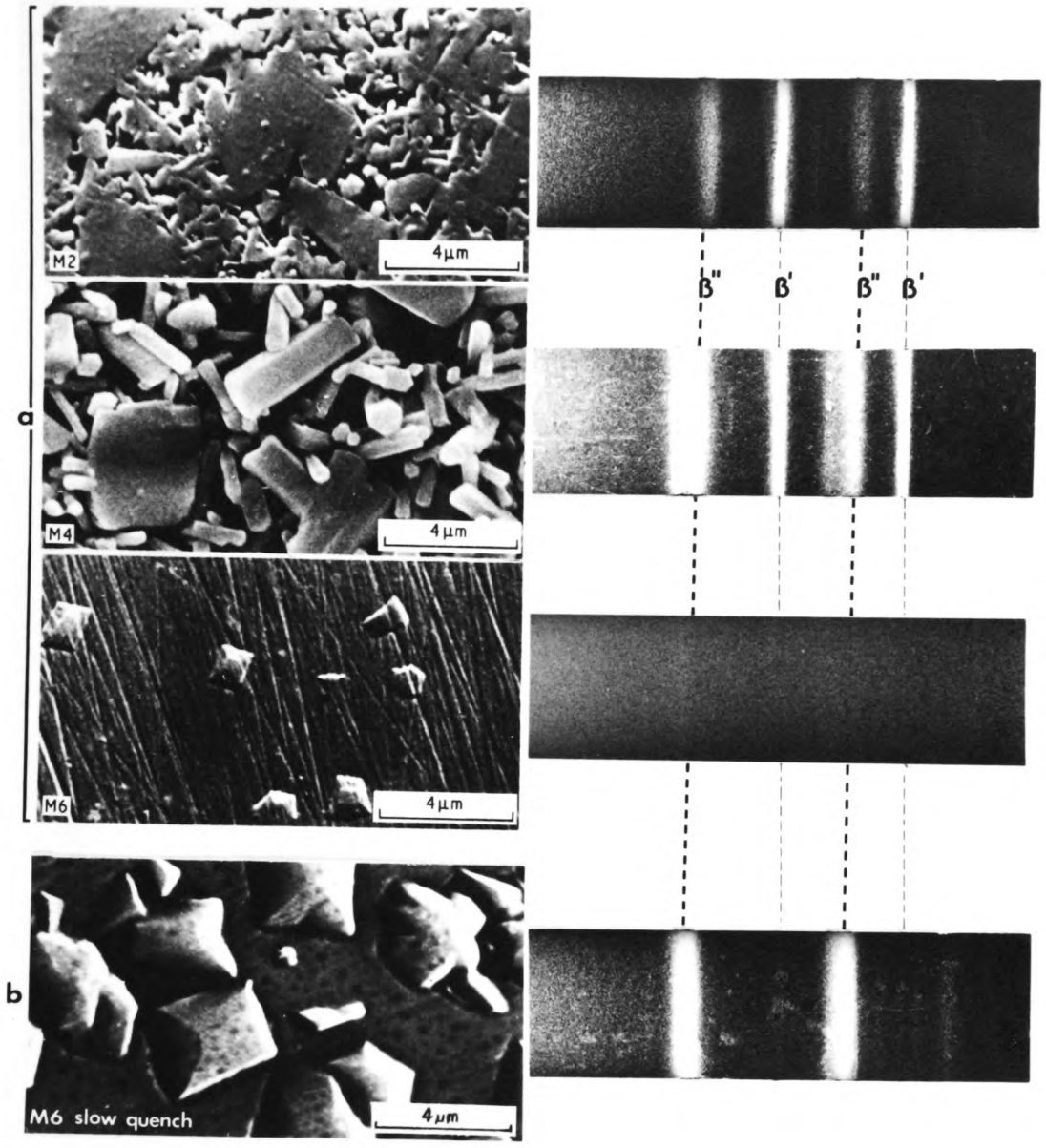

Figure 3.2

(a) SEM photographs of M2, M4 and M6 specimens reacted at 1650°C and rapid quenched , with their respective Guinier X-ray diffraction photographs.

(b) SEM photograph and X-ray diffraction photograph of M6 specimen reacted at 1650°C and slow quenched.

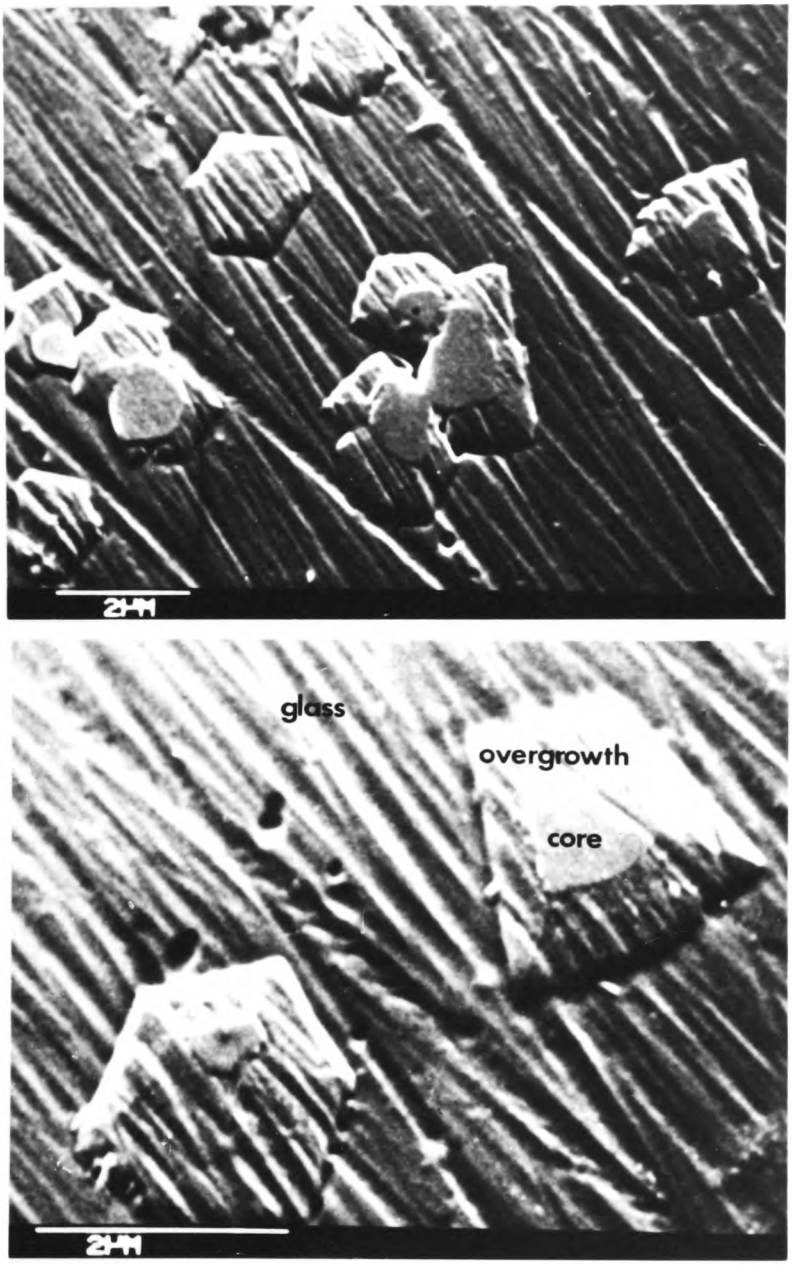

Figure 3.3

The core and overgrowth of a crystal precipitated from an M6 glass specimen reacted at 1650°C and rapid quenched (HF etch).

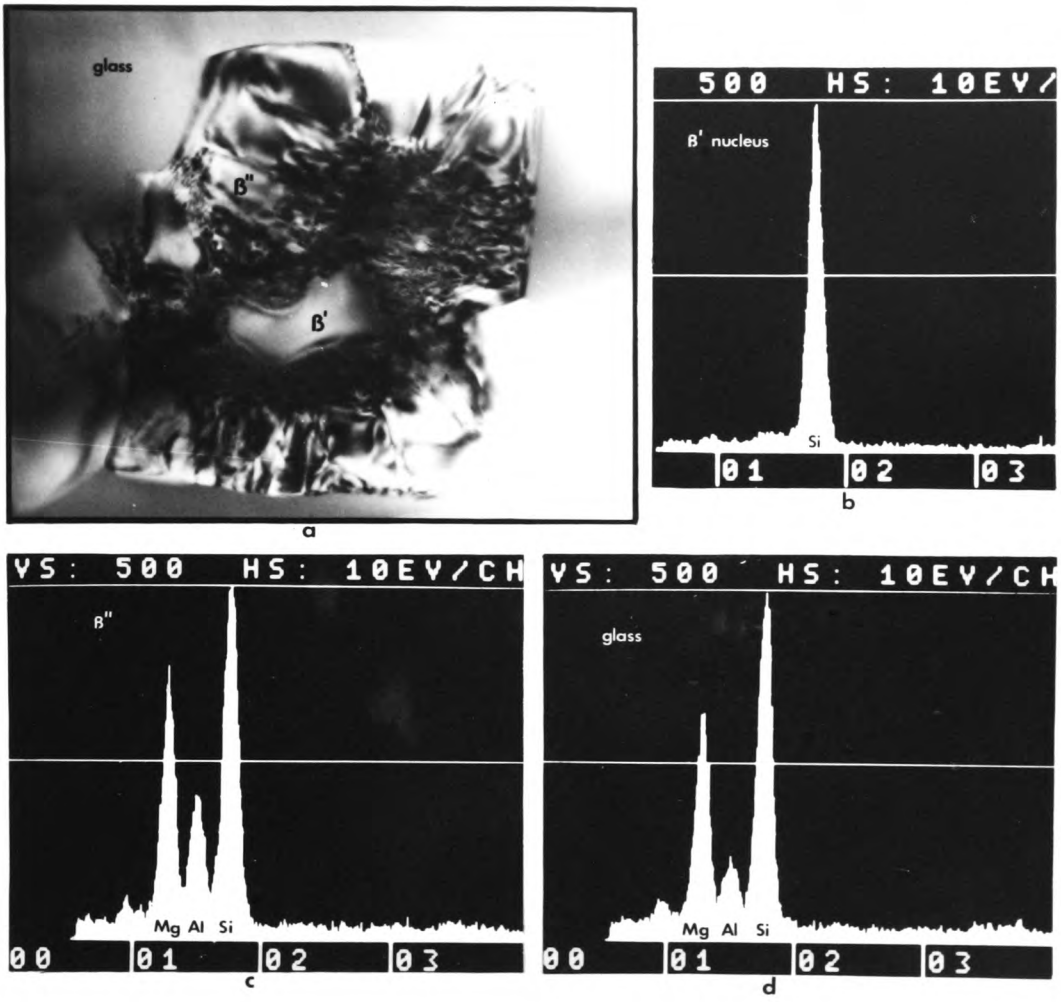

Figure 3.4

M6 specimen, slow quench :TEM micrograph (a) of a hexagonal crystal dispersed in the glass matrix, and associated EDAX analyses of (b) β'core, (c) β" overgrowth, and (d) glass matrix.

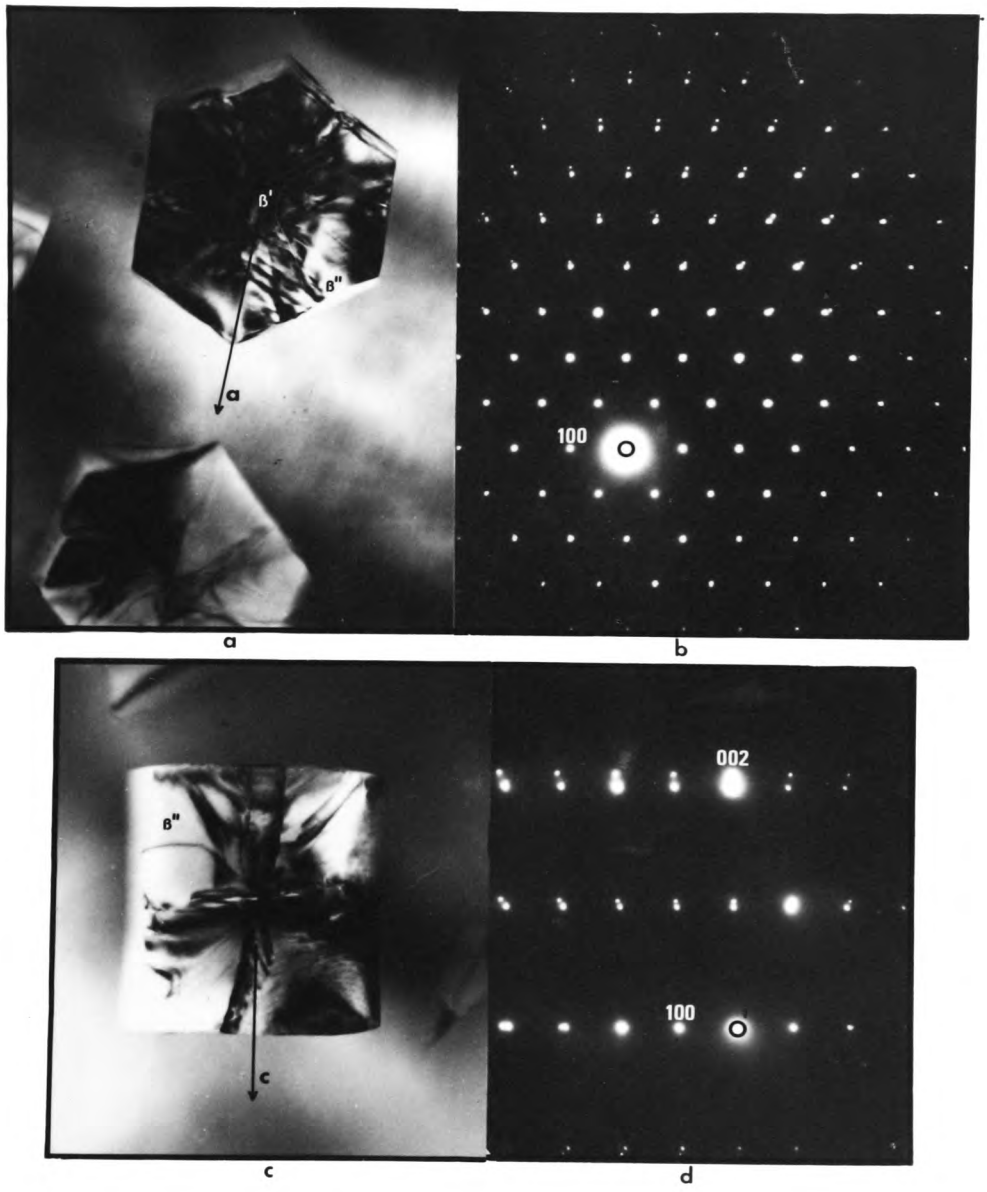

Figure 3.5

TEM micrographs of hexagonal crystals (M6 slow quench) with associated electron diffraction patterns.

(a,b) electron beam parallel to c-axis.

(c,d) electron beam perpendicular to c-axis.

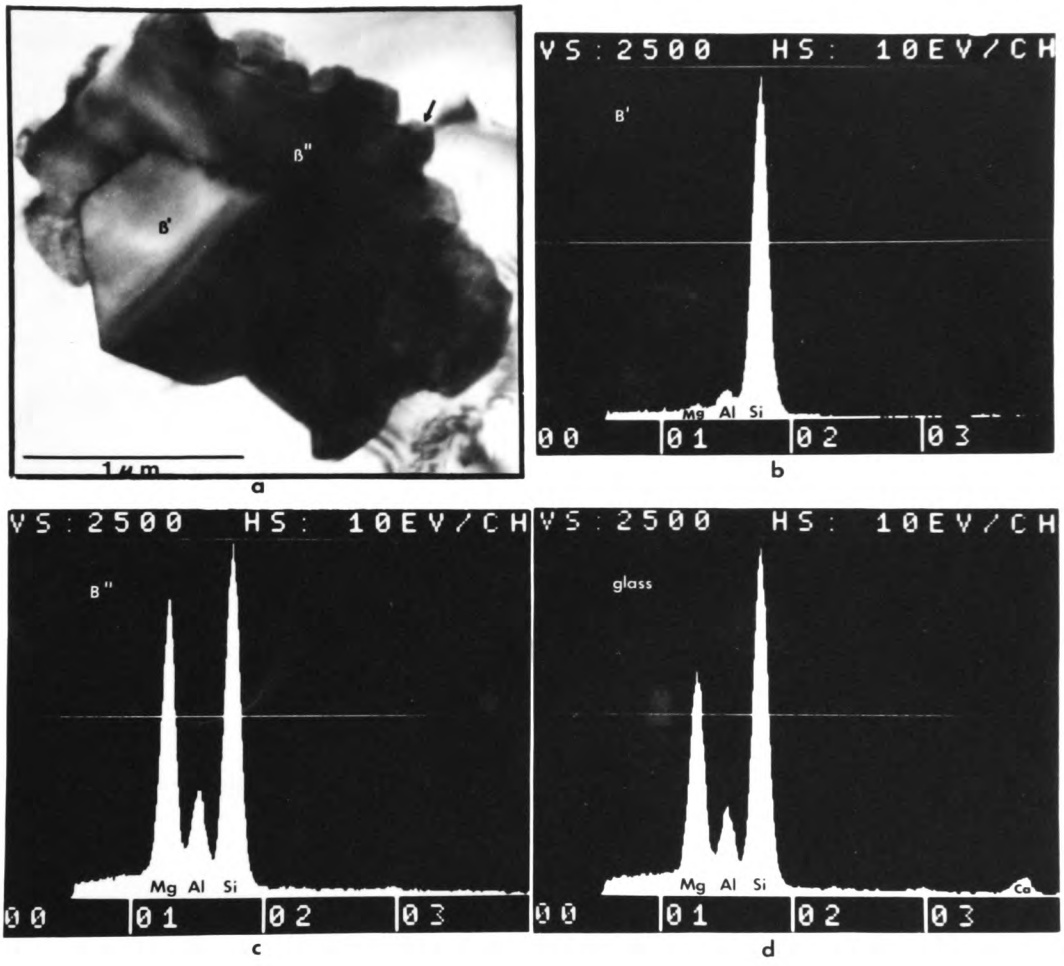

Figure 3.6

(a) TEM micrograph of M4 specimen reacted at 1650°C and quenched.

(b) EDAX analysis.

The M2 specimen contained approximately 10% volume of liquid at temperature, estimated from the amount of etched area in SEM micrographs. There are small pores visible throughout the specimen. The X-ray diffraction results indicate that the crystalline material is mainly β'-sialon, but together with it is a second distinct hexagonal phase, termed β", with unit cell dimensions larger than that possible for a β'-sialon.

The M4 specimen was estimated to contain approximately 30-40 % volume of liquid at temperature and the reacted pellet was very porous, with frothing having occurred blowing the pellet out of its original shape.

The crystalline material consists of inner cores of β'-sialon crystals overgrown epitaxially with β". There appears to be a second layer of crystals growing epitaxially on the main β" layer, arrowed in fig 3.6 (a). The X-ray diffraction photographs show two β" diffraction patterns, {a} and {b}, representing hexagonal cells of different dimensions, undoubtedly corresponding to the two layers of overgrowth observed in the TEM micrograph. The EDAX metal atom analyses for the M4 specimen show that:

(i) The contents of the inner cores of crystals are almost entirely Si with traces of Al.

(ii) The β" overgrowth consists of Mg, Al and Si.

(iii) The residual glass is similar in composition to that of the β" overgrowth crystal but with less Mg present and with some Ca impurity evident.

The M6 specimen was completely liquid at temperature and on cooling was observed to consist of homogenous partially transparent glass.

However dispersed evenly throughout the glass matrix are small faceted crystals about 1-2μm across. On close inspection the crystals are seen to consist of small central cores averaging about 1μm in diameter which are surrounded by an overgrowth of secondary material of thickness about 0.5μm. The scratch marks produced by the grains of SiC 0.25μm polish show the inner core to be much harder than the overgrowth, see fig 3.3. The crystalline content of this specimen is so low that any diffraction lines are barely detectable on a Guinier photograph, see fig 3.2 (a) M6.

However, adopting a slower cooling rate for the M6 specimen results in a dramatic increase in the size of the faceted hexagonal crystals dispersed in the glass matrix, see fig 3.2 (b). The thickness of the crystalline overgrowth has increased to approximately 2μm with the slower cooling rate. This increase in size of the overgrowth coincides with the appearance of a medium strong β" X-ray diffraction line, with β'-sialon lines barely detectable, fig 3.2(b).

TEM micrograph 3.4 (a) of the slow quenched M6 specimen shows a typical crystal dispersed in the glass matrix with a strain free central core clearly visible surrounded by a highly strained overgrowth phase. All the observed dispersed crystals exhibit this characteristic form. The EDAX metal atom analyses show clearly that :

(i) The inner core consists only of Si.

(ii) The peripheral B" 'overgrowth' region consists of Mg, Al and Si.

(iii) The matrix glass is of similar composition to the β" but contains relatively smaller proportions of Al and Mg.

The electron diffraction patterns show double spots which can be indexed on two β structures of small and large hexagonal cell

dimensions, indicating that the ß" overgrowth is growing in identical orientation to the ß' core, ie. epitaxial growth.

The eutectic composition specimen slow quenched to a clear transparent glass with no crystalline species present.

. . .

3.3 REACTION OF COMPOSITIONS J4 to Q4.

A series of pellets, compositions J4 to O4 (fig 3.1) were reacted for 90 minutes and rapidily quenched. Table 3.2 shows the crystalline phases present in the reaction products as determined by X-ray powder diffraction.

.

Reacting and quenching J4 and K4 results in a reaction product consisting of just ß'-sialon plus glass. With increasing Al content specimens L4, M4 and N4 contain in addition to ß'-sialon (of increasing unit cell dimensions) and glass,the new expanded ß" phase.

However near composition O4 there clearly exists a point where the Al content has increased to such a level that 15R polytype is formed. The 15R phase has a cation:anion ratio of 5/6 and hence its formation lowers the cation:anion ratio of the residual MgSiAlON glass below 3:4. When the Q4 composition is reached spinel and 15R have become the dominant stable crystalline products.

. . .

Table 3.2

Crystalline phases present in J4→Q4 reacted at 1650°C and quenched.

Specimen	Crystalline Phases		Hexagonal 'a' unit cell dimension, A.
J4	β'-sialon	(ms)	7.603
K4	β'-sialon	(ms)	7.609
L4	β'-sialon	(ms)	7.611
	β" (m)		**7.838**
M4	β'-sialon	(ms)	7.615
	β" {a}	**(m)**	**7.814**
	β" {b}	**(w)**	**7.933**
N4	β'-sialon	(ms)	7.630
	β"	**(m)**	**7.807**
O4	β'-sialon	(wm)	7.638
	β"	**(m)**	**7.819**
	15R	(m)	
P4	β'-sialon	(w)	7.643
	β"	**(m)**	**7.819**
	15R	(s)	
Q4	β'-sialon	(vw)	7.64
	β"	**(wm)**	**7.795**
	15R	(ms)	
	spinel	(s)	

3.4 EFFECT OF COOLING RATES ON THE FORMATION OF β".

The M4 composition specimen, reacted at 1650°C for 1.5 hours and rapid quenched, gave a product of β'-sialon, two distinct β" phases and residual glass (fig 3.2 and Table 3.1). At this stage, three identical M4 specimens were reacted at 1650°C for 1.5 hours and cooled at different rates to study the effect of cooling rate on the formation of β" and on the solidification and crystallization of the residual MgSiAlON liquid.

The three cooling rates used were, (a) rapid quench, (b) slow quench and (c) slow cool, corresponding to the cooling techniques mentioned in Chapter 2, page 28. Each specimen was subsequently annealed at 1200 °C for 2 hours in a nitrogen atmosphere. Guinier X-ray diffraction photographs of the reaction products are shown in fig 3.7.

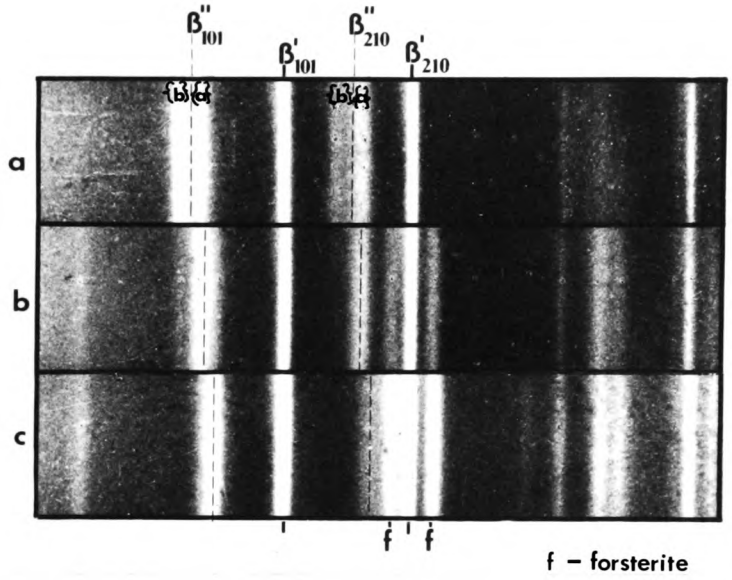

Figure 3.7

Effect of cooling rate on the product of a M4 composition pellet after reacting for 1.5 hours at 1650°C.

(a) rapid quench, (b) slow quench, (c) slow cool.

The following observations were made :

(a) **Rapid quench** : this specimen is identical to the M4 specimen described on page 59, consisting of β'-sialon and two distinct β" layers, {a} and {b}. When this specimen was annealed at 1200°C the X-ray photograph showed no trace of the β" diffraction lines but in their place forsterite, Mg_2SiO_4, and a trace of spinel, $MgAl_2O_4$ were observed.

(b) **Slow quench** : X-ray photographs again show β'-sialon and β" but in this case only one β" diffraction pattern is observed, the hexagonal cell having dimensions identical to those of β" {a} in the previous case. Weak forsterite lines are also present.

Annealing at 1200°C results in the disappearance of the β" diffraction lines, an increase in the intensity of the forsterite lines and the appearance of weak spinel lines.

(c) **Slow cooling rate** : the X-ray diffraction photograph shows β'-sialon together with forsterite and weak β" diffraction lines corresponding to relatively low cell dimensions : that is, a hexagonal 'a' unit cell dimension of 7.78 Å, only slightly larger than a z=4.2 β'-sialon.

Annealing at 1200°C has no effect on the phases as observed by X-ray diffraction.

. . .

3.5 SUMMARY

3.5.1 Occurrence of β".

In the series M2, M4, to M6, the proportion of liquid present at reaction temperature increases and the proportion of β'-sialon decreases, until at the M6 composition the specimen is completely liquid at reaction temperature. This increase in the volume of liquid in going from M2 to M4 leads to severe bloating and a decreases in density. Arias (10) found that sintering Si_3N_4 with increasing amounts of MgO (in excess of about 4 equivalent %) gives a decrease in product density. This decrease also causes bloating which itself is caused by the increasingly fluid liquid phase facilitating formation of bubbles of SiO and N_2 gases from the reaction of Si_3N_4 and SiO_2. However the M6 composition specimen which is fully liquid at reaction temperature forms a solid non porous glass on quenching.

It is apparent from the results reported in this Chapter that following quenching of the M2, M4 and M6 compositions, a second hexagonal crystalline phase is present as well as β'-sialon. This is the phase termed β" in Tables 3.1 and 3.2.

The X-ray diffraction results confirm that this β" phase exists with a range of hexagonal unit cell dimensions from ;

$a=7.78\ \text{Å}$ $c=3.06\ \text{Å}$, to $a=7.933\ \text{Å}$ $c=3.113\ \text{Å}$,

(indicating a range of composition).

These unit cell dimensions, while of similar magnitude to that of β'-sialons, are all significantly larger than the maximum theoretical values (assuming a linear relationship between all dimensions and compositions) for a hypothetical z=6 β'-sialon ($a=7.760\ \text{Å}$, $c=2.972\ \text{Å}$) as illustrated graphically in fig 3.8. These large hexagonal unit cell

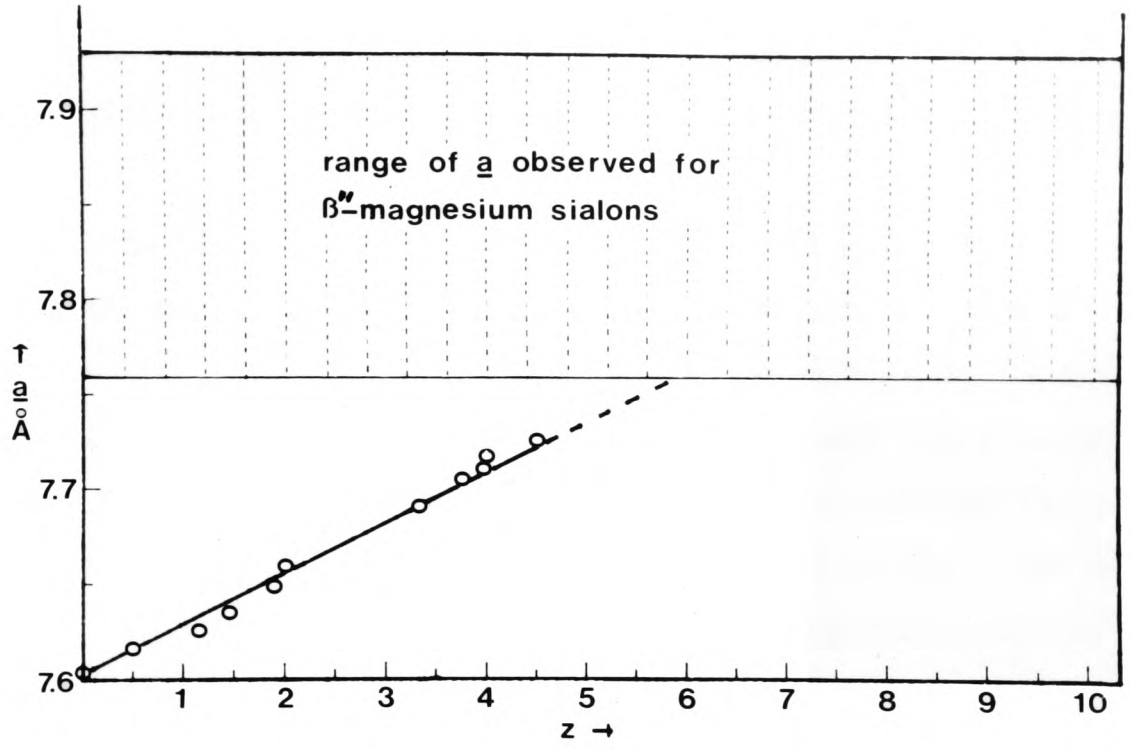

Figure 3.8

Plot of 'a' dimension versus z for β'-sialons, showing the range of dimensions for β" in the present study.

dimensions strongly indicate that β" is, in fact, a β'-magnesium sialon, with some substitution of the larger Mg atom for Al and/or Si in the β'-lattice, as suggested by Jack (34). The c/a ratio for these β" crystals is 0.394, slightly larger than the β'-sialon c/a ratio of 0.383.

For the M6 specimen, the observed correlation between the large increase in size of the dispersed hexagonal crystals and the increase in intensity of the β" X-ray diffraction lines on reducing the cooling rate suggests that the β" material is the 'overgrowth' which has either precipitated out of the liquid onto the small 'cores', or, has grown around the 'cores' from the glass matrix during cooling. As one might expect the overgrowth layer is much thicker at the slower cooling rate as it has had more time to grow. EDAX (TEM) analysis of the slow quenched M6 overgrowth in fig 3.4 (c) confirms that this β" overgrowth is a magnesium sialon.

The fact that β" is not observed in the diffraction patterns of J4 and K4 indicates that β" does not crystallize as easily from a liquid with a very low Al content, and possibly not at all when there is no Al. This also suggests that Al as well as Mg may well be a necessary component in the formation of the β" phase, unlike the situation for Be which can substitute for Si without the presence of Al.

3.5.2 Nucleation of β".

In the slow quenched M6 specimen substantial β" growth occurs around the β' nuclei precipitated from the liquid. The absence of any β" crystals in the slow quenched eutectic composition specimen, which has a composition very close to that of M6, strongly indicates that the presence of β' nuclei is a prerequisite for β" growth.

From the 3M/4X plane composition diagram, fig 3.1, it can be seen that the M6 composition lies just a small distance away from the eutectic composition towards the Si_3N_4 corner. Therefore it would be expected that a fine distribution of Si_3N_4 crystals would precipitate from the M6 liquid on cooling. This is confirmed by the EDAX (TEM) analyses of a core (fig 3.4 b) which shows only silicon and by the fact that the observed hexagonal unit cell dimensions of the slowly quenched M6 β' phase are the same (Table 3.1) as for β'-Si_3N_4.

The electron diffraction patterns in fig 3.5 indicate that the β" is growing in identical orientation to the β' core, that is epitaxial growth. The TEM micrograph and EDAX analyses of the rapidly quenched M4 specimen shown in fig 3.6, show the core to be a β'-sialon crystal again surrounded with an epitaxial magnesium sialon overgrowth of β".

Heterogeneities in a glass may promote nucleation because of their effectiveness in lowering the energy barrier to nucleation by reducing the initial nucleus surface energy (69). The following factors present in these MgSiAlON glasses fulfill the conditions necessary for effective nucleation of β" by β-Si_3N_4/β'-sialon nuclei:

(a) The mode of formation of β' nuclei, that is precipitation from the MgSiAlON liquid, and the chemical similarity of β-Si_3N_4/β' sialon to the glass ensures a low β'/glass interfacial energy.

(b) The β" and β' phases are structurally very similar as shown by the electron diffraction evidence.

(c) The difference in lattice parameters between the largest dimension β" and β-Si_3N_4 is only 4.4 %. This enables a reasonably coherent β'/β" boundary to form. In most cases of epitaxial growth the difference between lattice parameters does not exceed 15 % (70).

3.5.3 Conclusion.

From the preceeding work it is clear that; MgSiAlON liquids formed during reactions of the M2, M4 and M6 compositions in the 3M/4X plane, are on cooling able to crystallize into;

(i) β", which is a magnesium sialon phase, existing over a wide composition range and which nucleates and grows from magnesium sialon glass, providing there are suitable β-Si_3N_4/β'sialon nuclei present; or,

(ii) A mixture of forsterite , and β" of relatively low unit cell dimensions (ie. slightly larger than a z=4 sialon) when a slow cooling rate is employed.

These β" phases, in particular those of higher dimensions, are not stable crystalline phases as they disappear on heating at 1200 ^{o}C.

In order to investigate the crystallization of β" and its stability, and to determine whether its composition is in fact in the 3M/4X plane, a further and more comprehensive programme of heat treatment and analysis is required. The following two chapters comprise a detailed analysis of this programme.

. . .

CHAPTER FOUR.

CRYSTALLIZATION OF MGSIALON 3M/4X LIQUIDS (I) : QUENCH AND ANNEAL.

4.1 GLASS COMPOSITION, WEIGHT LOSSES, AND IMPURITIES.

It has been clearly demonstrated in the previous chapter that MgSiAlON liquids can be rapidly quenched to give glasses containing an even dispersion of precipitated β-Si_3N_4/β'-sialon crystals. This can be accomplished using compositions within the shaded sector illustrated in fig 3.1 (page 51) which are fully liquid at 1650°C ; that is within the eutectic-Si_3N_4-β'sialon (z=4.2) triangle bounded by the 1650 °C isotherm. The precipitated β' nuclei are such effective nucleants for promoting β" formation that some β" growth is unavoidable as the specimen is rapidly cooled through the 'liquidus-glass transition' region, as shown in fig 3.3 (page 55). These β'/β" crystals dispersed in the MgSiAlON glass matrix, can subsequently act as nuclei for the continued growth of β" on annealing at temperatures above the glass transition temperature.

The M6 composition was chosen for studying the growth of β"-magnesium sialon crystals because quenching an M6 liquid gives a fine even distribution of small β' crystals taking up only approximately 2% of the specimen volume with only a slight amount of β" overgrowth. The subsequent crystallization of the remaining glass may then be easily followed in stages with a substantial degree of crystalline growth occurring without impingement of adjacent crystals.

By comparison, see fig 4.1, a quenched N5 specimen which has a composition closer to the β'-sialon (ss) line than M6 and consequently has a heavier density of precipitated β' nuclei and consequently a

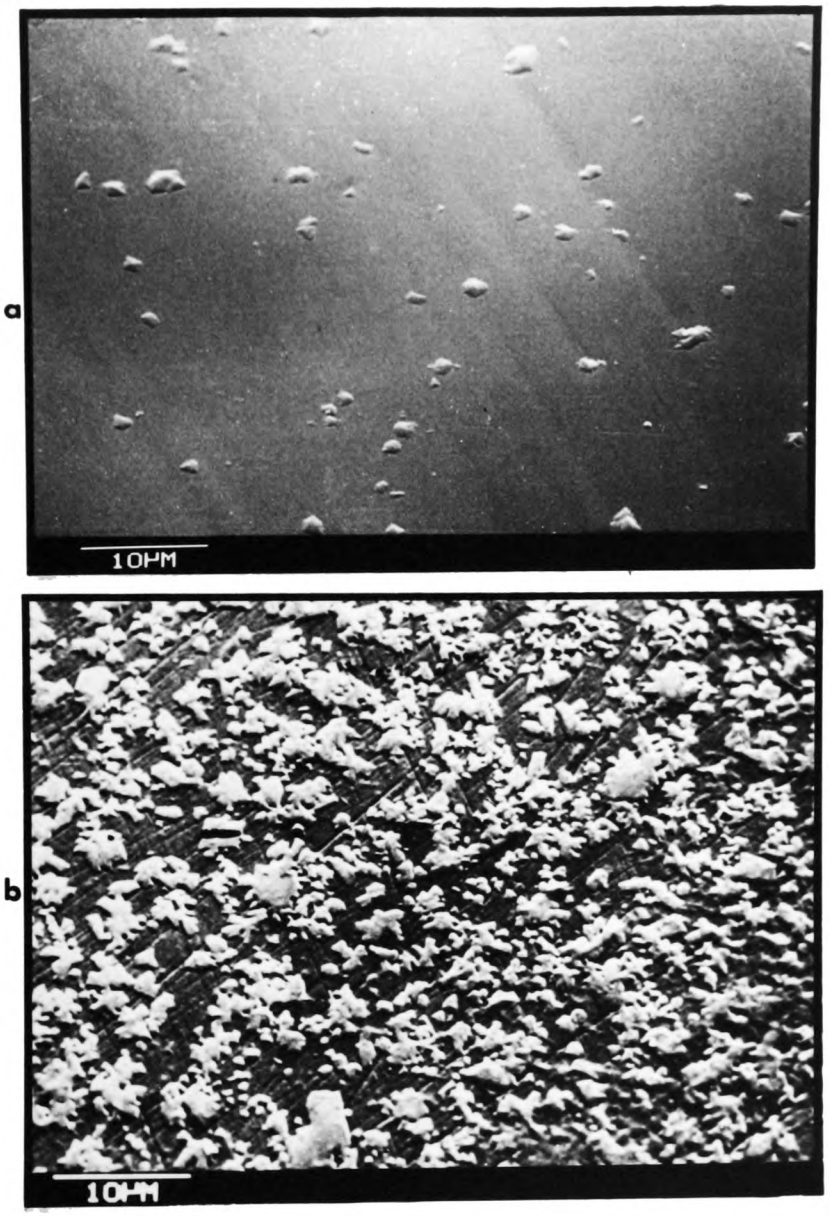

Figure 4.1

(a) SEM micrographs of quenched M6 specimen, and

(b) N5 specimen.

large proportion of the glass has crystallized as β" even on rapid quenching. The quenching of a liquid of eutectic composition gives a clear transparent glass with no β' nuclei.

An important factor with regard to studying the rate of growth of β" crystals in this M6 glass is to ensure that the glass composition is accurately in the 3M/4X plane.

A reaction time of only 12 minutes is required to give a homogenous M6 MgSiAlON liquid at 1650°C, and, this short reaction time keeps the weight losses down to between 1 and 1.5 wt%. The composition of the resulting M6 glass will be changed from that in the 3M/4X plane by an amount which is determined by these small weight losses.

The volatile species most likely to be lost from the M6 composition are MgO, SiO, and SiO_2. If all of a 1.5 wt% loss was attributed to loss of MgO (cation:anion ratio of 1:1) then the resulting cation:anion ratio of the M6 glass composition would drop from its original value of 0.7500 to 0.7467. A similar magnitude drop in the cation:anion ratio would occur if all the weight loss was attributed to SiO. If all the weight loss was attributed to SiO_2 (cation:anion ratio of 1:2) then the cation:anion ratio of the resulting M6 glass composition would increase from 0.7500 to 0.7545. Variations of cation to anion ratio of this magnitude are considered quite acceptable for the present work and no attempt was made to determine what actual species are lost from the MgSiAlON liquids during reaction. In formulating the glass compositions no allowance was made for any effect that the impurities might have on the cation:anion ratio as it was considered that the levels of impurity present would not significantly affect glass composition. However subsequent work does show that even trace amounts of impurities can significantly affect crystallization mechanisms . . .

4.2 OBSERVATIONS OF TRANSFORMATION WITH TEMPERATURE: MGSIALON GLASS (M6).

A powdered M6 glass sample was analyzed by differential thermal analysis in air to determine a suitable temperature range for studying crystallization. Part of the DTA trace obtained between 700^{o}C and 1100 ^{o}C is shown in fig 4.2.

Powdered samples of the M6 glass (as used in the DTA analysis) were annealed in air at temperatures corresponding to the initial sections of the peaks showing up in the DTA analysis, and then analyzed by X-ray diffraction in order to determine which phases have crystallized at the different temperatures. Bulk fragments of the M6 glass were also annealed at the same temperatures in a nitrogen atmosphere, and analyzed by X-ray diffraction. These X-ray diffraction results are presented in Table 4.1.

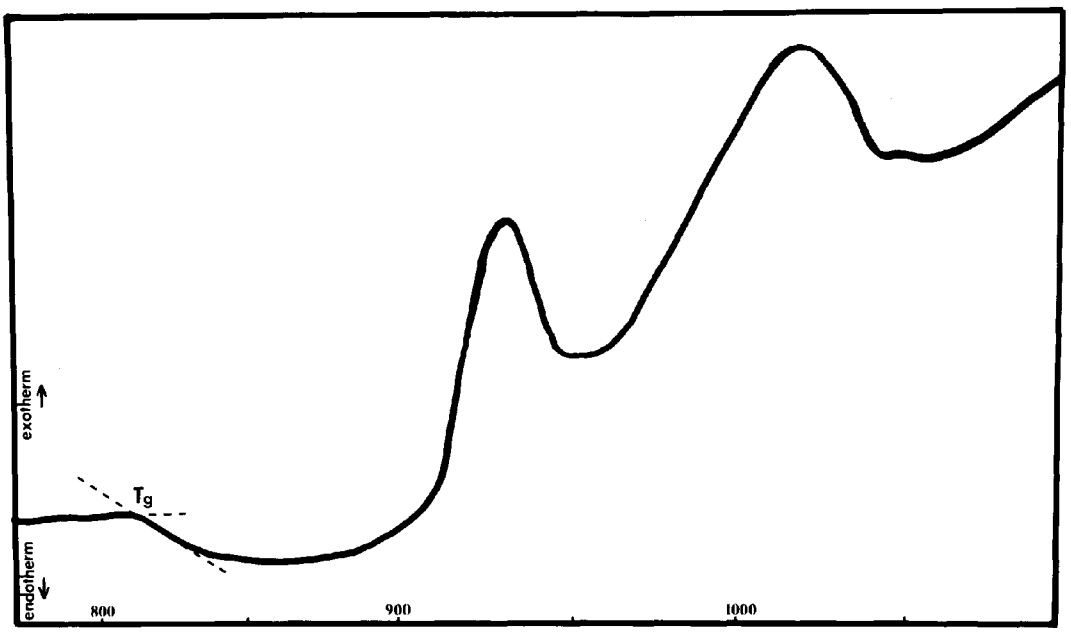

Figure 4.2

Differential thermal analysis trace of a rapidly quenched M6 MgSiAlON glass powder.

Heating rate - 10°C/min. Atmosphere - air.

Table 4.1

Crystalline phases developed in M6 MgSiAlON glass (impure) on annealing at 910°C, 1000°C, and 1300°C.

Annealing temperature and time.	Powdered M6 glass annealed in air.	Bulk M6 glass annealedin nitrogen.
910°C (12 hr)	β"-magnesium sialon (s)	β"-magnesium sialon (s)
	Forsterite (tr)	Forsterite (slight tr)
1000°C (12 hr)	β"-magnesium sialon (ms)	β"-magnesium sialon (s)
	Forsterite (m)	Forsterite (tr)
1300°C (3 hr)	Forsterite (ms)	Forsterite (s)
	Enstatite (m)	Q (w)
	other/s (w)	

The glass transition temperature for the M6 MgSiAlON glass is observed as a small endothermic step which occurs in the baseline of the DTA trace at 815°C ±5°C (fig 4.2).

The first exotherm in the DTA commences at about 870°C reaching a peak at 925°C. The X-ray diffraction results of the specimen annealed in air show that in this temperature region β"-magnesium sialon is the major phase developing. A second large exotherm begins at about 950°C and rises to a peak at 1020°C, and the X-ray results confirm that the secondary developing phase in this temperature region is forsterite.

Beyond 1100°C there is a further exotherm on the DTA trace, and the X-ray results show that at higher temperatures there is formed a

complex mixture of phases including forsterite, enstatite and at least one other unidentified phase.

The X-ray results of bulk MgSiAlON M6 glass specimens annealed in nitrogen show two major differences in the crystalline phases formed in comparison with the same glass powdered and annealed in air :

(i) Up to at least 1000°C, the only major developing phase in the bulk glass is β"-magnesium sialon. Only slight traces of forsterite form as well.

(ii) At 1300°C an unknown phase, termed Q phase, forms along with the main forsterite phase.

At 1000°C in air, oxidation reactions occurring with the finely powdered glass result in the formation of a significant proportion of the oxide product forsterite along with the oxynitride product β". At 1300°C in air a complicated mixture of oxidation products result with no β" formed.

From the preceding DTA and X-ray diffraction results it can be seen that under non-oxidising conditions with bulk specimens of M6 glass, the 900°C to 1000°C temperature range is suitable for studying the crystal growth of β"-magnesium sialon on its own, while higher temperatures will eventually involve competing forsterite and Q phase growth and possible transformations of any β"-magnesium sialon formed at lower temperatures.

The Q phase which formed along with forsterite at 1300°C cannot be identified at this stage because it is characterized by only two broad weak diffraction lines (~d spacings of 3.60 Å and 2.43 Å).

. . .

4.3 THE DEVELOPMENT OF MICROSTRUCTURE WITH TIME : M6 GLASS AT 910°C.

Specimens of quenched M6 MgSiAlON glass were annealed at 910°C for a range of times. The growth of β"-magnesium sialon crystals was followed by observation of polished and etched specimens by optical microscopy (reflected light) and by scanning electron microscopy. An optical micrograph and SEM micrographs of β" crystals that have grown in an M6 MgSiAlON glass are shown in fig 4.3. The HF acid etches the grown β" crystal in preference to the glass matrix, with the β' nuclei being left proud of the surface.

It was shown in Chapter 3 that the β"-magnesium sialon grows epitaxially on the nuclei formed during quenching. The growth rate in the initial stages of growth can be calculated by measurement, onthe SEM micrographs, of the distance between the β'/β" interface and the β"/glass interface, and dividing by the total annealing time. In doing this the following conditions were complied with ;

(i) The crystal face should be growing clearly unimpinged into a substantial area of glass matrix. This is to avoid any interference in the growth of one crystal by another.

(ii) The crystal must be orientated with its hexagonal c-axis either (a) parallel with, or (b) perpendicular to the surface of the polished section, and the growth measurements in these two different directions distinguished. This is to take account of the fact that linear growth rates of crystals are normally anisotropic.

(iii) When observing a β"-magnesium sialon crystal orientated with its hexagonal c-axis in the plane of the section surface the observed edges of the crystal faces are curved. The crystal face growing

perpendicular to the c-axis bows inward in the center, while the face growing along the c-axis curves outward in the center. Fig 4.3 shows how distances were measured between these curved β"/glass interfaces and the β'/β" interface.

(iv) A statistically significant number of different crystals measurements must be taken. This is to eliminate the effect of any local inhomogeneities in the specimen.

The % crystallization by volume was estimated by placing a square grid over low magnification SEM micrographs. The volume of residual glass as a percentage of the total volume was then measured by counting the number of grid intersection points lying on top of residual glass and calculating this as a percentage of the total number of grid points. The volume percentage of β"-magnesium sialon is then equal to (100 % - residual glass % - nucleus %). The process was repeated several times for each specimen and the result expressed in terms of the mean value ± the standard deviation.

The results of annealing specimens of an impure M6 glass at 910°C for various times between one and 20 hours in a nitrogen atmosphere are presented in fig 4.4 (a), (b) and (c), together with an EDAX (TEM) analysis of the residual glass. In fig 4.5 SEM micrographs and Guinier X-ray diffraction photographs of a pure M6 glass after quenching (a) and then after being annealed for 20 hours at 910°C in nitrogen (b) are shown.

Fig 4.6 (a) shows a SEM micrograph (back-scattered mode) of an M6 glass specimen which has been annealed for 20 hours at 910°C; and in (b) a plot of crystallinity (vol% of β") versus time for a pure M6 glass annealed at 950°C.

TEM micrographs of the pure M6 glass specimens annealed at 910°C for 20 hours are presented in fig 4.7. Together with the micrographs are the corresponding EDAX (TEM) analyses of a β" magnesium sialon crystal and the residual glass.

The density of the pure M6 glass and the annealed β" product were measured by a standard displacement method using a pyknometer (ASTM C329) and the results are presented in Table 4.3. Both samples were pulverised to eliminate closed pores, and the pyknometer filled with water and sample was evacuated overnight to eliminate trapped air bubbles.

To illustrate the necessity of having β-Si_3N_4/β'sialon nuclei present in the glass for β" growth, a clear quenched MgSiAlON glass of eutectic composition was annealed at 1000°C for 1/2 hour and 4 hours. SEM micrographs of these two specimens in fig 4.8 show that forsterite is the only crystalline phase that has developed (spherulitic morphology)

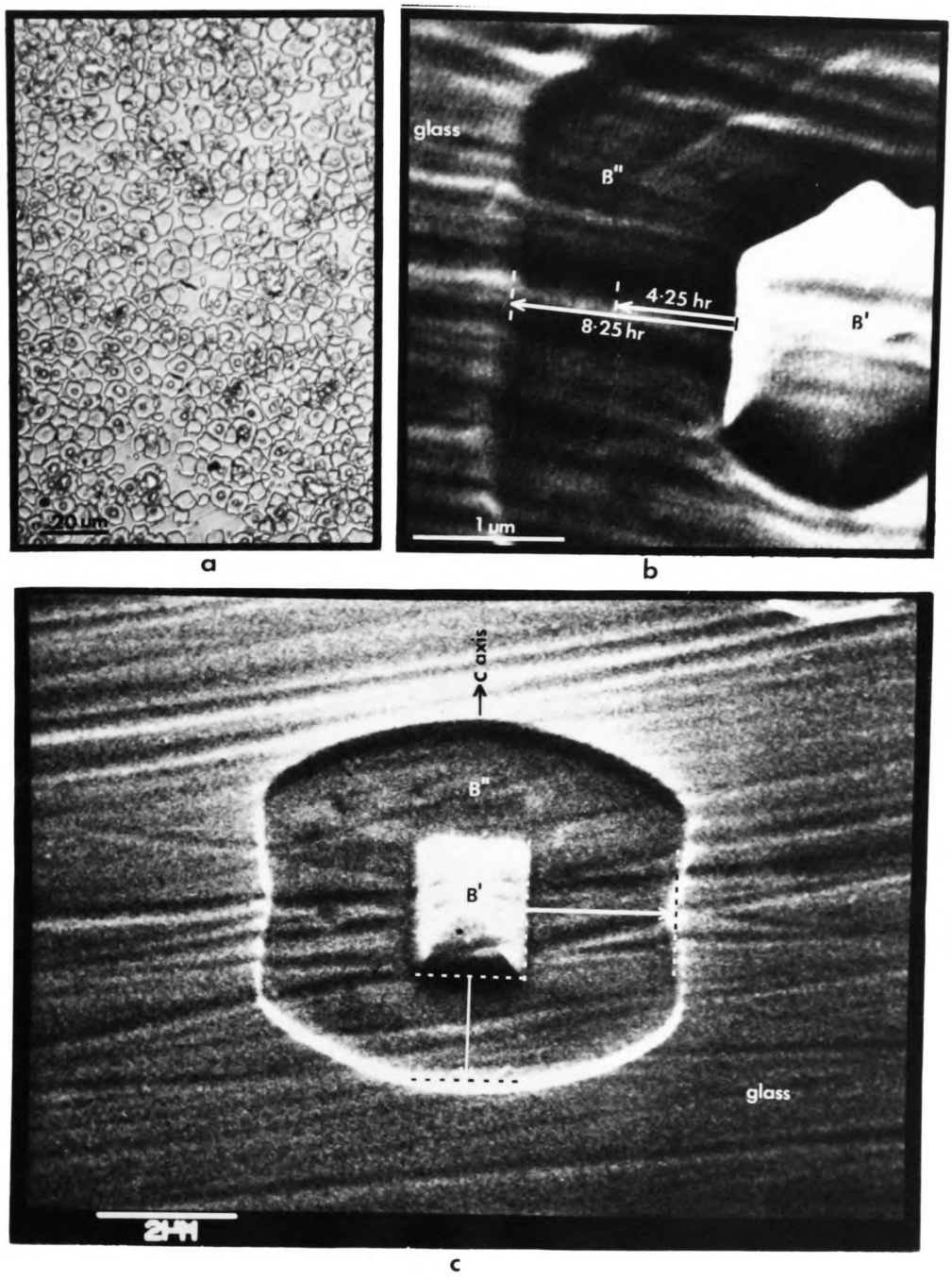

Figure 4.3

Micrographs of B"-magnesium sialon crystals grown in a MgSiAlON glass, (a) optical reflected light, (b) and (c) SEM.

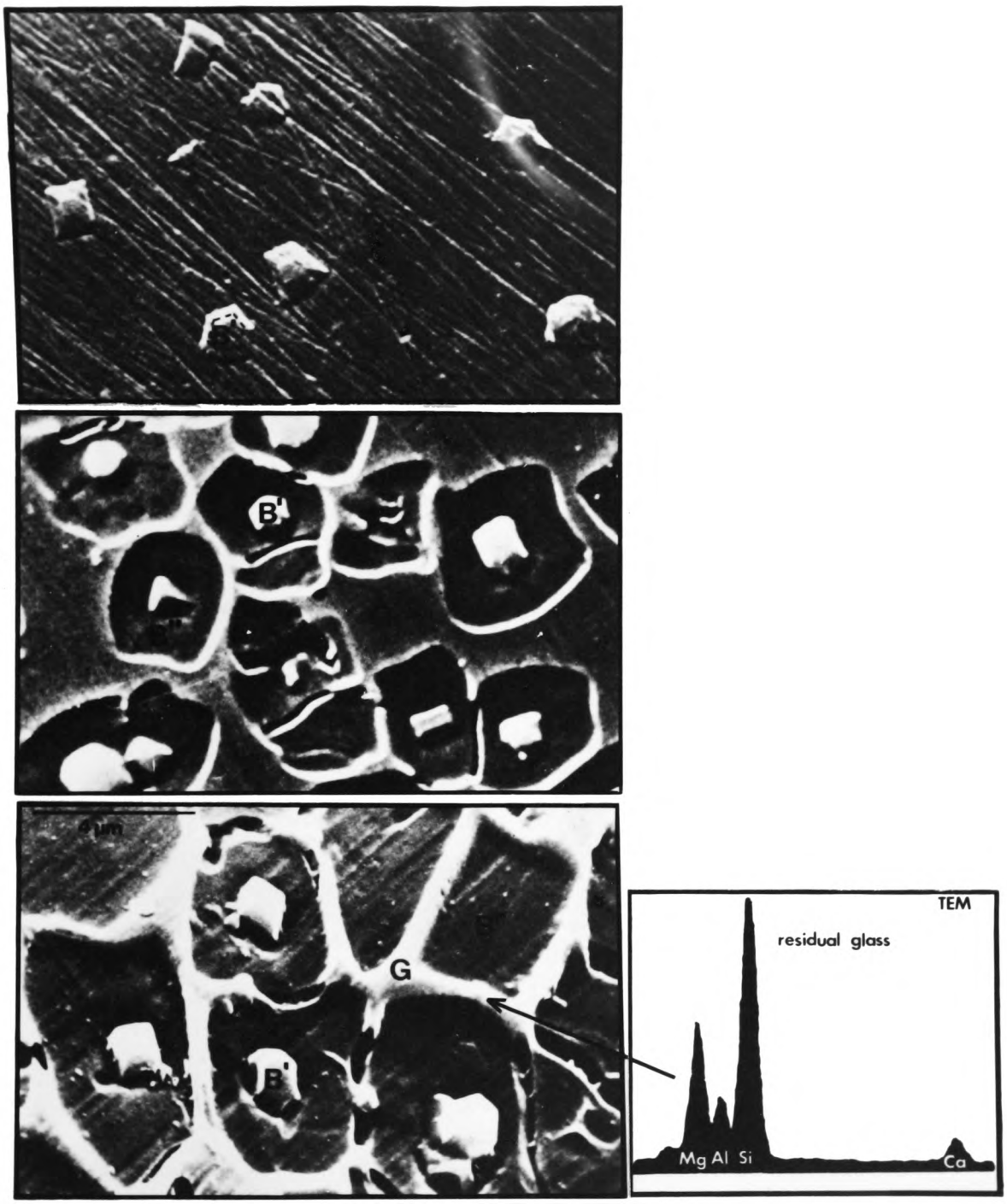

Figure 4.4

SEM micrographs showing the development of microstructure with time at a fixed temperature.

(a) rapid quenched M6 (impure) glass.

(b) M6 (impure) glass annealed at 910°C for 8 hr, and (c) for 20 hr together with an EDAX (TEM) analysis of the residual glass.

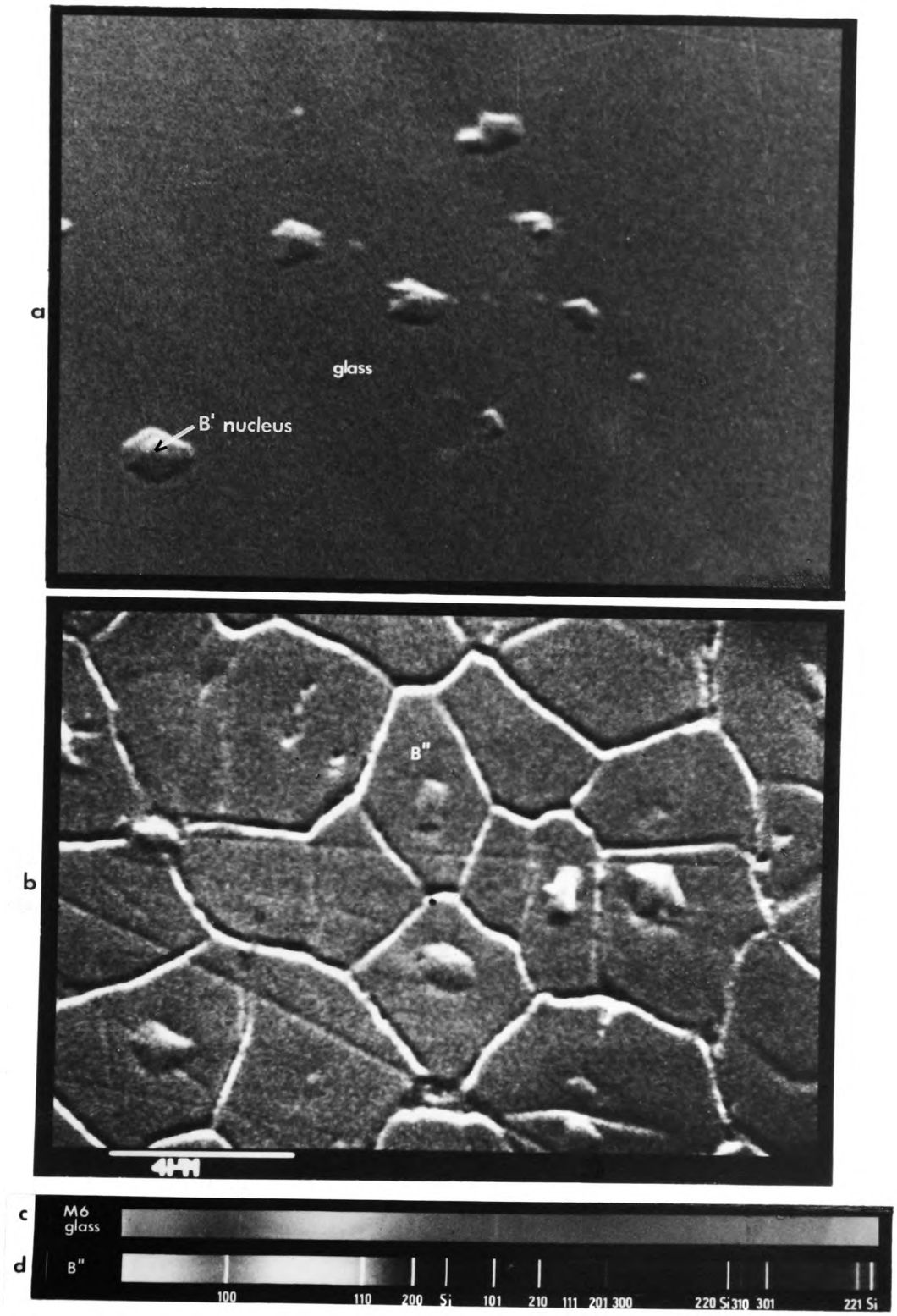

Figure 4.5

SEM micrographs (a) and (b), and Guinier X-ray diffraction photographs (c) and (d), of pure M6 glass before annealing and after annealing for 20 hours at 910°C.

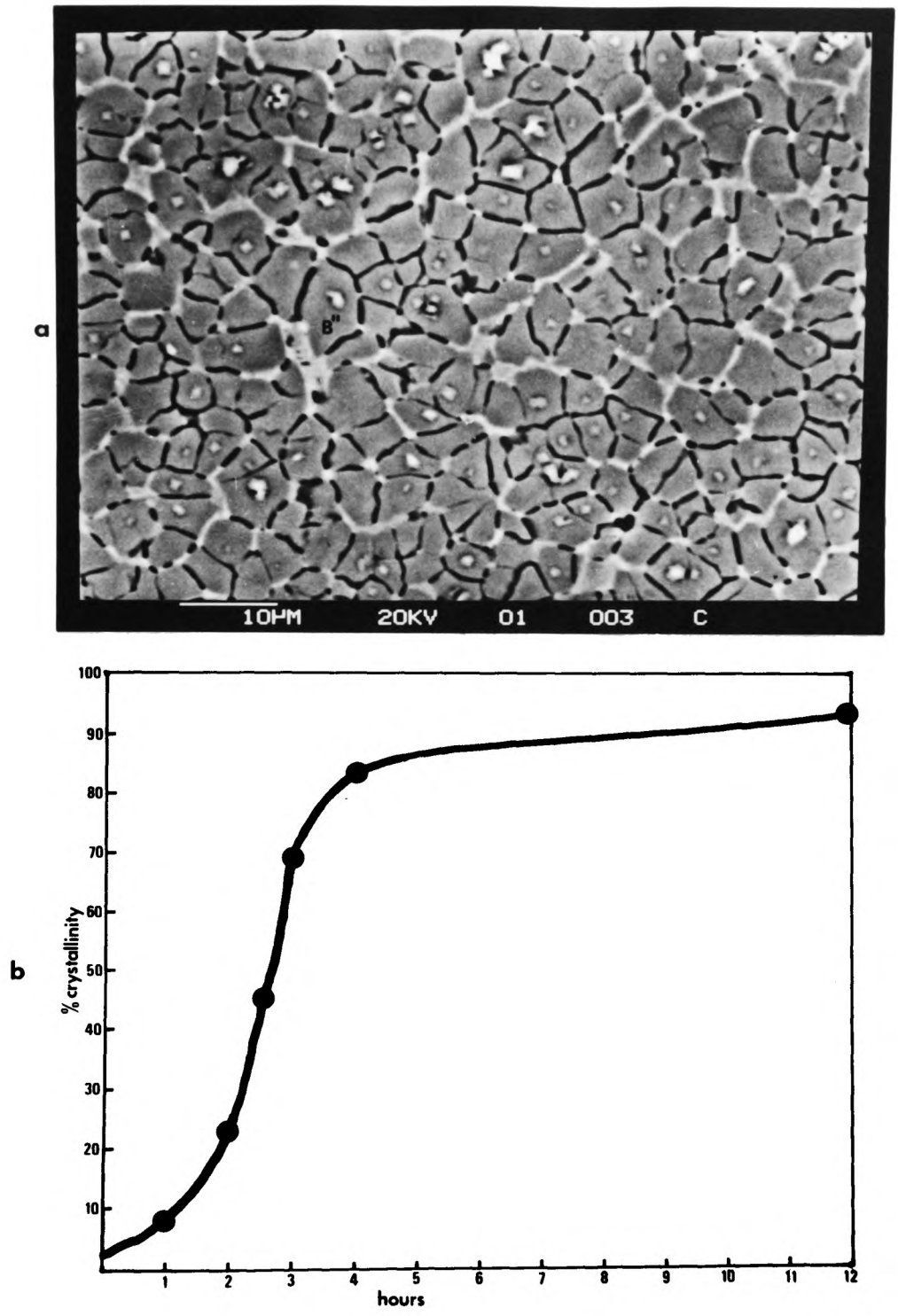

Figure 4.6

(a) SEM (backscattered mode) micrograph of an M6 glass after annealing for 20 hours at 910°C.

(b) Plot of crystallinity (vol % β") versus time on annealing at 950°C.

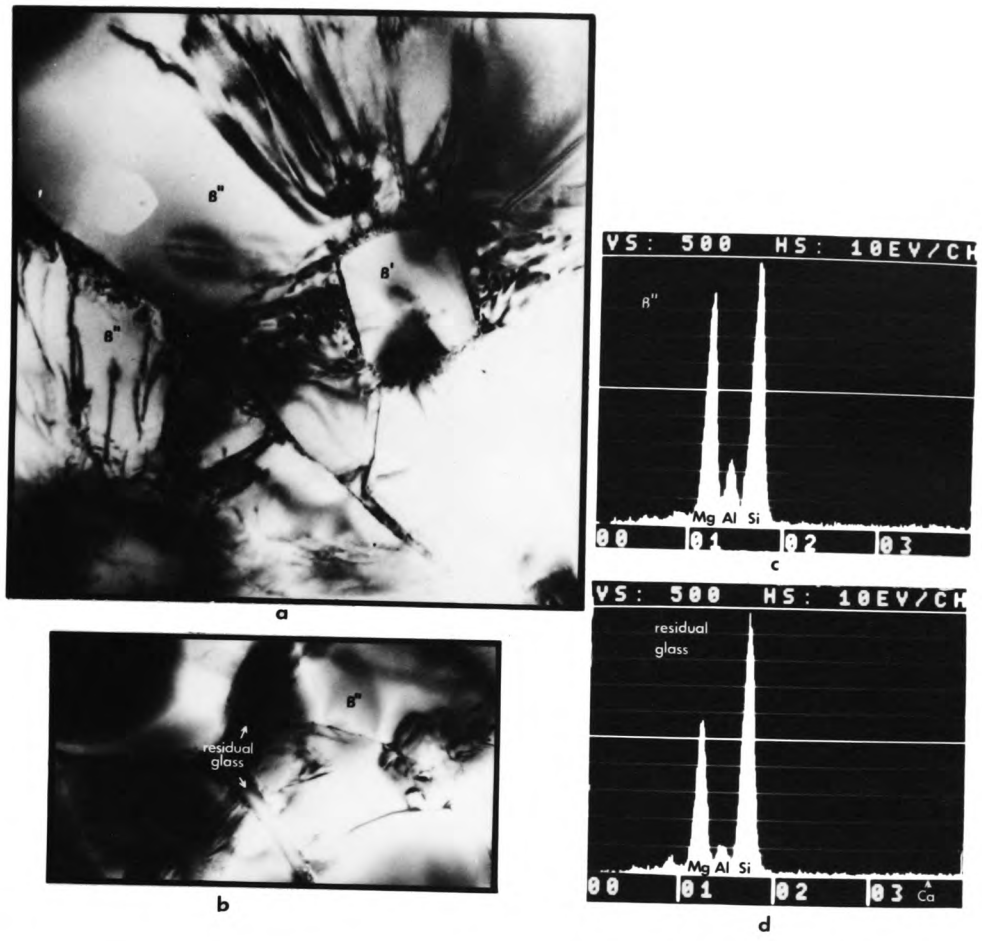

Figure 4.7

TEM micrographs (a) and (b) of a pure M6 glass after annealing for 20 hours at 910°C, together with associated EDAX (TEM) analyses of a β" crystal (c) and of the residual glass (d).

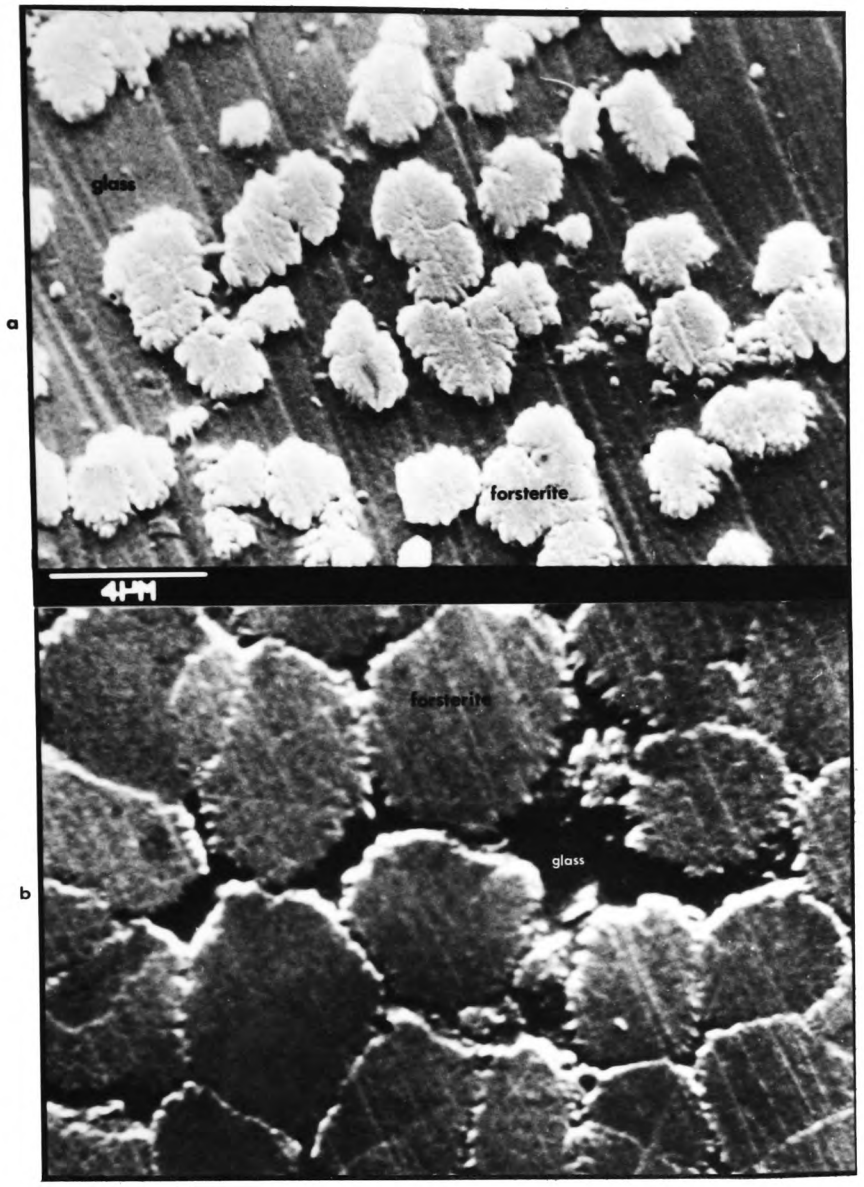

Figure 4.8

SEM micrographs of quenched MgSiAlON (3M/4X) eutectic glass annealed at 1000°C for (a) 1/2 hour (b) 4 hours.

The development of microstructure is very similar for samples prepared with both impure and pure starting materials up to about 8 hours at 910°C, but after 20 hours the pure M6 sample is more fully crystalline than the M6 glass prepared from impure grade powders. A comparison of fig 4.5 (b) with fig 4.4 (c) shows how the pure M6 glass has more completely crystallized as β". This is also illustrated in the following table:

Table 4.2

Volume percentage of phases in impure and pure grade M6 glass after annealing for 20 hours at 910°C.

impure M6		pure M6	
β" magnesium sialon	83-87 %	β" magnesium sialon	91-93 %
β' nuclei	~2 %	β' nuclei	~2 %
residual glass	11-15 %	residual glass	5-7 %

Table 4.3

Density of pure M6 glass and of annealed β" (M6).

material	density (g/cm^3)
glass M6	2.52 ± 0.02
β" M6	2.815 ± 0.02

An SEM micrograph of an M6 specimen that has been annealed at 910 ^{o}C for 4.25 hours, taken out of the furnace, then returned to the furnace for another 4 hours is shown in fig 4.3 (a) on page 81. The HF acid left a slight etch line where the β" crystal stopped growing after the first period and then starting growing again during the second period. This formed a convenient marker for the determination of the growth rates in these initial stages. From the micrograph, the linear increment of β" growth perpendicular to the c-axis for the first 4.25 hours is 0.81μm, and for the second 4 hour period is 0.73μm. This givesgrowth rates of ;

0.19 ±.01 μm/hr for the timeinterval 0-4.25 hours,

0.18 ±.01 μm/hr for the time interval 4.25-8.25 hours.

This shows that the rate of β" growth is approximately constant during these initial stages of growth.

However the fact that after 20 hours there is still a small amount of residual glass left especially at triple junctions confirms that the growth rate slows down markedly in the final stages of growth when only a small amount of residual glass remains. Annealing for longer times of up to a week produced no further crystallization in the impure or pure M6 specimens.

The progress at 950^{o}C of crystallization with time using the pure starting powders is shown in fig 4.6 (b). At this temperature the process of crystallization is virtually complete after about 4 hours, and the reduction in growth rate in the later stages can be clearly seen.

Note that the glassy regions etch proud of the β" crystal as do the β' crystal nuclei. Where however two β" crystals are in contact, preferential etching at the β"/β" boundary produces well defined

grooves, clearly evident in fig 4.4 (b) and (c).

Most of the grain boundaries in fig 4.5 (b) are these etched β"/β" grooves, with the residual glass not showing up very clearly in this lightly etched specimen. The amount of residual glass in the annealed pure M6 specimen is more clearly shown in the low magnification SEM micrograph in fig 4.6 (a) imaged in the backscattered electron mode (very lightly etched with HF). The etched out β"-β" grooves return little electron back-scatter signal and hence appear black, and the residual intergranular glass and the nuclei show out more clearly as the lighter phases (because of their higher average atomic number relative to the β" crystalline phase). This gives clear definition of the amount of residual glass left along grain boundaries and at triple points. In particular small pockets of residual glass can be seen clearly at many triple points.

There is a marked departure in composition of the residual contracting glass phase from the β" crystal composition shown in the EDAX analyses of the pure M6 specimen in fig 4.7 (d). The proportion of Mg and Al in the residual glass is significantly lower than that detected in the β"-magnesium sialon phase. Of course the extent to which the cation/anion ratio in this residual glass has deviated from its initial 3/4 ratio can not be determined due to the inability to analyze for oxygen and nitrogen.

Fig 4.4 (c) shows that there is a significant increase in the calcium level in the residual glass of the specimen prepared from impure powders, whereas the level of calcium in the residual glass of the specimen prepared from the pure powders is below the level of detection of the instrument as evident in fig 4.7 (d).

. . .

4.4 THE EFFECT OF COMPOSITION ON MICROSTRUCTURAL DEVELOPMENT.

The work presented in the previous section shows that the quenched M6 glass (3M/4X) can be almost fully crystallized as β" on annealing. Now the glass-forming region in the MgSiAlON system lies mainly below the 3M/4X composition plane, as can be seen in fig 1.4 (page24).A series of glasses with their compositions progressively adjusted more and more 'below the 3M/4X plane' were prepared and annealed to investigate how this change in glass composition affects the growth of β".

Starting with the M6 composition in the 3M/4X plane, compositions were chosen with progressively lower and lower cation:anion ratios, keeping the distance from the Si_3N_4 corner of the phase diagram approximately constant so as to maintain a similar distribution of β'-nuclei on quenching as was obtained with the M6 composition.

The five chosen glass compositions were annealed at 950°C until no further β"-magnesium sialon crystal growth was observed, in fact for very long periods to ensure that the maximum amount of β" growth had occurred (ie. 50 hours).

The five compositions (1) to (5) are listed in Table 4.4 together with their respective M/X ratios, and, the volume % of β"-magnesium sialon crystals present in the annealed specimens.

The positions of the compositions (1) to (5) are illustrated in two projections of the Mg-Si-Al-O-N triangular prism in fig 4.9, together with SEM micrographs of etched sections of the heat treated specimens.

Table 4.4

β" growth in glasses progressively below the 3M/4X composition plane.

Specimen	M/X ratio	vol% β"
(1) M6 composition.	.750	93 %
(2)	.743	65 %
(3)	.735	43 %
(4)	.720	22 %
(5)	.702	0 %

Compositions (1) to (4) after annealing at 950°C for 50 hours consisted of β", β'-nuclei and varying proportions of glass with no other crystalline species present. On observation in the SEM (HF etch) it was found that β"-magnesium sialon crystals had grown around the β'-nuclei to varying degrees depending on the cation:anion ratio of the glass, with a progressive reduction in the volume % of β" crystallization as the cation:anion ratio of this series of glass compositions is lowered below 3/4. This is shown clearly in the SEM micrographs of the four annealed specimens in fig 4.9 (1),(2), (3) and (4). Composition (5) showed no sign of any β" formation.

. . .

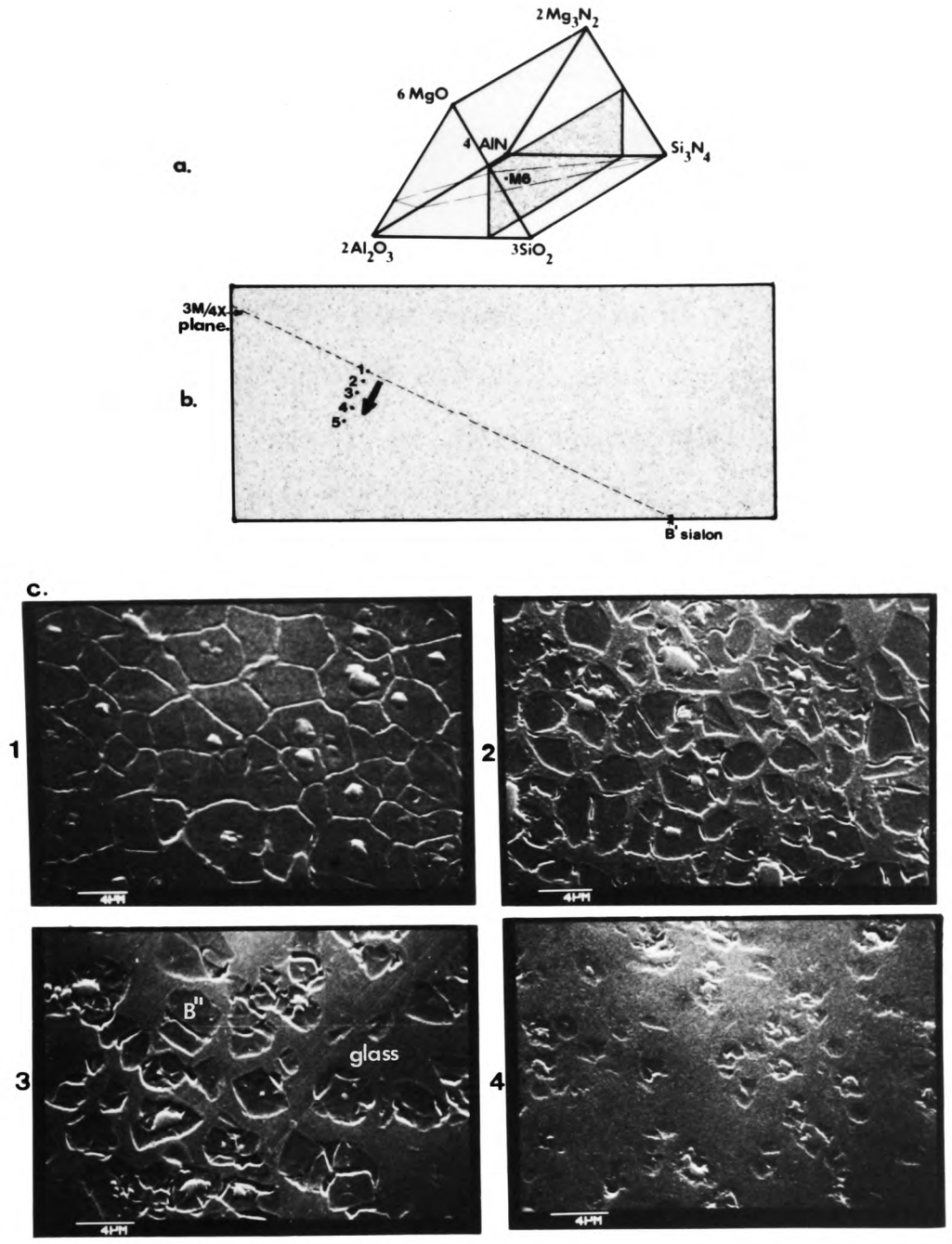

Figure 4.9

(a) Mg-Si-Al-O-N triangular prism, (b) MgSiAlON glass compositions (1) to (5) shown on a vertical plane slice of the MgSiAlON triangular prism.

(c) SEM micrographs of polished etched sections of glass compositions (1) to (4) after 50 hours heat treatment at 950°C.

4.5 THE OBSERVED RANGE OF β" COMPOSITIONS.

The M6 glass crystallized out as a β"-magnesium sialon of constant composition on annealing. Knowing the ratios of Mg, Al, and Si from the EDAX analyses, together with the fact that the M/X ratio is 3/4, fixes the O and N ratio. This then enables this M6 β"-magnesium sialon composition to be fully worked out and plotted on the 3M/4X plane of the Mg-Si-Al-O-N system as shown in fig 4.10. Having shown that the composition of this one β"-magnesium sialon (M6) is in the 3M/4X plane, the full compositions of β"-magnesium sialon crystals analyzed in other specimens have also been calculated from their cation analyses, assuming that they also have cation:anion ratios of 3/4.

The β" compositions 'a' to 'f' listed in Table 4.6 and plotted in fig 4.10 are derived from the EDAX analyses of individual β"-magnesium sialon crystals from four different specimens as listed in Table 4.5.

Table 4.5

Specimen source of β" analyses.

β"	Specimen	Preparation.
a	M6	rapid quench, annealed at 910°C.
b	M6	slow quench.
c	M4	rapid quench.
d,e,f	N5	rapid quench, annealed at 910°C.

Table 4.6

β" compositions (EDAX TEM).

Figure code.	β"-magnesium sialon composition.					Hexagonal cell dimensions (A)	
	Mg	Al	Si	O	N	a	c
a	3.20	0.67	2.13	7.07	0.93	7.875	3.105
b	3.10	0.66	2.24	6.86	1.14		
c	2.90	0.93	2.17	6.73	1.27	7.838	3.089
d	2.59	1.42	1.98	6.60	1.40		
e	2.31	1.64	2.06	6.26	1.74		
f	1.98	1.84	2.17	5.80	2.20		
z=4 sialon		4.00	2.00	4.00	4.00	7.17	3.009

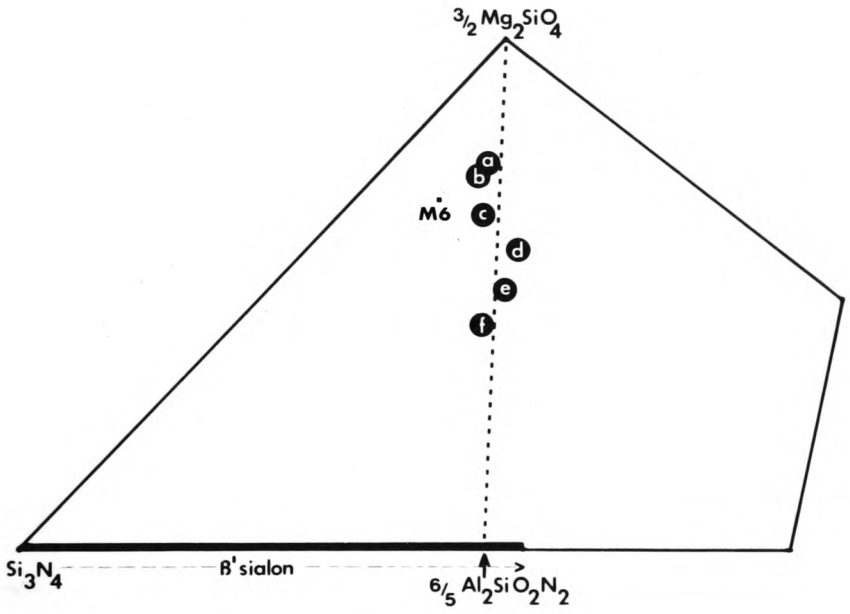

Figure 4.10

β"-magnesium sialon compositions plotted on the 3M/4X plane of the Mg-Si-Al-O-N system.

4.6 VARIATION OF B" GROWTH RATE AND PHASE COMPOSITION WITH TEMPERATURE.

The linear growth rate of β"-magnesium sialon for the M6 glass (impure) was measured over a range of temperatures above the glass transition temperature, during the initial stages where the rate is independent of time and there is no interference between adjacent crystals.

The growth rate measurements at various temperatures for M6 β"-magnesium sialon in the direction perpendicular to the hexagonal c-axis are plotted on a graph of growth rate versus temperature in fig 4.11 (a). The growth rate parallel to the c axis is lower, about 65-70% of the rate perpendicular to the c axis. SEM micrographs of β" crystals grown for 10 minutes at 1025^{o}C and 1050^{o}C are shown in (b) and (c).

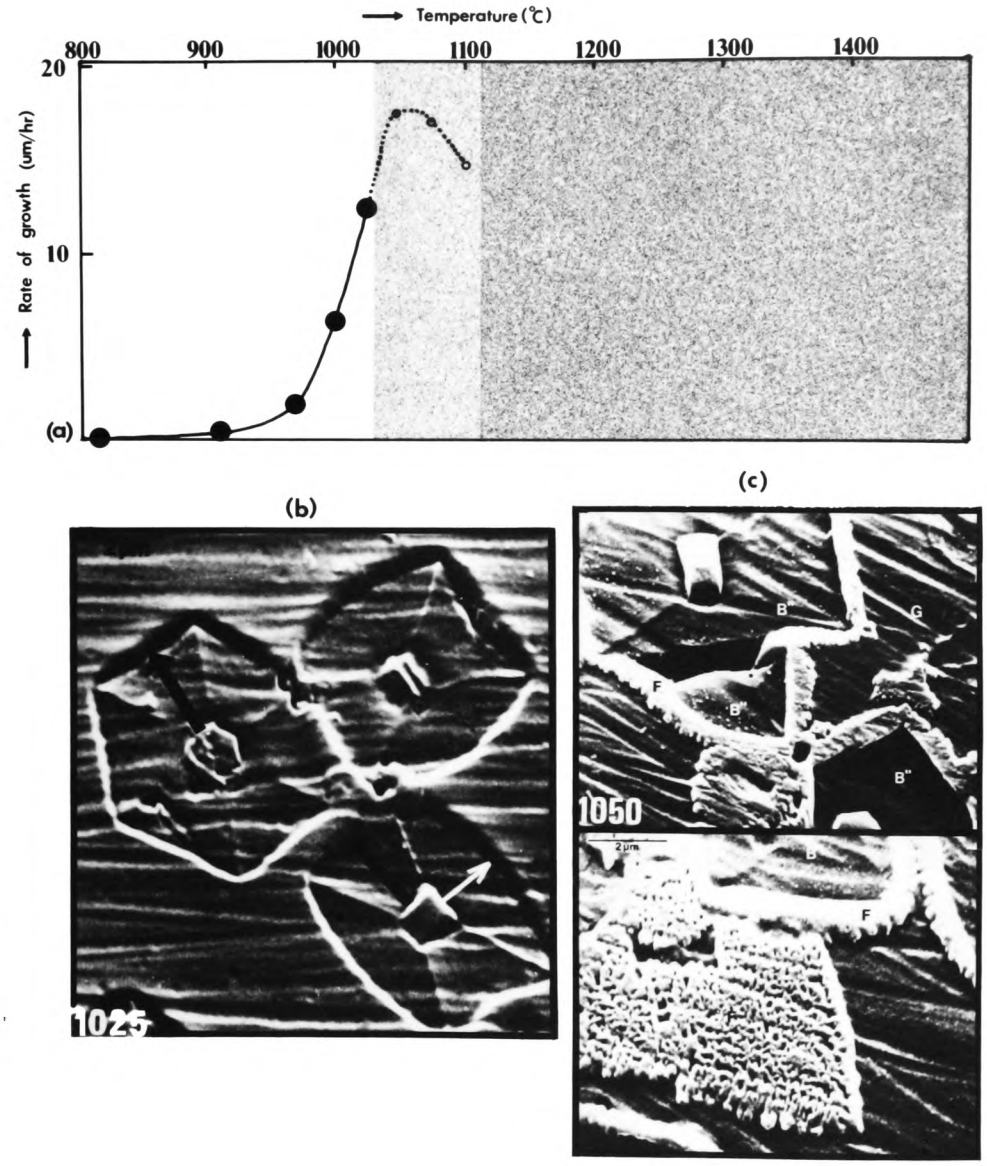

Figure 4.11.

(a) Plot of observed growth rate perpendicular to the hexagonal c-axis, R, against temperature for β"-magnesium sialon (M6 composition, impure). Region of forsterite formation shown by shading.

(b) M6 (impure) glass annealed 10 min at 1025°C, and, (c) for 10 min at 1050°C.

Between the glass transition temperature (815°C) and 1025°C, the only crystalline phase that can be observed developing in the microstructure is β". Fig 4.11 (b) shows three β"-magnesium sialon crystals that have grown in an M6 glass (impure) for 10 minutes at 1025°C. However Guinier X-ray diffraction photographs of β" grown at 890°C and at 1000°C do show very faint traces of forsterite, with the forsterite being slightly more apparent when annealing is carried out at the higher temperature of 1000°C. These trace amounts of forsterite are not identifiable in the micrographs.

However above 1025°C, the competing growth of forsterite becomes more and more apparent until it eventually becomes the major phase developing in this glass at 1300°C, see Table 4.1 page 76.

Figure 4.11 (c) shows an SEM micrograph of an M6 glass (impure) annealed for 10 minutes at 1050°C, illustrating the development of β"-magnesium sialon and forsterite together. During the annealing at 1050 °C the glass specimen cannot of course be taken instantaneously to this temperature. Here it can be seen that forsterite has nucleated at the β"/glass interface at some time during the 10 minute annealing as the temperature is rising between 1025 and 1050°C, thus blocking further growth of the β". This means that it is impossible to accurately measure the growth rate of β" in this M6 glass at temperatures of above 1025°C because of the interfering forsterite growth.

Also at temperatures above 1025°C the rate of β"-magnesium sialon growth becomes so fast that it becomes increasingly difficult to do accurate isothermal heat treatments for the short time intervals needed to catch the β" crystals in the initial stages of growth (ie. <2 min).

In fig 4.11 the growth rates for β"-magnesium sialon are plotted using black dots for temperatures 815°C, 910°C, 975°C, 1000°C, and 1025

^{o}C. Three further points at 1050^{o}C, 1075^{o}C and 1100^{o}C are also plotted using open black circles ,but it must be emphasized that these do not represent accurate growth rate measurements because of the reasons given in the preceding two paragraphs. However these points are included on the graph as they do correctly indicate that the 'growth rate versus temperature' plot is still rising at 1025^{o}C and then falls away with the competing forsterite growth. The region of forsterite growth is schematically illustrated by shading in fig 4.11.

The hexagonal unit cell dimensions of the β"-magnesium sialon crystals grown in the M6 glass over the temperature range 890^{o}C to 1000 ^{o}C remain the same, and, there is no difference in the composition of β" grown at these two temperatures as analyzed by EDAX. Therefore, the β"-magnesium sialon crystals are growing at the same composition over this temperature range in the M6 glass, as far as can be determined within the limits of analytical accuracy.

The β" growth rate measurements were not repeated for the pure M6 glass because the initial part of the 'growth rate versus temperature' curve (black dots) would still have the same shape, but with possibly slightly higher growth rate values for the pure glass.

However specimens of both the impure and pure M6 glass were annealed at temperatures above 1025^{o}C to determine if the impurities affected the crystallization product/s at these higher temperatures. Table 4.7 lists the crystalline phases present in the impure and pure M6 glasses after annealing at 1100^{o}C, 1200^{o}C, and 1300^{o}C for three hours. At these temperatures complete crystallization occurs within 10 minutes. Fig 4.11 shows SEM micrographs of M6 glass (pure) specimens annealed at 1050^{o}C, 1200^{o}C, and 1300^{o}C.

Table 4.7

Crystallization products of impure and pure M6 glass annealed at 1100°C, 1200°C and 1300°C for three hours.

Temperature	Crystalline product.	
	Impure	Pure
1100°C	Forsterite (ms) β" (m) (a=7.870 Å)	β" (s) (a=7.871 Å) Forsterite (vw)
1200°C	Forsterite (s) Q (w)	Forsterite (ms) β" (w) (a=7.83 Å)
1300°C	Forsterite (s) Q (w)	Forsterite (s) Q (w)

NB. the hexagonal 'a' unit cell dimensions of the β" phases are given in brackets.

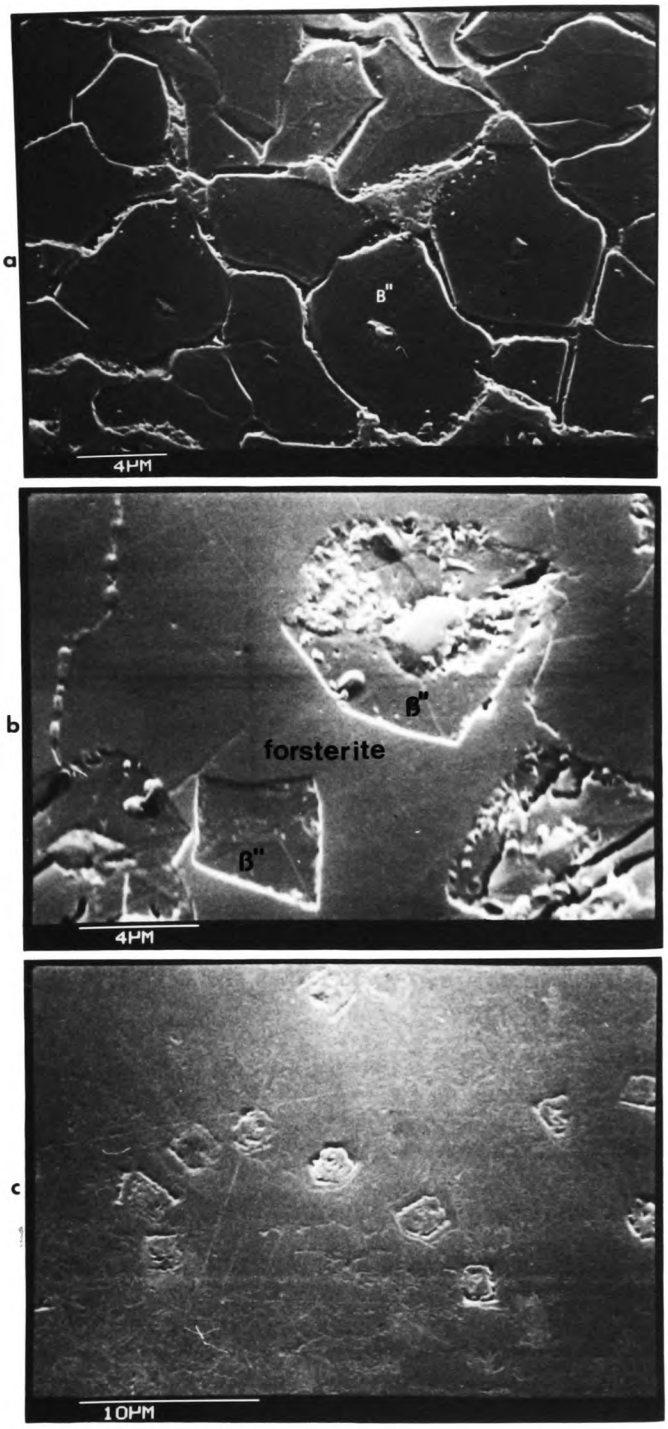

Figure 4.12

SEM micrographs showing M6 (pure) glass annealed for

(a) 10 min at 1050°C,

(b) 3 hr at 1200°C,

(c) 3 hr at 1300°C.

As shown previously, when an M6 glass containing impurities is annealed at 1050°C, fig 4.11 (c), forsterite appears to preferentially nucleate at the β"-glass interface after an initial period of β" growth. However, by comparison in fig 4.12 (a), the pure M6 glass annealed under the same conditions, shows no forsterite specifically nucleating on the β"-glass interface. The glass has crystallized mainly as β" during the 10 minutes annealing, leaving grain boundaries and triple points containing forsterite/residual glass. There has been no specific nucleation of forsterite at the β" grain boundaries.

On annealing at 1200°C, no β" crystallized in the impure glass but in the pure M6 glass a small amount of β" of relatively low dimensions is formed together with forsterite. Annealing at 1300°C gives forsterite and Q phase for both glasses. In the SEM micrograph of the M6 specimen annealed at 1300°C, fig 4.12 (c), the β' nuclei can be distinguished but the microstructure of the forsterite/Q phase matrix is not clearly delineated by the HF etch.

On annealing between 1025°C and 1100°C the presence of impurities in the M6 glass appears to promote the crystallization of forsterite relative to β". However on annealing in the same temperature region the pure M6 glass is able to crystallize mostly as β".

. . .

4.7 β" STABILITY IN NITROGEN AT ELEVATED TEMPERATURES.

An M6 glass specimen annealed at low temperatures, that is between the glass transition temperature and 1025°C, crystallizes almost entirely into β" of hexagonal unit cell dimensions a=7.871Å, and c=3.100 Å. However the same glass annealed at 1300°C crystallizes into a mixture of forsterite and Q-phase, as shown in Table 4.7 page 100. To observe the probable transformation of β" into forsterite and Q phase, a M6 glass prepared from the ultrapure powders was first annealed at 950°C to crystallize it into β", and then annealed for varying lengths of time in the temperature range 1100°C to 1300°C.

The following work is on the thermal stability of just this one particular β" composition with the above cell dimensions prepared from an M6 glass (pure). It has been shown that β" exists over quite a range of compositions and consequently there is probably a range of stabilities depending on composition.

At 1200°C this β" is not stable and it rapidly transforms into the more stable crystalline phases of forsterite and Q-phase, the transformation being complete after 15-20 minutes. At lower temperatures this transformation occurs more slowly until at 1100°C there is no observable transformation after 12 hours. The progress of the transformation was monitored over a range of temperatures by measuring the time taken for complete transformation to occur at a particular temperature. Whether complete transformation had taken place was determined by preparing a polished section, etching for a few seconds with HF, and looking for any residual untransformed etched β" in an optical microscope under reflected light.

The dependence of this transformation on temperature is shown in fig

4.13 (f), where the time taken for complete transformation is plotted against the temperature. Fig 4.13 (a) and (b) show an SEM and a TEM micrograph of a partially transformed M6 β"-magnesium sialon, having being annealed for 5 minutes at 1200°C. Fig 4.13 (c), (d) and (e) show high magnification images of the initial stages of transformation within the β" matrix.

Fig 4.14 (a) shows a TEM micrograph of an M6 β"-magnesium sialon specimen which has been completely transformed together with an electron diffraction photograph of part of the transformation product.

. . .

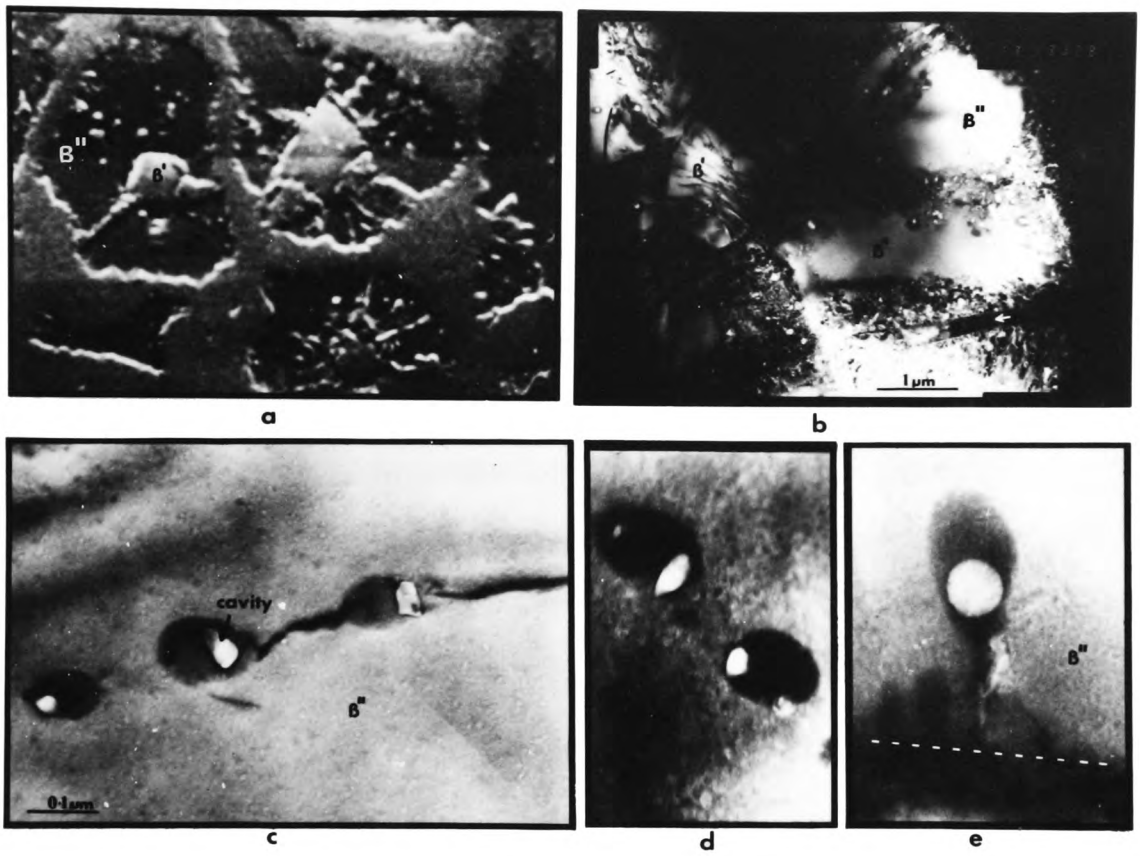

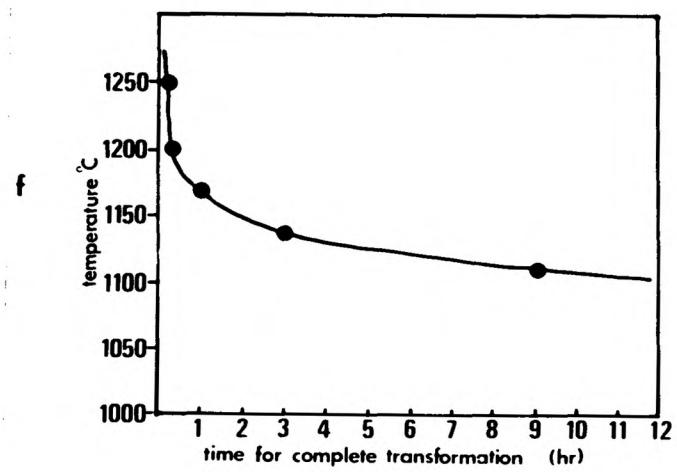

Figure 4.13

Micrographs of β" crystals partially transformed after 5 minutes at 1200°C; SEM (a) and TEM (b), (c), (d), and (e). White line in (e) shows former grain boundary residual glass.

(a) Plot of time for complete transformation versus temperature for β"-magnesium sialon of hexagonal unit cell dimensions a = 7.871 Å and c = 3.100 Å.

NB Refer to inside back cover for enlargement of 4·13(b).

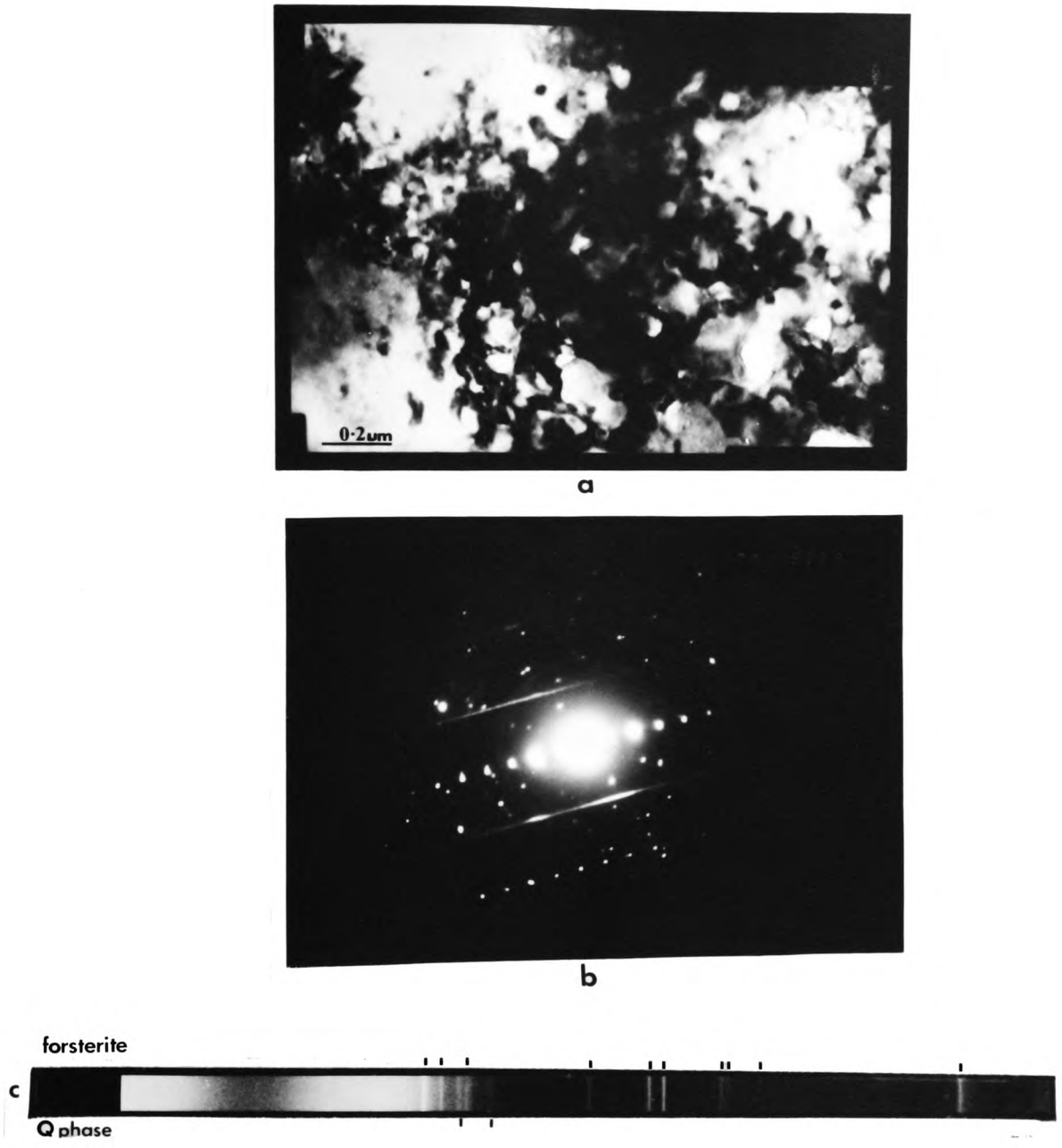

Figure 4.14

TEM micrograph (a), electron diffraction photograph (b), and Guinier X-ray diffraction photograph (c) of a β"-magnesium sialon specimen which has been completely transformed after three hours at 1200°C.

The X-ray diffraction photograph of fig 4.14 (c) shows that when a β"-magnesium sialon (M6) specimen is annealed at 1200°C it transforms into a mixture of forsterite and Q-phase (the same two phases formed when an M6 glass is annealed at 1300°C (Table 4.7) page 100.

There are only two weak broad X-ray diffraction lines for this Q-phase and the microstructure of the transformed material is so fine, fig 4.14, that no EDAX analysis or electron diffraction patterns could be specifically obtained from individual crystals. Therefore the nature of this Q-phase was not determined in the transformed β"-magnesium material. However an unknown electron diffraction pattern was obtained from a phase that was obviously not forsterite in the transformed β" material and this is shown in fig 4.14(b). This pattern shows continuous streaks which normally result from a crystal containing stacking faults and is probably Q phase.

The electron micrographs in fig 4.13 of a partially transformed β"-magnesium sialon (M6) material show the following microstructural features related to the initial solid -state transformation mechanism :

(i) The transformation is initiated at the grain boundaries and at dislocations.

(ii) The transformation proceeds by a nucleation and growth mechanism.

(iii) Initial volumes of transformed material are oval shaped and contain cavities.

Also, electron diffraction patterns taken over an area containing both β"-magnesium sialon and adjacent transformed material, show no obvious crystallographic relation between the transformed and untransformed phases .

. . .

4.8 SUMMARY AND CONCLUSIONS.

4.8.1 β" compositions.

The almost complete crystallization into β" of pure M6 MgSiAlON glass, and, the progressive reduction in β" crystallization as the metal atom:non metal atom ratio of the glass is lowered away from the 3M/4X composition plane, is conclusive evidence that the composition of this β" is in the 3M/4X plane, that is, it is a magnesium substituted β'-sialon.

Further confirmation comes from a comparison of the measured M6 β" density , 2.81 ± 0.02 g/cm^3, which agrees well with the theoretical density for a magnesium substituted β'-sialon of M6 composition of 2.813 g/cm^3. However this is only an estimate of the true M6 β" density as the sample also consists of ~5-7% residual glass and ~2% Si_3N_4

The β" compositions as plotted in fig 4.10 on page 95 indicate that β"-magnesium sialon does not necessarily crystallize with the initial glass composition. For example, the β" that has grown in the quenched M6 glass specimen has grown at a composition to the right of the overall M6 composition. With the annealed N5 specimen, β" crystals grew over a range of compositions, and the three examples of these plotted show the same tendency to be to the right of the overall N5 composition. The M4 B" would have crystallized from a liquid with a composition in a line between the M4 and eutectic compositions, and this M4 B" composition is to the right of this line.

The proximity of these β" compositions to the Mg_2SiO_4-$Al_2SiO_2N_2$ line in the 3M/4X plane, suggests these β"-magnesium sialons with relatively high levels of Mg substitution tend to exist over a specific composition region along this line, that is, given by the equation;

$$Mg_x\ Al_{4-x}\ Si_2\ O_{4+x}\ N_{4-x} \quad . \quad . \quad .(14)$$

where $x = m/2$.

It has been shown that the initial growth rate of β" crystals in the M6 glass is approximately constant, but fig 4.6 (b) page 84 shows that in the later stages of crystallization the crystal growth rate declines and becomes insignificant after long periods (20 hr at 910 ^{o}C), hence preventing complete crystallization of the M6 glass.

A likely explanation for this decline in growth rate after long annealing times and the inability to crystallize the last 5-7% of the glass, is a transition from an initial interface-controlled growth to diffusion-controlled growth.This would, in turn, be brought about by :

(i) increasing departure in the composition of the advancing β"-magnesium sialon phase and the contracting glassy matrix.

That this does occur is shown by the difference between the EDAX analyses of the β" crystal and the residual glass in fig 4.7 page 85. Any departure of M:X ratio from 3/4 in the contracting glassy matrix would also prevent the crystallization of the last remaining glass as β".

(ii) increasing impurity concentrations in the contracting glassy matrix.

Calcium impurities in the starting materials are not incorporated into the β"-magnesium sialon structure and become concentrated in the residual glass as crystallization proceeds. This is clearly shown in the EDAX analyses of the residual glass in the annealed 'impure' M6 specimen of fig 4.4 (d) page 82, but this is not such a significant factor for the pure M6 glass where no Ca was observed in the residual glass (fig 4.7 (d) on page 85).

4.8.2 Effect of impurities on β" crystallization.

Calcium is the only impurity which is observed to have an effect on the crystallization of B" from the M6 MgSiAlON glass, the calcium being concentrated in the residual glass. The size of a calcium ion relative to Mg, Al and Si ions is shown in a list of ionic radii for several metal ions in Table 4.8. These ionic radii are just a guide to the actual atomic sizes in the β" crystal as the crystal bonding is partly ionic and partly covalent.

The percentage ionic character of the bonding in Si_3N_4 is approximately 30 % and the effect of considerable magnesium substitution would be to increase the ionic character of the bonding. Now using the plot of 'electronegativity' versus '% ionicity in bonding', given in reference (85), for the M6 β" composition gives a value of 47% ionic bonding, or approximately 50:50 ionic:covalent bonding.

From Table 4.8 it can be seen that the Ca^{+2} ion is considerably larger than the Mg^{+2}, Al^{+3}, and Si^{+4} ions, and apparently being too large to fit into the β"-magnesium sialon lattice is continuously rejected at the advancing β"crystal/glass interface, thus concentrating in the residual glass.

The presence of impurities in the impure M6 glass promotes the crystallization of forsterite relative to β" at temperatures in the 1025-1100 ^{o}C region, as is illustrated in Table 4.7 page 100 and fig 4.11 (c) page 97.

An explanation of this may be, that with the growth of β" crystals in the early stages of crystallization, a significant concentration of rejected impurity calcium atoms builds up at the advancing β"-glass interface where this triggers off the nucleation of forsterite. Calcium

Table 4.8

Ionic radii of metal ions, (71).

Ion	Radius for 6-coordination	Observed coordination number	Approx.ionic char. of bond with oxygen,(%).
Si^{+4}	0.42	4	48
Al^{+3}	0.51	4 , 6	60
Mg^{+2}	0.66	6	71
Impurities.			
Fe^{+3}	0.64	6	54
Fe^{+2}	0.74	6	69
Ca^{+2}	0.99	6 , 8	79

can in fact partially replace magnesium in the forsterite lattice at temperatures above 1000°C (72). Also calcium occurs only in 6-fold coordination with oxygen, and in forsterite magnesium is 6-fold coordinated to oxygen whereas in β" magnesium is 4-fold coordinated to oxygen.

When the pure M6 glass was annealed at 1200°C for three hours some β"-magnesium sialon of relatively low unit cell dimensions (a = 7.83 Å) crystallized along with the forsterite as shown in Table 4.7 and in fig 4.12 (b). Now we have seen from section 4.7 that β" with unit cell dimensions of a = 7.871 Å is completely unstable at 1200°C, transforming rapidly to forsterite and Q-phase within 15-20 minutes. It seems that at higher temperatures such as 1200°C, β" compositions with lower unit cell dimensions and hence low magnesium contents are more stable.

4.8.3 The thermal stability of β" (M6).

The M6 MgSiAlON glass crystallizes into a high magnesium content β"-magnesium sialon at low temperatures because it is kinetically favoured. This is common in silicate systems where small differences in free energy between phases of similar composition often results in the preferred growth of kinetically preferred intermediate metastable phases. The crystallization proceeds readily because the compositions of the β"-crystal and M6-glass are similar and the process does not become diffusion controlled until the final stages where the residual glass composition changes markedly. That is, the diffusion paths necessary for β" crystal growth are very short. However, if the composition of the glass is significantly out of the 3M/4X composition plane then as the β" crystals grow the diffusion paths rapidly become longer and longer and only a limited amount of β" growth can occur, as shown in fig 4.9 page 92.

However, without β-Si_3N_4/β'-sialon nuclei present, for example in a clear glass of the eutectic composition, no β"-magnesium sialon growth occurs at all. This is shown with a clear quenched glass of the eutectic composition where instead of B", forsterite crystals with a spherulitic morphology grow, extemely slowly at 910^{o}C but quite quickly at 1000^{o}C as is shown in fig 4.8 on page 86. The M6 glass is only able to reduce its free energy by crystallizing as metastable high magnesium content β" as long as the work required for nucleation is substantially reduced by the presence of the very potent β/β' nuclei. The reasons for the effectiveness of these nuclei in the nucleation of β" have been outlined on page 69.

At higher temperatures above 1150^{o} C, the atoms have sufficient mobility for substantial structural rearrangement to take place and the

metastable β" formed at lower temperatures transforms into the stable phases for the system of forsterite and Q-phase.

4.8.4 Morphology of the initial stages of the β" transformation.

The β"-magnesium sialon transformation is heterogeneous ; that is, at an intermediate stage the assembly can be divided into microscopically distinct regions of which some have transformed and others have not as shown in fig 4.13 page 105. The transformation thus begins from identifiable centres in the original phase, a process called nucleation.

The free energy changes associated with the solid state nucleation and initial growth of say, B (transformation product) within a parent matrix A, can be discussed in terms of the following three contributions :

(i) The creation of a volume of transformed material giving a volume free energy reduction.

(ii) The creation of an parent/product interface giving a free energy increase.

(iii) In general the transformed volume will not fit perfectly into the space originally occupied by the matrix and this gives rise to an elastic strain energy proportional to the volume of the inclusion.

As observed in fig 4.13, the initial stages of the β" transformation take place at :

(a) Grain boundaries.

(b) The heavy concentration of dislocations surrounding the β'-Si_3N_4 nuclei.

(c) Along dislocations running from the β'-Si_3N_4 nucleus outward through the β" crystal.

These microstructural features, grain boundaries and dislocations, and other features not obviously present in the β" crystals such as stacking faults, interstitial atoms, and vacant lattice sites, are comparatively unimportant in a description of the equilibrium state of a crystal, but their presence may be fundamental to the process of transformation, as is the case here.

Now, the essential driving force for a phase transformation is the lowering in the system's free energy in proceeding from the initial to the final configuration of the assembly. However, there are two factors leading to increases in free energy :

The first, the 'interfacial energy' term tends to dominate in the initial nucleation stage where the surface area/volume of a very small transformed region is high. The catalysing of this nucleation process depends on reducing the net surface energy needed to form a nucleus. This can happen when the formation of the nucleus involves the destruction of an existing surface, the free energy of which helps to provide the free energy for the new surface. This is why in the transformation of the β", the nucleation process initiates at the surfaces already present, that is at grain boundaries and dislocations. The minimization of this interfacial energy term can be achieved by the transformed inclusion taking the shape of a sphere.

The second term involving an increase in energy is the 'elastic strain energy' term. For a small transformed particle nucleating in a parent matrix the strain energy of an incoherent particle is a function of its shape, and the transformed volume will form a shape that

minimizes this energy. Now the β" (hexagonal) and the main transformation product forsterite (orthorhombic) are of completely different crystal structures, and electron diffraction patterns show no crystallographic relation between these two lattices. Therefore it is unlikely that any coherent or semicoherent interfaces form and the transformed inclusion is said to be incoherent. Nabarro (73) and Lee et al (74) have shown that the elastic strain energy of an incoherent ellipsoidal precipitate approaches zero as the precipitate shape becomes a thin disk, while reaching a maximum value when the shape becomes spherical.

Therefore unless the interfacial free energy is severely anisotropic, the minimization of both the interfacial energy and elastic strain energy terms should result in a shape which is a compromise between a thin disk and a sphere, that is an oblate ellipsoid. Such is the shape of the volumes of transformed material in the initial stages of the transformation of the M6 β"-magnesium sialon as shown in fig 4.13 (c), (d) and (e).

A striking feature of each small volume of transformed material is the presence of a cavity. The considerable volume misfit between the rather open 'phenacite' β"-magnesium sialon structure (density 2.81 g/cm^3) and the main transformation product forsterite (density 3.22 g/cm^3) apparently produces so much elastic strain that to relieve this a cavity is formed within the transformed volume. In this case it is energetically more favourable to form a cavity within the transformed inclusion with its new interface, than, for this elastic strain to be accomodated by plastic flow or diffusion.

These discussions on the M6 β"-magnesium sialon transformation

mechanism describe only the transformation morphology in the initial stages. The composition, structure and distribution of the second transformation product, Q-phase, are not known and therefore a detailed analysis of how the β"-magnesium sialon structure decomposes into the two product phases needs further investigation.

. . .

CHAPTER FIVE

CRYSTALLIZATION OF MGSIALON LIQUIDS (II) : SLOW COOLING.

5.1 SLOW COOLING RATE.

The work of the previous chapter has shown that MgSiAlON liquids (3M/4X) quenched into the glassy state containing suitable nuclei can be annealed into β", a metastable crystalline state. Now, slow cooling of such MgSiAlON liquids in the 3M/4X composition plane might be expected to result in the crystallization of the equilibrium phases for the system, that is, forsterite, spinel, β'-sialon or possibly some of the polytype phases close to the 3M/4X plane which can accomodate some magnesium such as 15R.

Two MgSiAlON specimens that are fully liquid at 1650°C,

(i) composition E, the eutectic composition,

(ii) composition D (see fig 5.11 page 135) with a higher Al content than the eutectic,

were reacted at 1650°C for 15-20 minutes and then slow cooled. The cooling was done by slowly lowering the crucible down the vertical furnace giving a cooling rate of approximately 10°C per minute. The phases detected by X-ray diffraction are presented in Table 5.1 together with a brief description of the morphology of the crystals as observed by microscopy.

Table 5.1

Phases present in D and E MgSiAlON compositions after slow continuous cooling.

Specimen.	Crystalline phases.	Crystalline morphology.
E	Forsterite (s)	coupled with β", and long individual macro-crystals.
	β" (m) (a=7.728 Å)	coupled with forsterite.
D	Forsterite (s)	coupled with β", and faceted individual crystals.
	β" (m) (a=7.754 Å)	coupledwith forsterite, and some individual crystals nucleated on β'
	β'-sialon (tr)	small precipitated crystals (~.2μm)

Fig 5.1 shows two optical micrographs (reflected light) of representative areas of the eutectic composition specimen, after reacting at 1650°C for 15 minutes and slow cooled at approximately 10°C per minute; together with a Guinier X-ray diffraction photograph showing two sets of diffraction lines, one set from forsterite and one set from β"-magnesium sialon.

Fig 5.2 shows a selection of seven SEM images from the large areas of duplex microstructure which is only just resolvable in the optical micrograph of the preceding figure. Fig 5.2 (g) and (h) show EDAX (SEM) analyses of the two phases in this microstructure, β" and forsterite, The etch used to show this microstructure is hot HCl for 2 minutes

which has etched away the forsterite phase leaving the B"-magnesium sialon phase proud.

This slow cooled eutectic liquid has solidified into a porous crystalline solid consisting of two crystalline phases, forsterite and B"-magnesium sialon. The β" phase has a very low level of magnesium substitution as can be seen from fig 5.2 (h). There are only small pockets of residual glass in the specimen (eg. shown by an asterisk in fig 5.1 c) accounting for approximately 5% volume of the specimen.The porous appearance of the specimen is similar to the bloated M4 specimen discussed on page 66.

The morphology exists on two distinct scales;

(i) long narrow macro-forsterite crystals often lying parallel to each other, and inbetween these,

(ii) a much finer structure consisting of large volumes of coupled forsterite/β" duplex microstructure similar to that found in a eutectic structure.

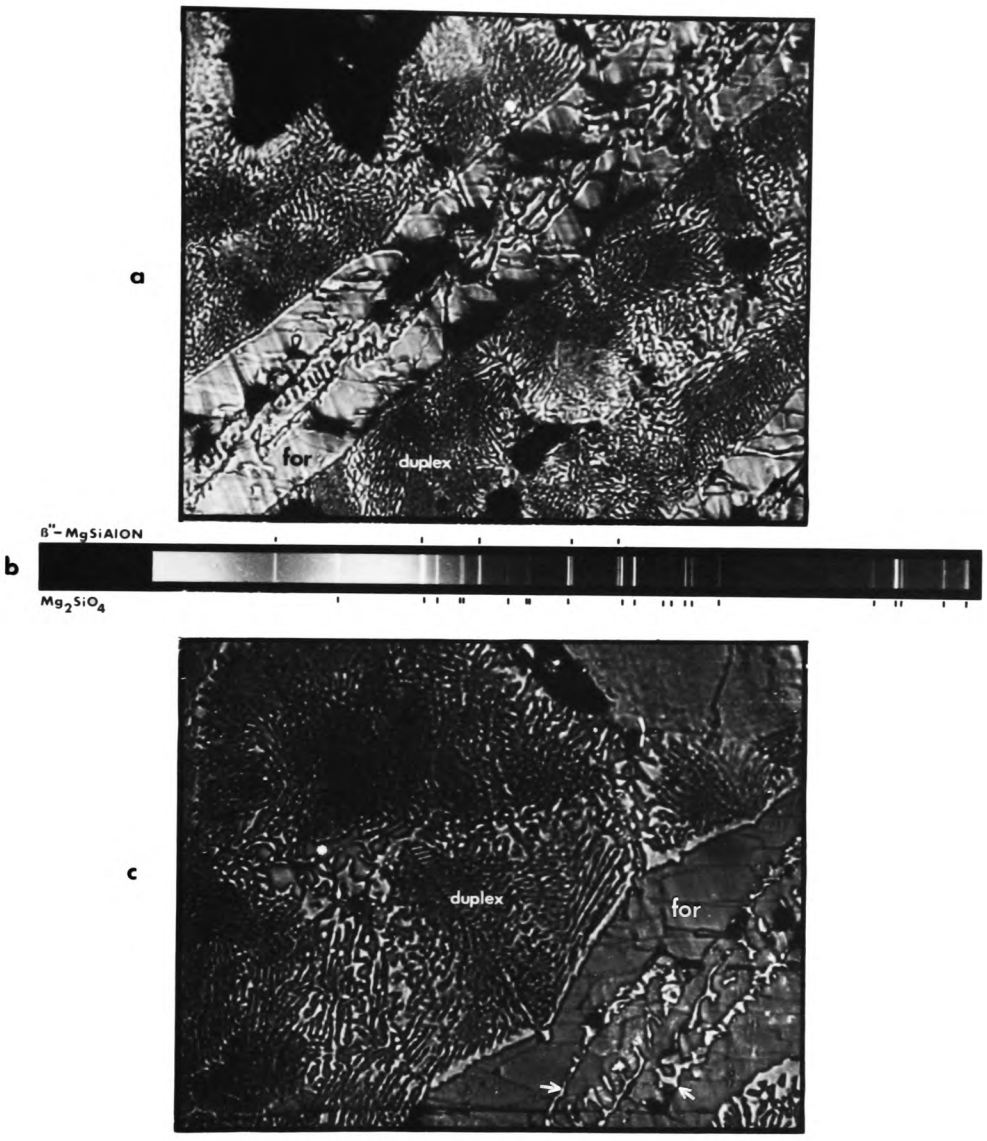

Figure 5.1

Optical micrographs (a) and (c), together with (b) a Guinier X-ray diffraction photograph of a eutectic composition MgSiAlON liquid (3M/4X) specimen, reacted for 15 minutes at 1650°C and slow cooled.

Etch - hot HCl for 2 minutes.

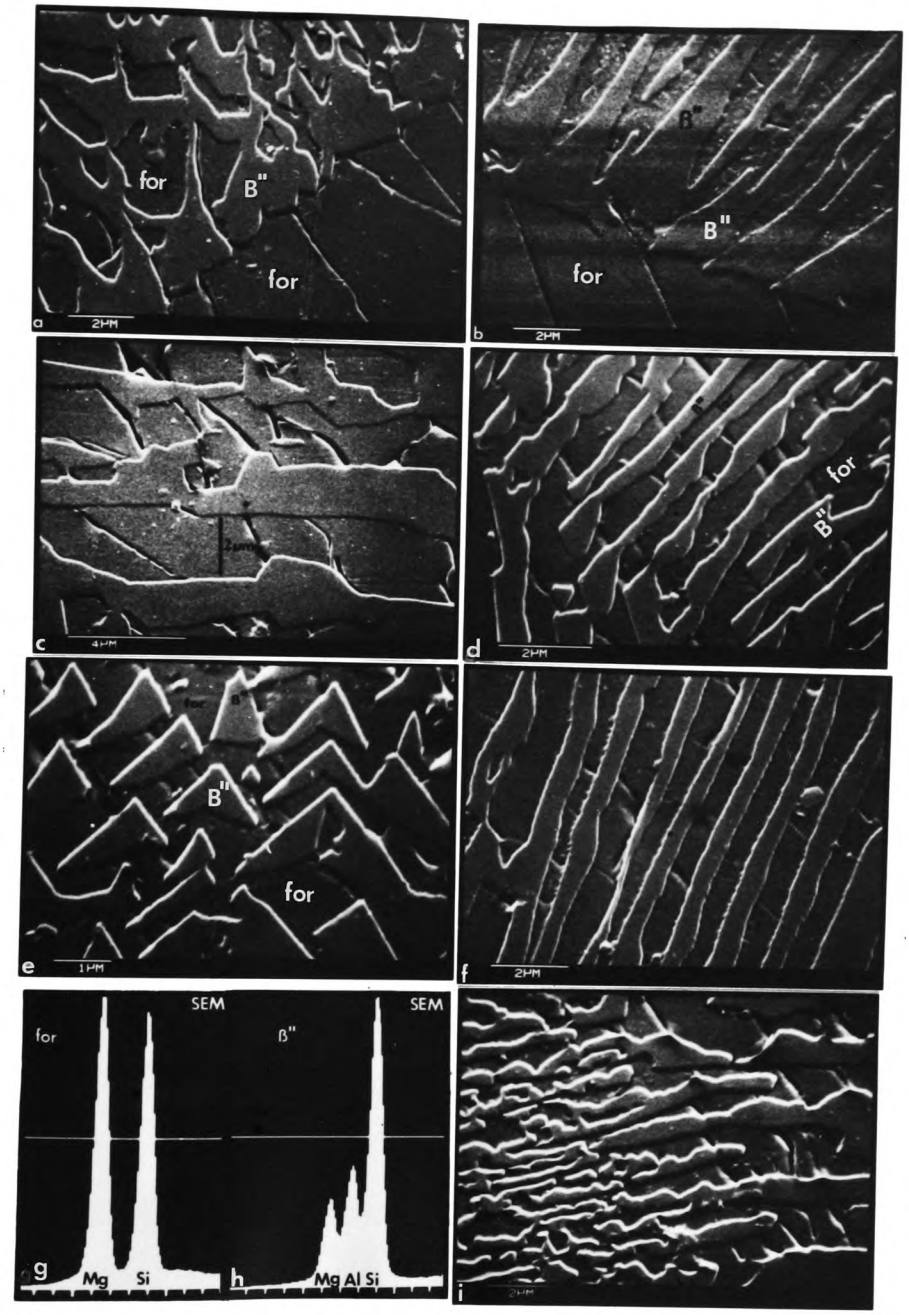

Figure 5.2

SEM micrographs of the duplex areas of a eutectic composition MgSiAlON liquid (3M/4X) reacted at 1650°C for 15 minutes and slow cooled.

etch - hot HCl for 2 minutes.

The following microstructural features are of particular note:

(a) The long narrow macro-forsterite crystals have an anomalous morphology : they are not solid crystals but have volumes of ß" within them - shown by white arrows in fig 5.1 (c).

(b) The ß" appears to have nucleated and grown at the surface of the macro-forsterite crystals, and then, coupled growth of the two phases has progressed outwards into the liquid. Fig 5.2 (a) and (b) show two examples of the 'macro-forsterite/coupled' interface.

(c) There is a wide variety of spacing between forsterite and ß" phases in the duplex structure, eg. a 2μm spacing in fig 5.2 (c) down to an approximately 0.2μm spacing in the left part of fig 5.2 (i).

(d) The orientation of the duplex structure is varied.

Fig 5.3 and fig 5.4 show TEM electron micrographs and EDAX (TEM) analyses of two representative parts of the MgSiAlON liquid 'D' after reacting at 1650°C for 20 minutes and slow cooling.

The D specimen crystallized into a porous solid mixture of forsterite and B" with approximately 5-10% of residual glass. There are two different crystal morphologies apparent in the specimen.

(a) Faceted crystals of both forsterite and ß"-magnesium sialon.

(b) Large regions of coupled duplex forsterite/ß"microstructure, approximately 70%.

Fig 5.3 (a) shows a faceted forsterite crystal which, on growing, has almost completely enveloped a faceted ß"-magnesium sialon crystal, which itself has nucleated on a small ß'-sialon particle. The EDAX

(TEM) analyses confirm the identity of the three crystalline phase present.

Fig 5.4 (a) and (b) show the coupled duplex microstructure which makes up approximately 70 % by volume of the D specimen. This 'eutectic-like' microstructure consists of forsterite and β" growing by a coupled (or cooperative) mechanism.

The EDAX (TEM) analyses of the β" phase in the duplex structure shown in fig 5.4 (c) is identical with the β" crystal of fig 5.3 (c), which has grown by nucleation and growth arounda β′nucleus.

Electron diffraction patterns taken of the duplex structure show that the forsterite/β"-magnesium sialon interface is incoherent with their being no obvious crystallogaphic relationship between the two phases (ie. no rows of diffraction spots of one phase were observed to obviously line up with rows of the other phase).

. . .

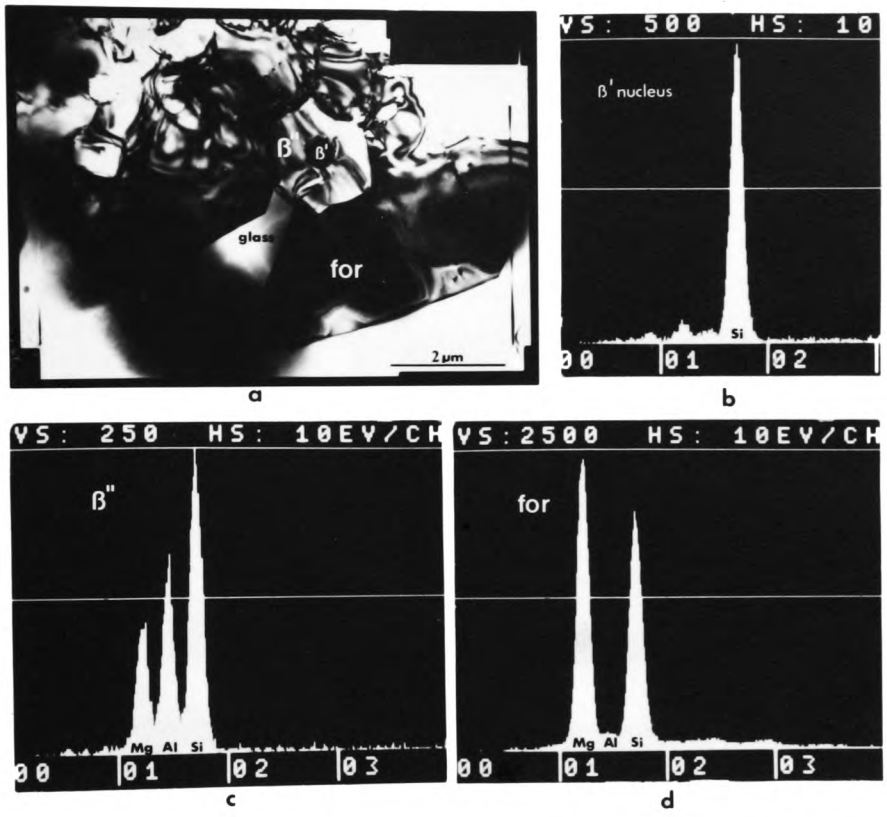

Figure 5.3

TEM micrograph of part of MgSiAlON specimen D , reacted at 1650°C, and then slow cooled.

(a) faceted forsterite crystal, ß"-magnesium sialon and ß'-sialon nucleus, together with EDAX (TEM) analysis of the (b) ß'-sialon nucleus, (d) ß"-magnesium sialon, (e) forsterite.

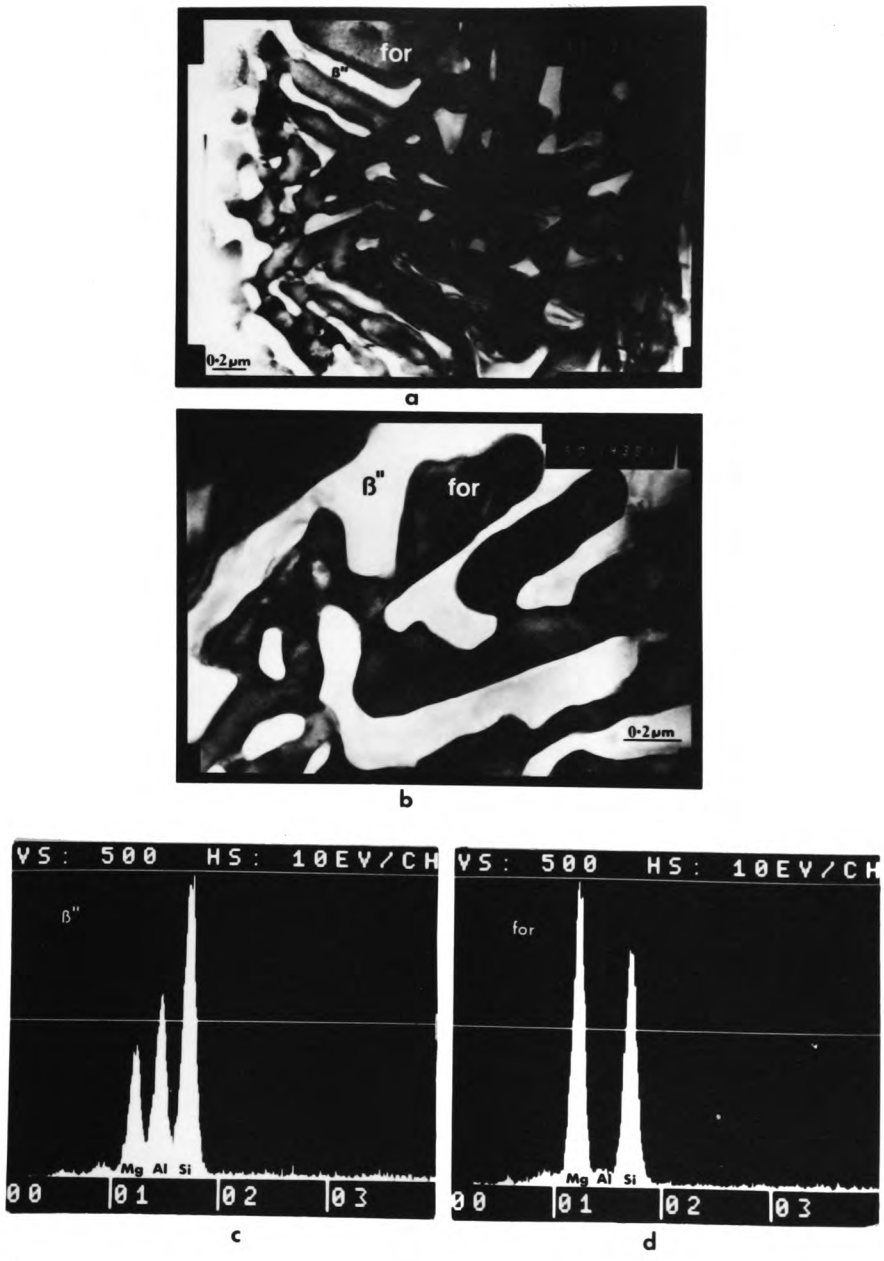

Figure 5.4

TEM micrographs (a) and (b) of part of specimen D, slow cooled after reaction at 1650°C, showing duplex structure.

(c) EDAX (TEM) analyses of the β", and (d) the forsterite phase.

NB Refer to inside cover for enlargement of 5·4(a).

5.2 COOLING VIA ISOTHERMAL STEPS.

These experiments were carried out with the eutectic liquid to provide more information on the sequence of events occuring when this liquid crystallizes into a mixture of forsterite and a low magnesium content β''.

Specimens of the eutectic liquid composition in the 3M/4X plane of the MgSiAlON system were reacted for 15 minutes at 1650°C and then, each cooled down to a temperature below the liquidus temperature, held there for 30 minutes, then quenched, as illustrated schematically here:

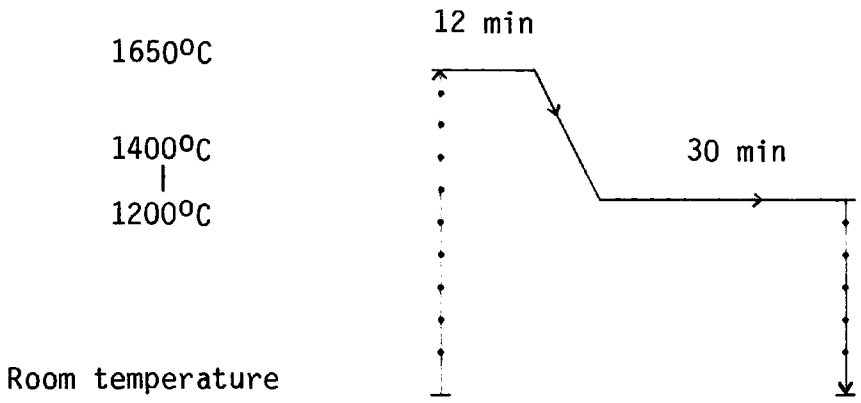

The temperature of the isothermal holding step was varied between 1400°C and 1200°C. To lower the temperature from 1650°C to this hold step, the graphite crucible containing the specimen was lowered from the 'hot zone' of the furnace alumina tube down to that part of the tube at the required temperature. The actual temperatures of the holding steps were not measured accurately, ie ±15°C ; but the steps were made at lower and lower temperatures giving a sequence of progressively larger degrees of undercooling. The crystalline phases present in four eutectic composition specimens, cooled from 1650°C via isothermal holding steps, are listed in Table 5.2.

Table 5.2

Crystalline product phase of eutectic compositions reacted at 1650°C for 15 minutes and each cooled via an isothermal holding step.

Temperature (C) of hold step	% Vol crystallinity	Crystalline phase
1400	10%	Forsterite
1375	80%	Forsterite (m) β" (m)
1325	95%	Forsterite (s) β" (wm) Q (m)
1200	95%	Forsterite (s) Q (m)

Micrographs of polished sections of the specimens listed in Table 5.2 are presented in fig 5.5 to fig 5.10. These four eutectic composition specimens each cooled via a holding step are referred to as E-1400, E-1375, E-1325 and E-1200.

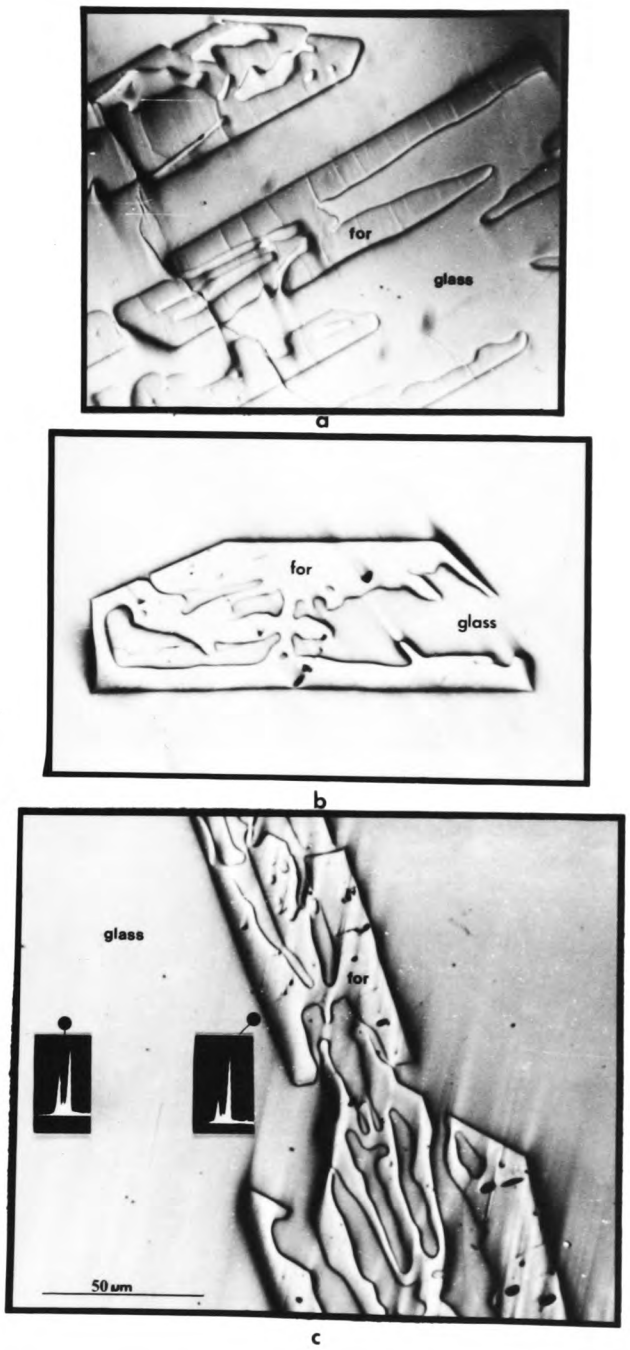

Figure 5.5

E-1400 : (a) and (b) Optical micrographs of forsterite crystals within the glass matrix.

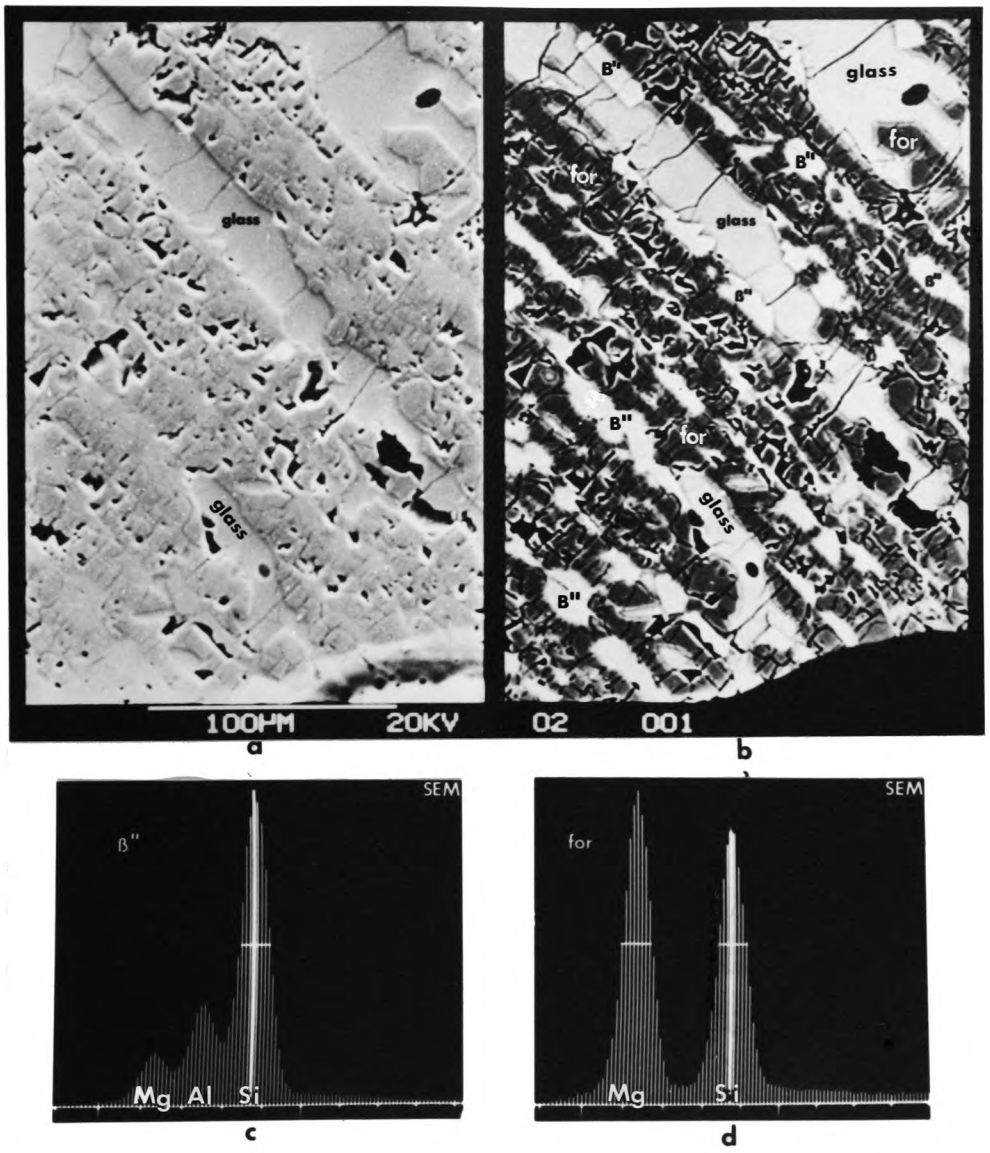

Figure 5.6

E-1375 : SEM micrographs, (a) secondary electron mode, (b) back-scattered electron mode; EDAX (SEM) analyses of (c) the β'' phase, and (d) forsterite phase.

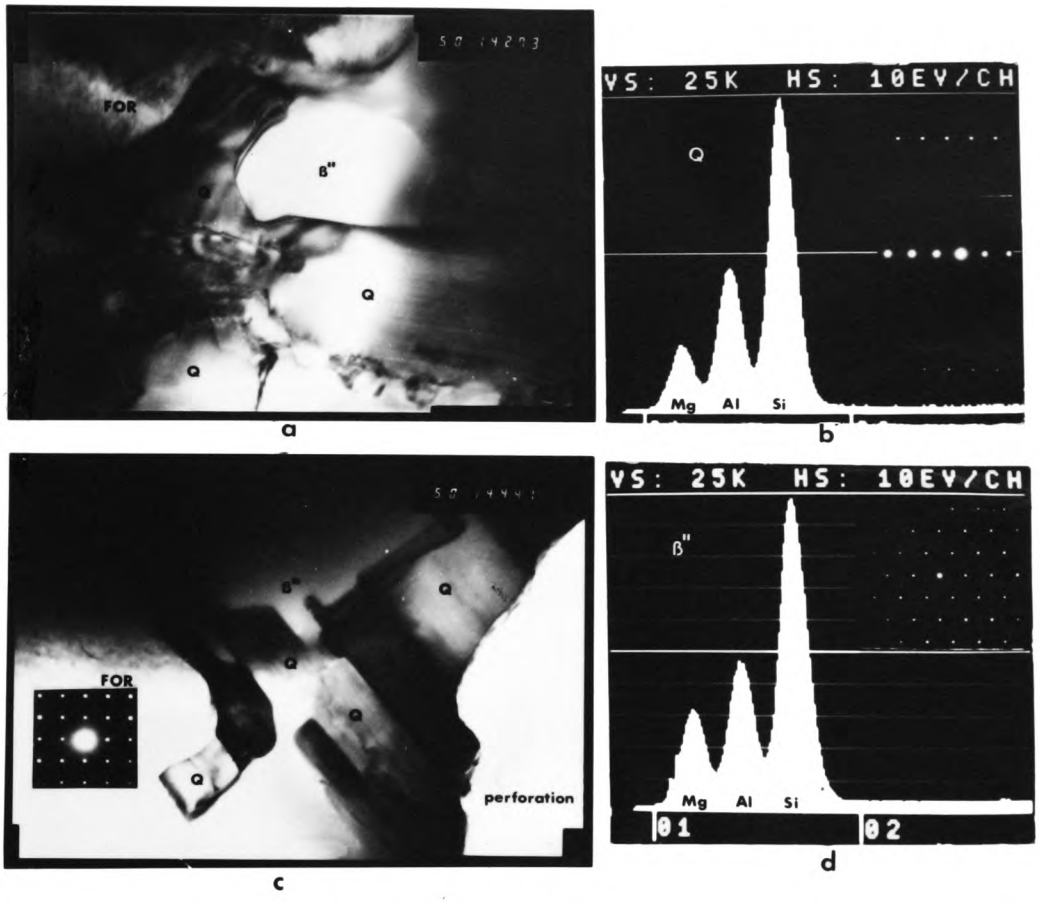

Figure 5.7

E-1325 : TEM micrographs (a) and (c) ; and EDAX (TEM) analyses of (b) Q phase and (d) ß".

Representative electron diffraction photographs of forsterite, Q-phase and ß" are included.

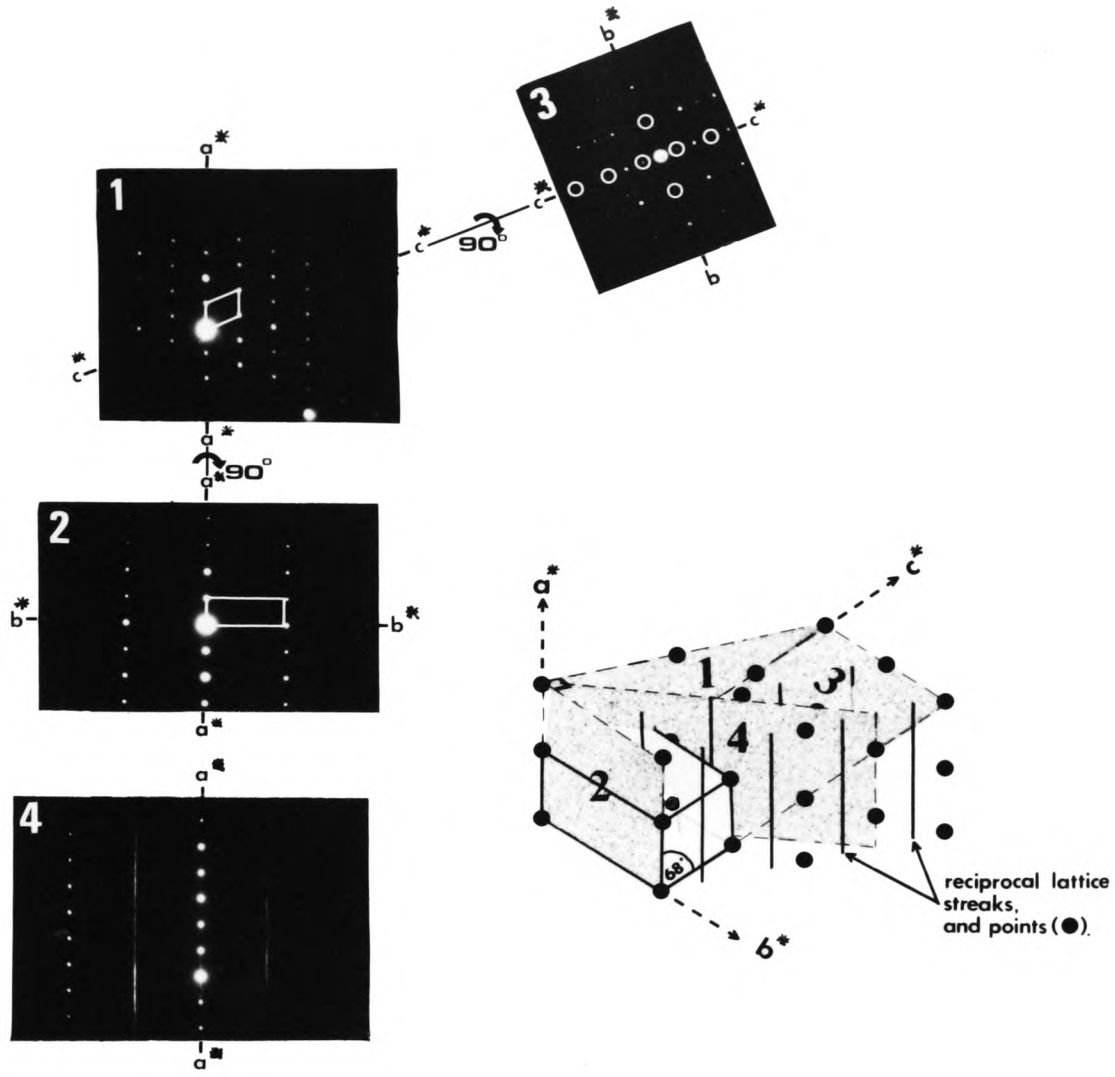

(a) (b)

Reciprocal lattice planes 1,2,3 and 4 are shown as solid opaque plane sections.

Figure 5.8

Electron diffraction photographs of Q-phase taken from specimen E-1325, and a section of the Q-phase reciprocal lattice. See text for discussion on page 146.

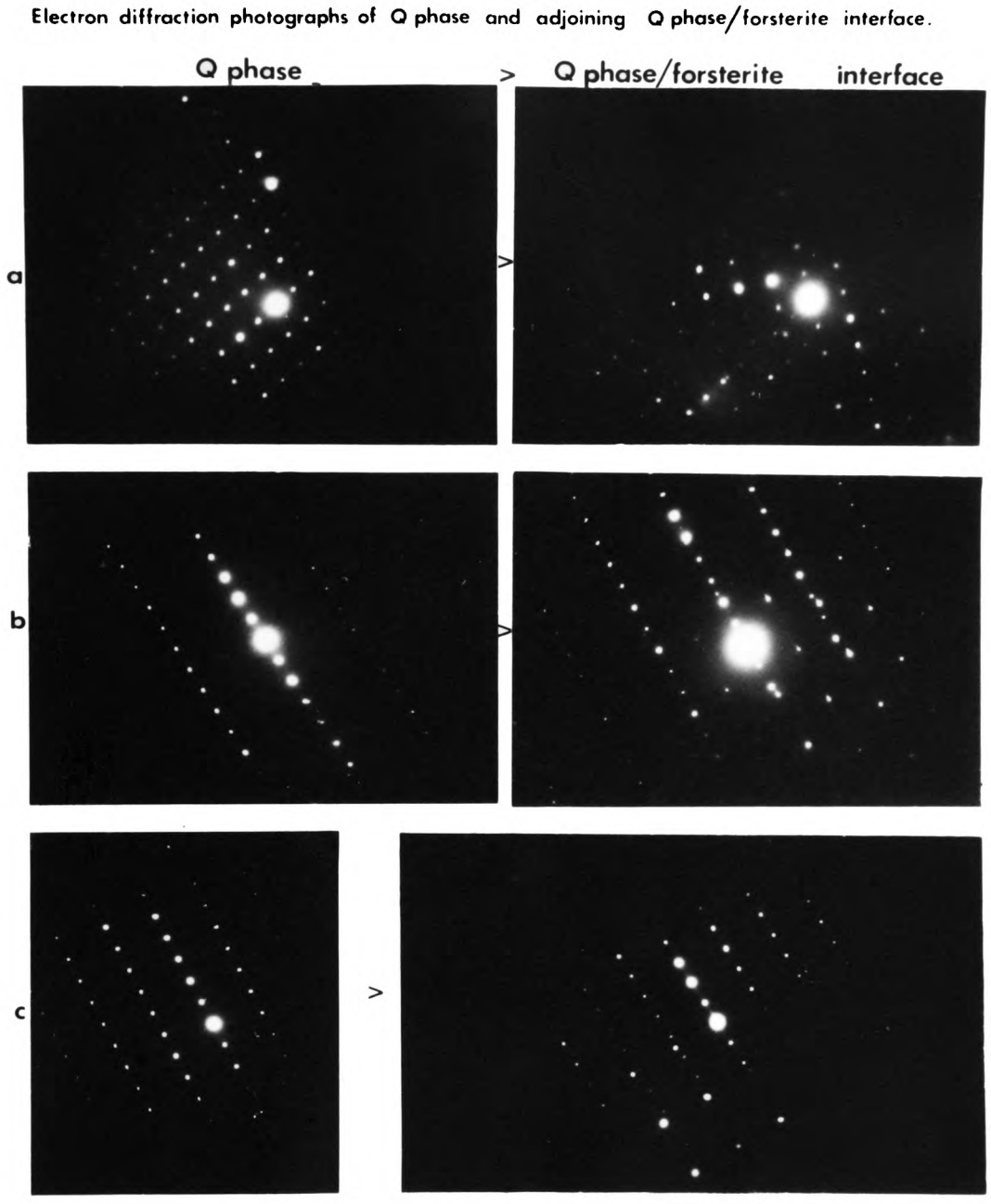

Figure 5.9

Electron diffraction photographs of forsterite/Q phase crystal interfaces in specimen E-1325.

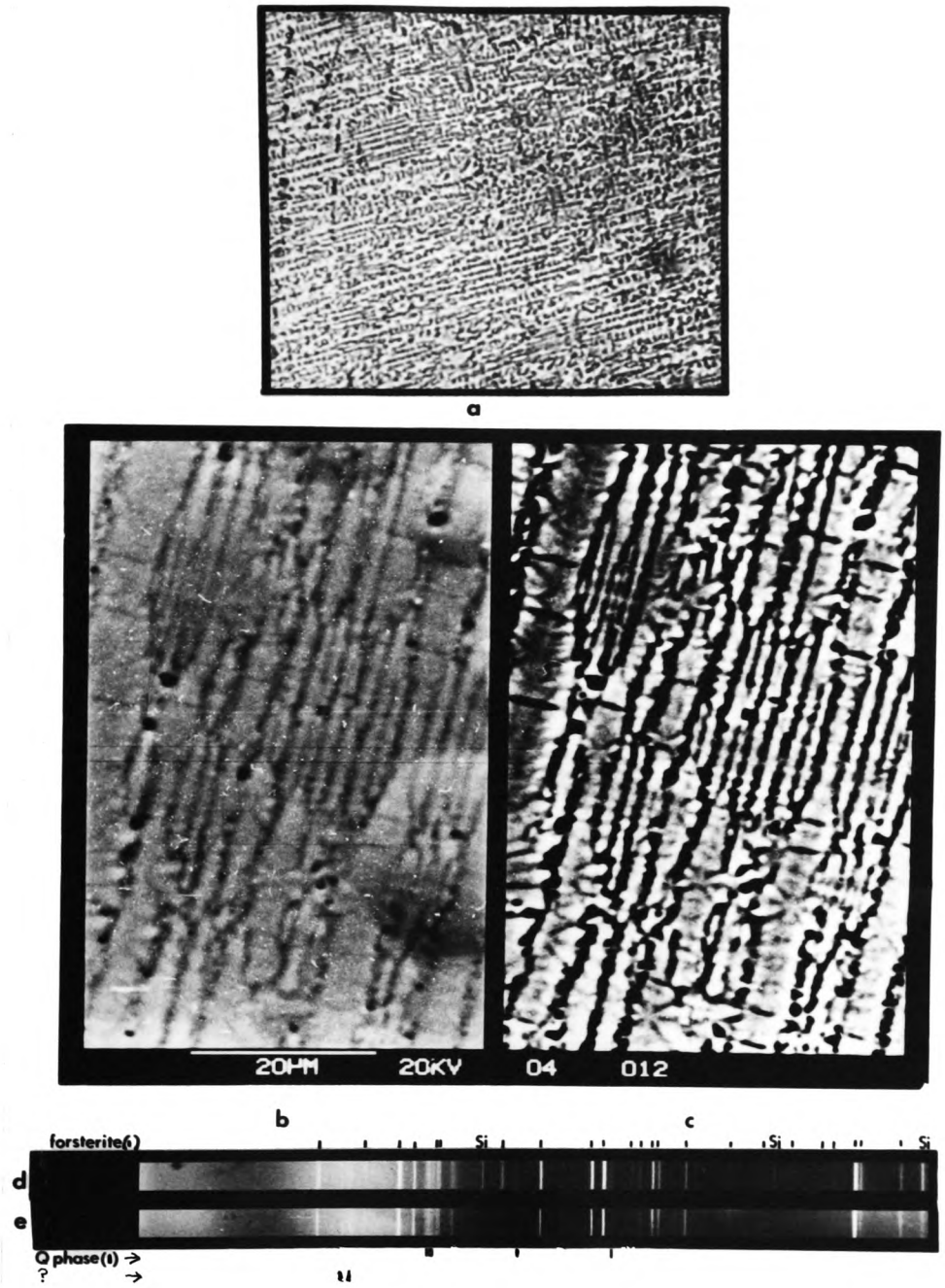

Figure 5.10

E-1200 : (a) Optical micrograph; SEM micrographs (b) secondary electron mode and (c) backscattered electron mode.

Guinier X-ray diffraction photographs of (d) E-1200 and (e) a quenched eutectic glass that has been annealed 3 hours at 1350°C.

The compositions of the phases β" and Q-phase as analyzed by EDAX are presented in Table 5.3 and fig 5.11.

Table 5.3

Compositions of phases occurring in slow cooled E and D specimens and in E-1325.

Specimen	Phase	Composition.					EDAX (TEM/SEM)
							*
E	β"	Mg	Si	Al	O	N	SEM
		1.38	3.32	1.30	3.76	4.24	
D	β"	Mg	Si	Al	O	N	TEM
		1.74	2.40	1.85	5.33	2.67	
E-1325	β"	Mg	Si	Al	O	N	TEM
		1.60	2.80	1.60	4.8	3.2	
	Q	Mg	Si	Al	(O,N)		
		1.12	3.12	1.77			

* This SEM EDAX analysis was carried out by relating the EDAX spectrum of a bulk specimen analysis to the known bulk composition and so determining empirical correction factors which were then applied to the EDAX spectra of the β".

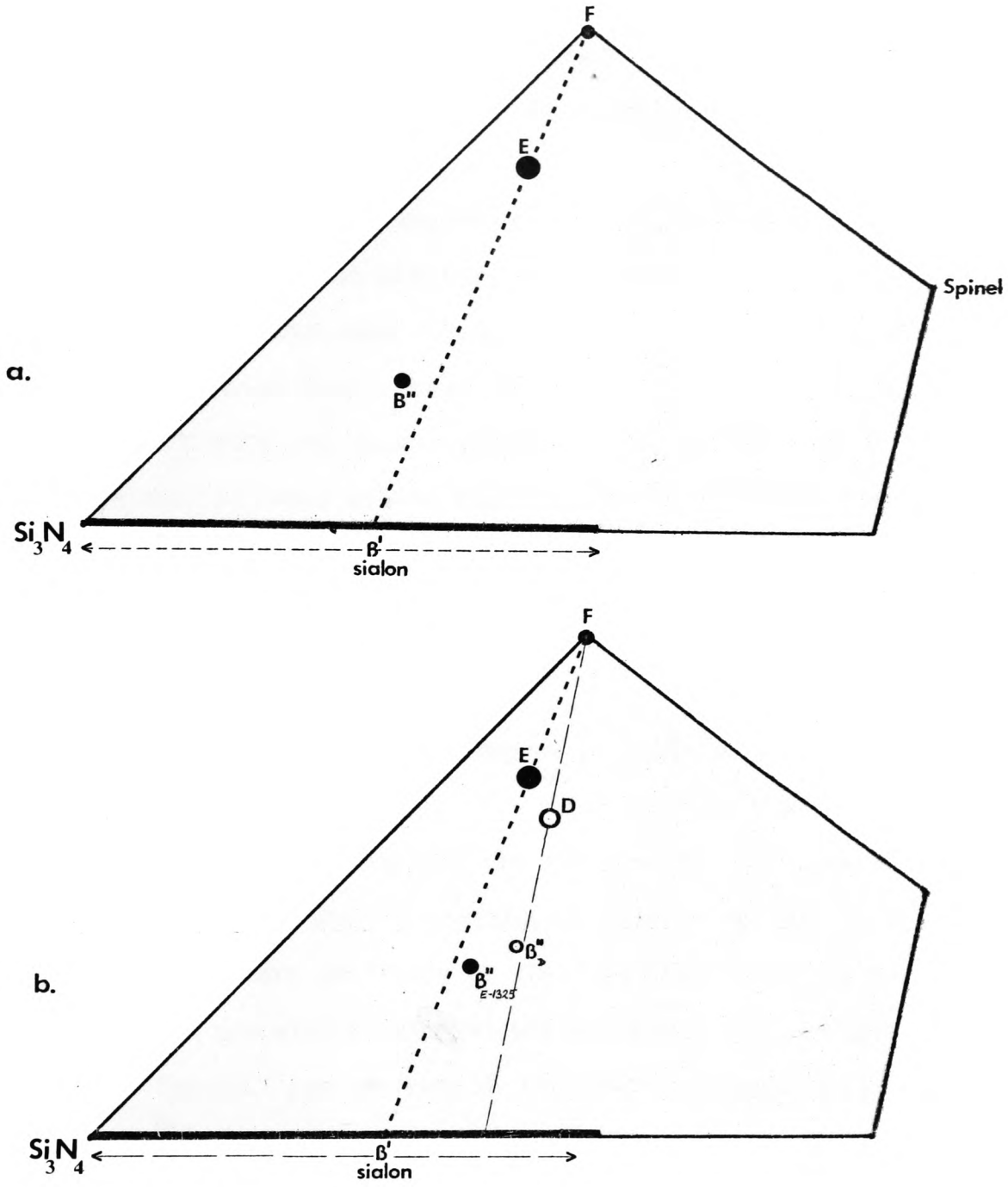

Figure 5.11

The 3M/4X MgSiAlON composition plane;

(a) β" composition from the duplex structure of the slow cooled eutectic specimen.

(b) β" of the slow cooled D specimen and β" composition of specimen E-1325.

The main microstructural features of these eutectic composition liquids cooled via various holding steps are:

E-1400 This specimen, cooled via a holding step which is just below the liquidus temperature of 1420°C, consists of mainly clear glass and large forsterite crystals making up approximately 5-15 % vol. These forsterite crystals are long finger-like crystals with the outer interfaces flat and pointed at the ends, but with open volumes within the crystals which have smooth curved interfaces. This anomalous morphology appears partly faceted in character and partly cellular.

E-1375 With the greater degree of supercooling at 1375°C, this specimen consists of forsterite and low magnesium content β" with approximately 15-25% vol of residual glass. The morphology of the forsterite crystals is similar to that in E-1400 but now β" crystals have nucleated at the forsterite surfaces growing out into the glass and also growing within the gaps in the large forsterite crystals. Careful comparison of the secondary and back-scattered electron mode SEM micrographs on page 129 shows the β" phase as the lightest tone phase in fig 5.6 (b). The HF etch only distinguishes between glass and crystalline material in micrograph (a) taken in the secondary electron mode.

The EDAX (SEM) analysis of the β" in this specimen is similar to that in the continuously cooled eutectic composition specimen of fig 5.2 (h) on page 121.

E-1325 This specimen is almost completely crystalline, 10% residual glass, and appears as a two phase assemblage in reflected light; however, the X-ray diffraction photograph shows that together with forsterite there are now two other phases, B" and Q-phase.

The three crystalline phases can be easily distinguished in the TEM because the forsterite shows characteristic radiation damage after a few minutes in the electron beam giving a mottled texture, the Q-phase has a faulted structure which shows as fine parallel streaks, while the B" crystals appear clear. These features are clearly illustrated in fig 5.7 page 130, together with a characteristic electron diffraction pattern from each of the three crystalline phases.

EDAX (TEM) analysis of the B" and Q-phase show their metal atom compositions to be very similar, with the B" having a slighly higher Mg content than the Q-phase.

Electron diffraction photographs taken on forsterite/Q-phase interfaces show that there is a definite crystallographic relation between the forsterite and Q-phase crystals. In fig 5.9 page 132, each diffraction pattern in the left column is taken from a Q-phase crystal alone, while the right hand diffraction pattern of each pair is taken over an area including a neighbouring forsterite crystal. The clear lining up of rows of diffraction spots in the Q-phase patterns with rows of spots in the forsterite patterns indicates that the Q-phase must have nucleated on the forsterite.

E-1200 This specimen gave a two phase crystalline mixture of forsterite and Q-phase with a very fine dendritic morphology. This very fine dendritic morphology shows up clearly in the SEM backscattered micrograph of fig 5.10 page 133, but the exact nature of the two phases and the relationship between them is not apparent and it would need further TEM work to resolve this.

In fig 5.10 the X-ray diffraction photograph (d) of E-1200, and of (e) a quenched eutectic glass after annealing at 1350°C are compared. Both show the same two phases, forsterite and Q-phase, with no sign of any β'-sialon phase which would be the expected stable secondary product to occur with forsterite with the eutectic glass having been annealed at a high subsolidus temperature.

The interplanar d-spacings (Å) for the observed Q-phase diffraction lines are as follows; 3.61, 3.58, 3.53, 2.91, 2.43 Å.
(weak d-spacings of 4.68 and 4.63 Å are also observed, but not identified as necessarily arising from Q-phase)

5.3 SUMMARY AND CONCLUSIONS.

5.3.1 Forsterite / B" duplex structure.

Both the MgSiAlON liquids of composition D and E, when cooled slowly, show that MgSiAlON liquids in the 3M/4X plane can crystallize in a duplex morphology involving the coupled growth of forsterite and a low magnesium content B"-magnesium sialon.

Growth is said to be coupled when the duplex solid is arranged at the growth front in such a way as to maintain a near steady state diffusion process in the liquid, with the two phases growing edgewise into the melt ideally as parallel lamellae, as schematically illustrated in fig 5.12. This regular lamellae structure is illustrated

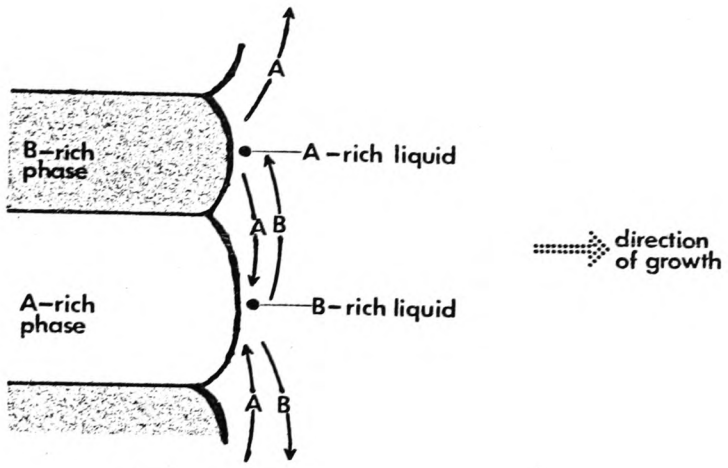

Figure 5.12

Growth, mechanism and diffusion paths for a lamellar eutectic AB; after Chalmers 'Principles of Solidification' (75).

most clearly for the eutectic specimen in the micrograph of fig 5.2 (f) on page 121. During coupled growth of a eutectic AB, the A-rich phase rejects B atoms and the B-rich phase rejects A atoms. In the case of Mg_2SiO_4/β"-MgSiAlON coupled growth, the growing forsterite phase would be rejecting Al and N atoms while the growing β"-magnesium sialon phase would be rejecting excess Mg and O atoms, with the proportion of Si approximately the same in each phase.

This structure can occur when a material of eutectic composition is solidifying under near equilibrium conditions. It also can occur with 'off-eutectic' compositions at subeutectic temperatures when the growth velocity of the coupled structure is higher than the growth velocity of the primary phases individually : this means that there can be a composition range, termed the 'coupled zone', within which the two phases are able to grow cooperatively by the normal short range diffusion mechanism, at a rate exceeding that of primary phases separately.

Now the compositions of the two B" phases occuring in the duplex structure of the E and D specimens are different. This is shown by comparing their hexagonal 'a' unit cell dimensions which are repectively 7.728 $\mathring{A}$ and 7.754 $\mathring{A}$ as shown in Table 5.1 on page 118. This composition difference is also shown in their respective EDAX spectra in figs 5.2 (h) and 5.3 (c) (although these are not strictly comparable because one is an SEM spectra and one a TEM). These two different β" compositions both found in coupled duplex structure with forsterite show the existence of a coupled zone in this MgSiAlON 3M/4X composition plane.

That is, off-eutectic liquid compositions to the left and to the right of the eutectic E composition may crystallize by a coupled

mechanism, giving coupled forsterite/β" growth where the low Mg content β" phase composition can vary considerably. As an example of this, taking a liquid composition to the right of the eutectic composition E , fig 5.11 on page 135, on cooling instead of initially primary spinel precipitating and bringing the liquid composition back to E, followed by coupled forsterite/β" growth : the liquid may solidify by coupled forsterite/β" growth with the β" of relatively high Al content.

Variation in the interlamellar spacing in a eutectic specimen can arise from variation in the rate of solidification. As the rate of solidification increases the time available for diffusion at the interface decreases resulting in a smaller interlamellar spacing. Under conditions used in this work , with a small globular liquid specimen at temperature being continuously cooled as it is lowered down the furnace, there are multiple growth fronts growing away from the long forsterite crystals with no control over the growth rate. Consequently the duplex structure is irregular in spacing and direction. Normally the controlled directional solidification of a eutectic material involves getting a single plane growth front to move through the liquid at a constant rate and with a controlled temperature gradient through the specimen (77).

Neither the D or E specimens consist completely of duplex structure. D contains large faceted forsterite crystals and β"-magnesium sialon crystals which have nucleated on and grown around some small β'-sialon crystals present in this non-eutectic composition. The eutectic E specimen might be expected to give a more regular and completely duplex structure but there are long macro-forsterite crystals dispersed

through the duplex structure. The anomalous morphology of these crystals is not what one would expect of primary forsterite crystals, that would precipitate as solid faceted crystals if the liquid's composition was off-eutectic towards the forsterite corner of the phase diagram.

The series of cooling experiments done with holding steps at higher and higher degrees of undercooling provide a possible explanation for the presence of these anomalous macro-forsterite crystals. Where the MgSiAlON eutectic liquid is held at a very small degree of undercooling, specimen E-1400, and then quenched, the resultant glass contains large forsterite crystals with faceted outer surfaces, but within, having smooth curved volumes of glass (see fig 5.5 page 128). This 'internal' forsterite morphology has itself a duplex appearance, most clearly seen in fig 5.5 (c), but without any second crystalline phase present.

It appears that at this temperature the diffusion of atoms is low enough to cause diffusion controlled cellular growth on the faster growing forsterite crystal faces. However on the slow growing low energy crystal faces the low diffusion rates are not a limiting factor and faceted growth is still occuring. Hence polished sections through these forsterite crystals show this dual faceted/cellular growth.

However when the eutectic specimen is held at a larger degree of undercooling (E-1375), a second crystalline phase β" is now able to nucleate at the surface of the forsterite crystals, both on the outside and on the 'internal' forsterite/glass surfaces.

This means that under the experimental conditions employed it is not possible to produce a completely regular duplex structure. This is

because, on slow cooling the specimen, the β" appears unable to nucleate at the low degrees of undercooling in the initial stages of solidification. The initial growth of just forsterite crystals results in the adjacent liquid being very much depleted in Mg with a composition close to that of the β" that eventually nucleates and grows. The β" eventually nucleates at the forsterite surface and grows into the liquid forcing the liquid composition back towards the eutectic composition and then the duplex growth takes over.

For the eutectic composition specimen to completely crystallize as a two phase forsterite and β"-magnesium sialon mixture, then the β" composition must lie somewhere in between the eutectic composition and β'-sialon (ss), along a straight line drawn on the phase diagram from forsterite (F) through the eutectic (E) and along to β'-sialon (β'), as illustrated by the dashed line in 5.11 (a) page 135. The question arises;

At what level of magnesium substitution does the β"-magnesium sialon form, when growing by this coupled mechanism with forsterite? ...that is, how far along the line E-β' does the β"-magnesium sialon composition lie?

Now we know that ;

(i) At high temperatures, that is 1700°C and above, Mg solubility in β'-sialon is approximately zero, as referred to in Chapter One by the work of Gauckler and Lewis (page 11).

(ii) At medium temperatures, that is 1300-1400°C, β"-magnesium sialon crystals with relatively low levels of magnesium substitution are able to grow. eg. as shown by the EDAX analyses of β" crystals in

specimens E-1375 and E-1325.

(iii) At low temperatures, that is 900-1100°C, anM6 β"-magnesium sialon grows from the glassy state with a high level of Mg substitution (its composition being close to the eutectic composition). However this β" is unstable over 1120°C.

(iv) The β"-magnesium sialon in the eutectic specimen duplex structure has grown at a specific composition, as shown by its reasonably sharp diffraction lines in fig 5.1 (b) on page 120.

From these results it seems that for a particular temperature there is a maximum level of magnesium substitution tolerable in the β"-magnesium sialon structure, and that this level decreases with increasing temperature. Huseby found a similar trend with Be substitution in β'-Si_3N_4 with the amount of Be tolerable in the β' lattice decreasing with increasing temperature (page 12).

The composition along the E-β' line that the β"-magnesium sialon phase grows at in the coupled duplex structure should then be determined by two factors :

(a)The temperature, which sets an upper limit on magnesium substitution.

(b) The diffusion growth mechanism, which will operate more easily the closer the compositions of the two duplex phases are to each other.

Hence the β"-magnesium sialon should grow at a composition along the line E-β' as close to E as can be tolerated by the β" lattice in the temperature range prevailing.

The three β"-magnesium sialon phases formed in specimens E, D and E-

1325 all have compositions approximately half way between the eutectic composition and β'-sialon solid solution as plotted on the 3M/4X MgSiAlON phase diagrams of fig 5.11 on page 135.

5.3.2. Q Phase.

(A) Formation : The continuously slow cooled eutectic E specimen and specimen E-1375 contain two crystalline phases, forsterite and a low Mg content β". However with specimens E-1325 and E-1200, solidified at progressively larger degrees of undercooling, the low Mg content β"-magnesium sialon phase is progressively replaced as the second crystalline phase by Q-phase. E-1200 consists of just forsterite plus Q-phase; the high degree of undercooling and consequent high viscosity has led to a very fine dendritic microstructure.

The eutectic composition specimen EQ-1350, solidified by the different route of quenching to a clear glass and then annealing at a temperature of 1350°C, just below the liquidus, also crystallizes to a two phase mixture of forsterite and Q-phase as shown by the two relevant X-ray diffraction photographs of fig 5.10 (d) and (e) page 133.

This annealing of a glass at a high subsolidus temperature usually produces the stable crystalline phases for a system. Now one might expect that the equilibrium crystalline phase product for the eutectic composition in the 3M/4X composition plane would be a 73% forsterite plus 27% β'-sialon mixture (ie. equiv %, using the Lever rule along the forsterite - eutectic - β'sialon composition line). Howvever there is no sign of any β'-sialon crystallizing from this glass, instead the second phase is Q-phase.

In E-1325 the crystallographic relationship between Q phase and

forsterite shows that the Q phase has nucleated at the forsterite interface, and also the morphology of the Q phase crystals in fig 5.7 (c) page 130 suggests that Q-phase is growing into and may be consuming the β" which had formed at an earlier stage.

(B) Composition : The EDAX (TEM) analysis of the Q-phase formed in E-1325 is very similar to the analysis of the β"-magnesium sialon phase found in the same specimen, fig 5.7 (d). These two compositions are plotted on the 3M/4X MgSiAlON composition diagram in fig 5.11 (b). In plotting the Q-phase composition it is assumed that its composition does lie in the 3M/4X plane, because, the E-1200 specimen appears to completely crystallize into just two phases, and we know that both the forsterite and the overall compositions both lie on the 3M/4X plane.

(C) Structure: A selection of Q-phase electron diffraction photographs is presented in fig 5.8 (a) page 131. Photographs '1', '2' and '3' show the most rational patterns obtainable, each of these three patterns being related by 90° rotations about the axes shown. In rotating from patterns '1' to '2' there is a series of patterns containing reciprocal lattice streaks indicative of stacking faults parallel to the basal plane ; one example of these is pattern '4', which is the same diffraction pattern previously observed in the fully transformed M6 B" product in fig 4.14 (b) page 106.

Patterns '1' and '2' of fig 5.8 page 131 suggest a monoclinic unit cell for Q-phase. However this is not satisfactorily resolved as yet, because the monoclinic reciprocal unit cell outlined in fig 5.8 (b) has systematic absences along the c^* axis as well as the b^* axis, and, systematic absences may only exist along one axis of a monoclinic

reciprocal lattice unit cell. The ringed diffraction spots in pattern '3' show the diffraction spots that are filled in by double diffraction where these systematic absences occur along the c^* and b^* axes (ie. Compare the c^* axis row of spots in patterns '1' and '3', and the b^* axis row of spots in '2' and '3' to observe this).

5.3.3 Conclusion.

If the low magnesium content β"-magnesium sialon phases and Q-phase were stable phases for the MgSiAlON system then it should be possible to prepare them from suitable mixtures of Si_3N_4, SiO_2, Al_2O_3, MgO and AlN.

Specimens made up with compositions in the region of the B"-magnesium sialons and Q-phase found in specimens E, D, and E-1325 (fig 5.11 page 135) have been sintered at 1650°C, and no evidence was found for these compositions forming a Q-phase or a β"-magnesium sialon product. Instead these compositions all sinter to give β'-sialon and glass (which partly crystallizes on cooling to give metastable β"-magnesium sialon) and also possibly some 15R and spinel. For example see the results for the reactions of compositions J4 to Q4 in Table 3.2 on page 62.

Attempts to react a specimen made up at the β" composition found in the slow cooled specimen D at subsolidus temperatures (below 1420°C) for longer time periods provided no evidence for the formation of a β" product, because, with such stable compounds and with only solid-state reaction possible the reaction rates are too slow for significant reaction to occur.

Therefore there is no evidence for the low Mg content β" and the Q-

phase actually being stable equilibrium phases in the MgSiAlON system. Both appear to be metastable crystalline phases formed -

(a) via a MgSiAlON liquid stage as an intermediate step,

(b) together with forsterite,

(c) with the relative amounts of the low Mg content β" and Q phase dependent on the level of undercooling and the cooling rate.

By cooling at the slow rate used in this work it is possible to crystallize the eutectic liquid as a forsterite/β" duplex mixture. This forms between the liquidus (1420°C) and 1350°C : the time spent in cooling from 1350°C down through 1200°C is not sufficient for the conversion of the β" to Q phase.

However if the eutectic liquid is cooled via a holding step in the 1350-1200 °C region, then β" and Q-phase form together with forsterite (Q-phase nucleating on the forsterite). It is possible that β" forms initially and then transforms partially into Q-phase (eg. E-1325).

If the holding step is at a sufficiently low temperature of say 1200°C, as was for specimen E-1200, then it is likely that the Q phase forms directly with forsterite, without any intermediate β" formation.

. . .

CHAPTER SIX.

DIFFRACTION STUDIES OF β"-MAGNESIUM SIALON.

6.1 X-RAY DIFFRACTION.

The compositions of β" crystals plotted on the 3M/4X MgSiAlON plane on page 95 indicate a likely ordering of Si relative to (Mg,Al). That is, the β" compositions lie close to the Mg_2SiO_4- $Al_2SiO_2N_2$ line of the 3M/4X composition plane. Along this line the (Mg+Al):Si metal atom ratio is 2:1, similar to the 2:1 Be:Si ratio in the mineral phenacite. The existence of these apparently narrow composition limits strongly indicates some form of ordering of the different atom types within the B" structure. The presence of such ordering, with the Si atoms existing on particular metal atom sites and the Mg and Al on other metal atom sites, might show up on the X-ray diffraction photographs as additional weak reflections.

However no such additional reflections are apparent on the Guinier X-ray diffraction photographs of the M6 β" in fig 4.5 (d) on page 83. All the observed β" reflections index on the same hexagonal unit cell as β-Si_3N_4.

. . .

6.2 ELECTRON DIFFRACTION.

6.2.1 Preliminary observations.

Careful observation of long exposure electron diffraction photographs of the M6 β", annealed at 910°C, does in fact reveal additional weak diffuse streaked spots along with the normal hexagonal B' pattern of spots. These diffuse spots, indicative of partial ordering, are too weak to be observable with the naked eye on the TEM screen.

However β" crystals grown at 980°C show a very marked sharpening of these additional spots, as shown in the two (110) electron diffraction patterns in fig 6.1, of β" crystals grown at (a) 910°C and at (b) 980 °C. Electron diffraction patterns of the untransformed parts of β" crystals that have been partially transformed at 1200°C still have these same discrete additional spots, showing that the ordered crystal structure can exist at temperatures just prior to transformation.

These additional reflections reveal a form of long range ordering which results in a much larger hexagonal cell ($a_{\beta"}$, $c_{\beta"}$) than that originally used to index the X-ray powder diffraction patterns (a_β, c_β). The two cells are related by ;

$$a_{\beta"} = \sqrt{3}.a_\beta \qquad c_{\beta"} = 3\,c_\beta \qquad \ldots (15)$$

In phenacite, Be_2SiO_4, the beryllium atoms are ordered relative to the silicon atoms in a 2:1 ratio, and being rhombohedral, phenacite can equally well be indexed on a similar large hexagonal cell. However a more useful comparison is with willemite, Zn_2SiO_4, which is isostructural with phenacite and which has hexagonal cell dimensions (large hexagonal cell) very similar to those of the M6 β" (Table 6.1).

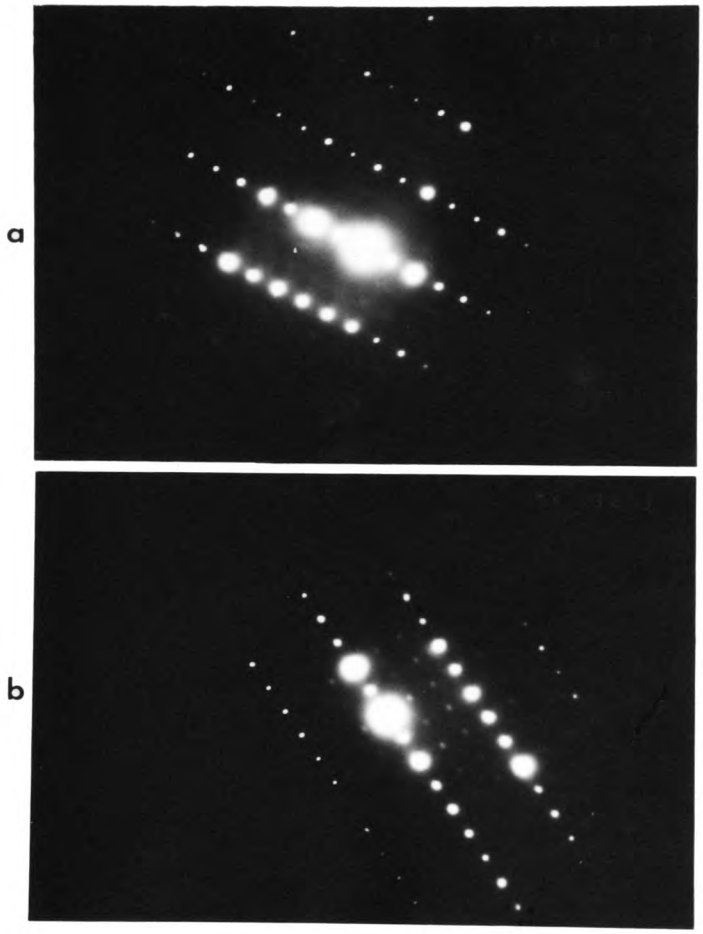

Figure 6.1

Electron diffraction patterns (110) of β"-MgSiAlON crystals.

(a) grown at 910°C.

(b) grown at 980°C.

Table 6.1

Large hexagonal unit cell dimensions of β" (M6), willemite and phenacite.

material	a	c
β"-magnesium sialon (M6)	13.64 Å	9.315 Å
Zn_2SiO_4	13.94 Å	9.309 Å
Be_2SiO_4	12.47 Å	8.252 Å

This similarity in cell dimensions means that the electron diffraction patterns of β" and willemite are easily comparable, being of almost the same scale. Therefore electron diffraction patterns of willemite were obtained in order to provide a direct comparison with those of B" (for the same orientations) in order to ascertain whether B" (M6) is also isostructural with phenacite.

* The term 'superlattice' is used from now on to describe the enlarged unit cell caused by the metal atom ordering, and the additional diffraction spots are termed 'superlattice' spots. The term superlattice can only be strictly applied where the disordered crystalline state also occurs and so the term is used in parentheses while taking into account the following two notes.

Note (1) At the M6 β'-MgSiAlON composition, completely disordered crystals have not been found (ie. additional diffraction spots have always been observed even though at times these are very weak and

diffuse) but at the low magnesium content β" compositions found in Chapter Five (fig 5.11 page 135) there are no observable additional spots and consequently no cation ordering at these β" compositions.

Note (2) In Zn_2SiO_4, there is no known disordered hexagonal form of Zn_2SiO_4 (although metastable forms of Zn_2SiO_4 do exist with triclinic, tetragonal, orthorhombic, and cubic structures (80)).

. . .

6.2.2 The willemite structure and its reciprocal lattice.

Willemite, Zn_2SiO_4 has the phenacite (78) structure (space group $R\bar{3}$), being isostructural with the mineral phenacite (Be_2SiO_4) (78,79).

The crystal classes 3, $\bar{3}$, 32, 3m and $\bar{3}2/m$ can have either a primitive rhombohedral lattice or a non-primitive hexagonal lattice. Even when the lattice is rhombohedral, it is customary to continue to refer the crystal to the hexagonal cell because the orthogonality of the c axis to the plane of the a_1 and a_2 axes gives rise to a simpler geometry. When this is done, the hexagonal cell is no longer primitive but triple as shown in fig 6.2 (a). A criterion is then needed to decide whether such a crystal really belongs to the hexagonal system or is actually rhombohedral. If the conditions for reflection are :

(ie. three lattice points per unit cell)

$$(-h + k + l) = 3n \qquad \ldots (16)$$

then the crystal is rhombohedral.

For a rhombohedral crystal indexed as a non-primitive hexagonal lattice, the forbidden reflections not meeting this criterion, ie. with indices (-h+k+l) not equal to 3n, cannot be filled in by double diffraction. So the recognition of such a rhombohedral lattice cannot be confused by multiple diffraction. This is because reciprocal lattice vectors which already satisfy the above equation can only add to other vectors which also satisfy the same condition. Therefore multiple diffraction will modify the intensities of the reflections satisfying equation (16) but will not give rise to forbidden reflections, such as those obtained in the forsterite pattern of fig 2.5 on page 41.

In willemite the zinc atoms are ordered on particular metal atom sites and the silicon atoms on others. Each column of metal atoms

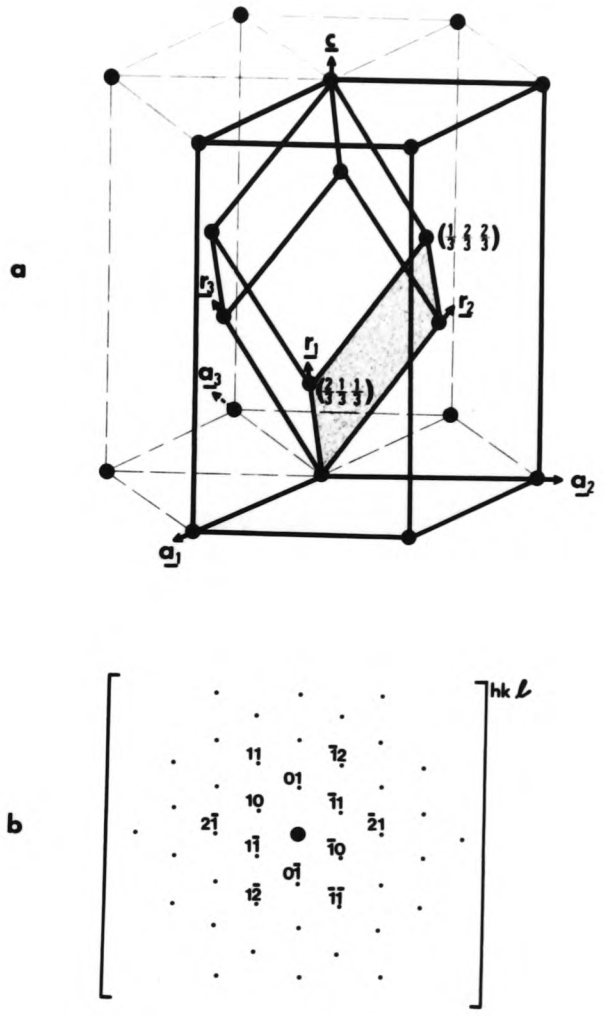

Figure 6.2

(a) The rhombohedral (primitive) and the hexagonal (non-primitive) unit cells in a rhombohderal lattice (83).

(b) A projection down c^* axis of the hexagonal reciprocal lattice.

parallel with the screw triad axes is arranged in the sequence **Zn Zn Si Zn Zn Si,** corresponding to the arrangement of Be and Si in phenacite (78,79). This arrangement means that the diffraction spots in layers,

... hk1, hk2, hk4, hk5, hk7, hk8 ...

receive structure factor contributions only as a result of differences in the scattering power between **Zn and Si,** the oxygen atoms making no contribution to the structure factor for these particular reflections (ie. those with l not a multiple of 3).

The diffraction spots in hkl layers with l=3n are strong, while spots in layers with l≠3n are of very low intensity. In the following figures illustrating sections of reciprocal lattices the strong spots are represented with large dots and the low intensity spots with small dots. The hexagonal reciprocal lattice illustrated in fig 6.2 (a) consists of a series of layers one above the other with l= ...$\bar{3}$,$\bar{2}$,$\bar{1}$,0,1,2,3... and each layer separated by a distance c^{-1}.

In fig 6.3, the hk0, hk1, hk2 and hk3 reciprocal lattice layers of willemite ($R\bar{3}$, large hexagonal lattice) are illustrated, with only the reciprocal lattice points obeying the rhombohedral criterion of equation (16) represented. All points not obeying this criterion have zero structure factor.

In fig 6.4, these same four reciprocal lattice layers are illustrated in a clinographic projection. This three dimensional representation is used to help visualize plane sections through the willemite reciprocal lattice and hence to explain the electron diffraction photographs obtained.

In the following illustrations showing specific plane sections

through the willemite reciprocal lattice, reciprocal lattice points in a particular plane section are white, while, those points out of this plane are only just visible as dark spots against the black background. Thus the pattern of white dots is a three dimensional projection of part of the diffraction pattern for that particular orientation.
NB. The clinographic projection foreshortens the direction normal to the page.

The condition for a reciprocal lattice point hkl to lie in the (uvw) reciprocal plane (containing the origin 000) is given by (81):

$$hu + kv + lw = 0 \qquad \ldots (17)$$

This geometrical relationship is used to specify the crystal orientation for each particular indexed diffraction pattern.

In the following work ;

(1) reciprocal lattice points are referred to by their indices as hkl ; eg. 021 and 321.

(2) reciprocal lattice planes, and the electron diffraction photographs that they represent, are referred to by their indices as (uvw) ; eg. (122) and (110).

. . .

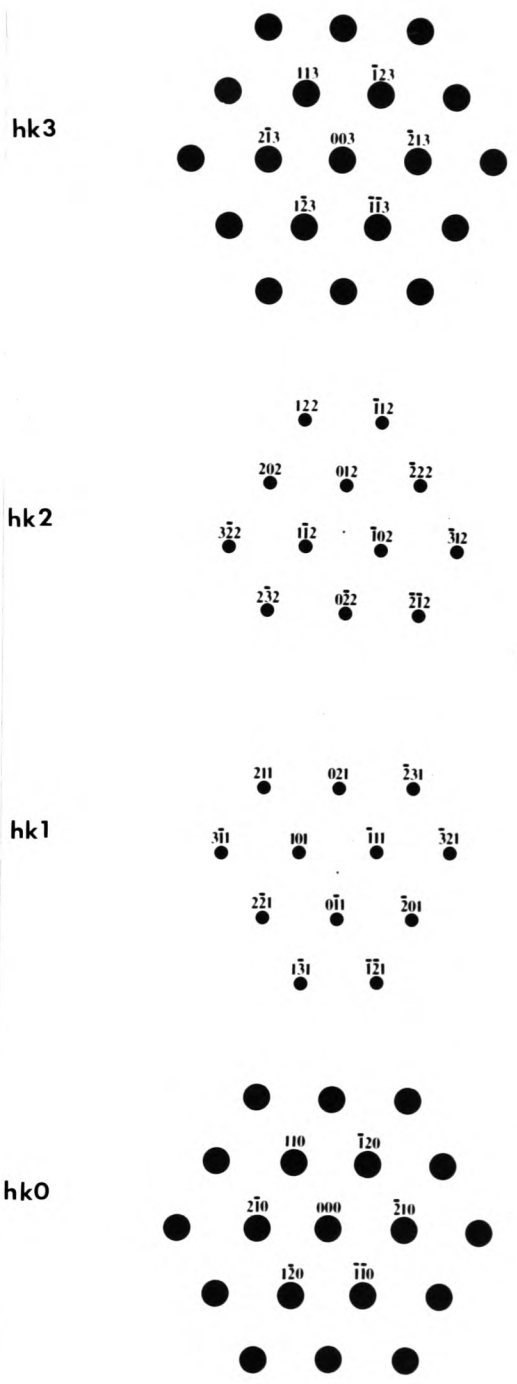

Figure 6.3

Sections of the hk0, hk1, hk2, and hk3 layers of the $R\bar{3}$ reciprocal lattice.

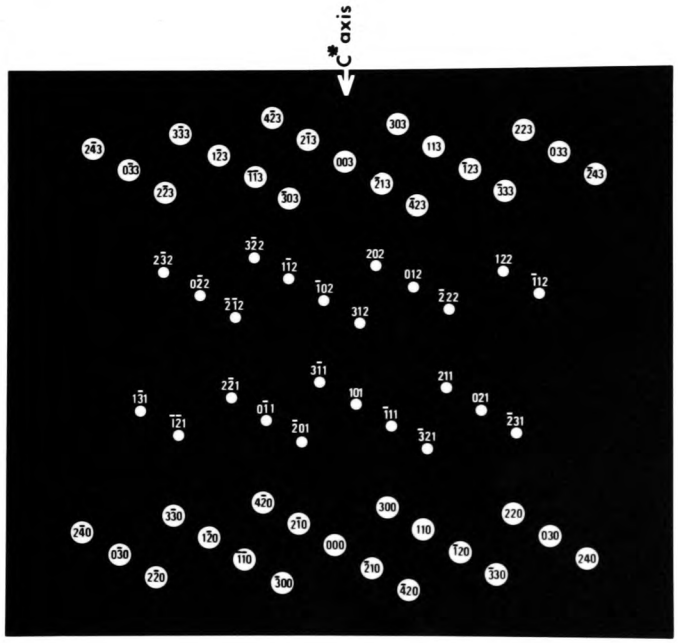

Figure 6.4

A clinographic projection of part of the $R\bar{3}$ reciprocal lattice, showing sections of the hk0, hk1, hk2 and hk3 layers.

6.2.3 Electron diffraction photographs of β" (M6) and willemite.

In the figures of this section, for each particular orientation a schematic projection of the particular reciprocal lattice plane is presented, together with the relevant willemite and B" electron diffraction photographs. Where the willemite diffraction pattern was not obtained a schematic representation of it is given.

ORIENTATION (001) Fig 6.5 The fundamental basal pattern (001) shows the characteristic regular hexagonal pattern of spots for both willemite and β".

Starting from this (001) orientation, rotation about a suitable axis gives a set of systematic diffraction patterns, as a series of zones appear with their zone axes becoming parallel to the electron beam. There are two convenient axes to rotate about (shown in fig 6.5):

(i) through the edges of the hexagon;
eg. about a row $2\bar{1}0$-000-$\bar{2}10$.

(ii) perpendicular to the faces of the hexagon;
eg. about a row $3\bar{3}0$-000-$\bar{3}30$.

Following are a selection of six representative orientations $(12\bar{1})$, $(12\bar{2})$, $(12\bar{4})$, $(12\bar{5})$, (122) and (120), all involving rotation about the row $2\bar{1}0$-000-$\bar{2}10$.

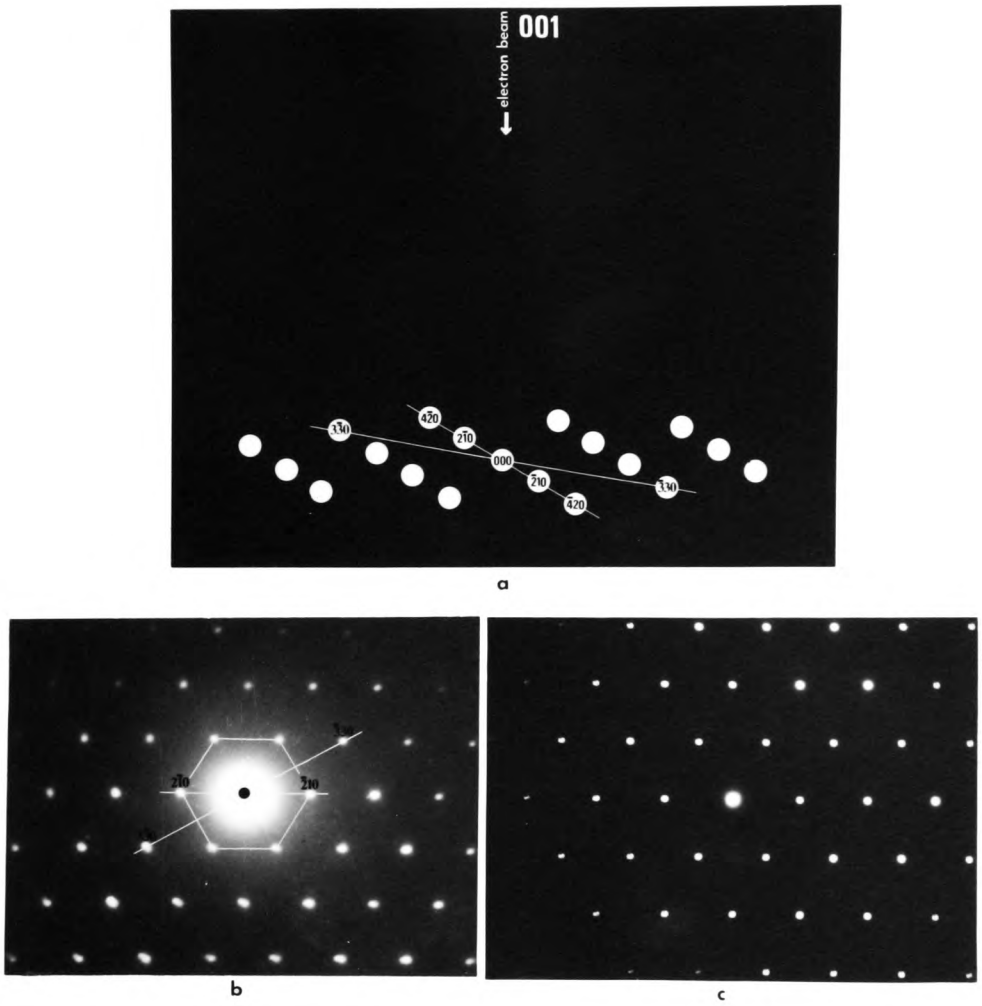

Figure 6.5

A schematic projection of the willemite (001) reciprocal lattice plane (a), and the corresponding electron diffraction photographs for willemite (b) and β" (c).

ORIENTATION ($12\bar{1}$) Fig 6.6 The willemite and β" ($12\bar{1}$) diffraction patterns are identical in form, both with a 'V' pattern of 'superlattice' spots. As might be expected from the electron scattering factors in Table A.3 page 191, the intensity of the β" 'superlattice' spots relative to the strong 'l=3n' spots is markedly less than corresponding 'l≠3n' spots in willemite. That is, the difference between the (Mg+Al) and Si scattering factors is less than the corresponding difference between the Zn and Si scattering factors.

Referring to the willemite reciprocal lattice in fig 6.4, the ($12\bar{1}$) pattern results from orientating the plane containing the $2\bar{1}0$-000-$\bar{2}10$ row and the 113-$\bar{1}23$ row perpendicular to the electron beam.

Now if the plane containing the $\bar{1}\bar{1}0$-000-110 row and the $1\bar{2}3$-$2\bar{1}3$ row is orientated perpendicular to the electron beam, then a pattern of orientation ($1\bar{1}\bar{1}$) is obtained, identical to the ($12\bar{1}$) pattern.

Likewise, if the plane containing the $1\bar{2}0$-000-$\bar{1}20$ row and the $\bar{1}\bar{1}3$-$\bar{2}13$ row is orientated perpendicular to the electron beam, then a pattern of orientation (211) is obtained, also identical to the ($12\bar{1}$) pattern.

These three orientations, ($12\bar{1}$), ($1\bar{1}\bar{1}$) and (211) give identical diffraction patterns, and are related to each other by a 120 degree rotation about the c^* reciprocal lattice axis. This is a result of the 3 fold screw axis of the $R\bar{3}$ space group, about the c axis of the willemite crystal structure. This first series of electron diffraction patterns are referred to as (12ℓ) orientations because this set of indices is easier to work with. Note that a 60 degree rotation would not give the same pattern for a rhombohedral reciprocal lattice, although it would for a hexagonal lattice.

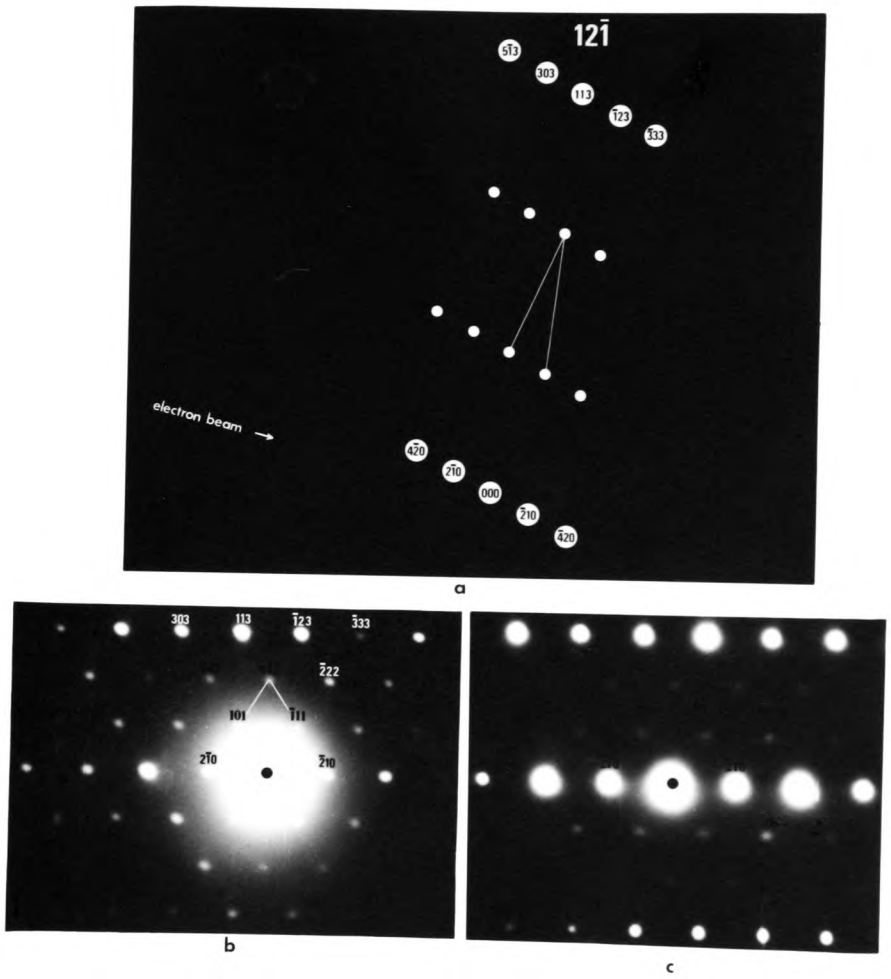

Figure 6.6

A schematic projection of the willemite (12$\bar{1}$) reciprocal lattice plane (a), and the corresponding electron diffraction photographs for willemite (b), and β" (c).

ORIENTATION (122) Fig 6.7

Both the willemite and β" (122) patterns have the same almost orthogonal array of 'superlattice' spots.

ORIENTATION (12$\bar{2}$) Fig 6.7

The willemite (12$\bar{2}$) pattern does not contain any 'superlattice' spots because the reciprocal lattice points 212, 011 etc have ZERO structure factor (ie. do not satisfy the rhombohedral criterion).

However the β" (12$\bar{2}$) pattern has an identical pattern of 'superlattice' spots to the β" (122) orientation.

The (12$\bar{3}$) electron diffraction patterns of both willemite and β" do not contain any 'superlattice' spots and are not shown.

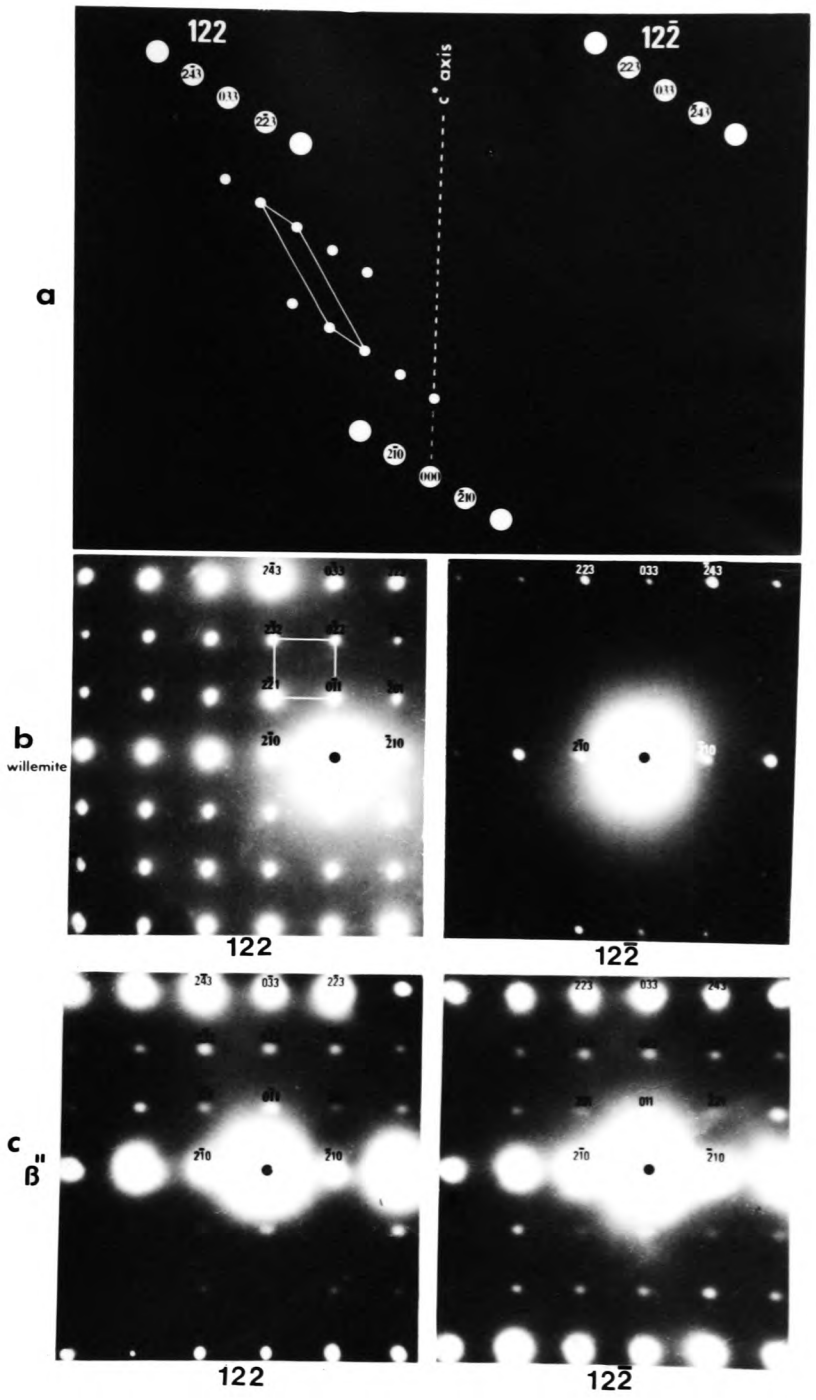

Figure 6.7

A schematic projection of the willemite (122) and (12$\bar{2}$) reciprocal lattice planes (a), and the corresponding (122) and (12$\bar{2}$) electron diffraction photographs of willemite (b) and β" (c).

ORIENTATION($12\bar{4}$) FIg 6.8 Both the ($12\bar{4}$) willemite and β" electron diffraction photographs have the same form of orthogonal array of 'superlattice' spots. In this orientation all the 'superlattice' spots obey the rhombohedral criterion.

•

ORIENTATION ($12\bar{5}$) FIg 6.9 The β" ($12\bar{5}$) diffraction pattern contains another 'V' pattern of superlattice spots all NOT obeying the rhombohedral criterion. Hence the corresponding willemite pattern (not shown) does not have any 'superlattice' spots.

Note that in the β" ($12\bar{5}$) photograph there are four weak spots (211, $\bar{2}31$, $\bar{2}\bar{1}\bar{1}$ and $2\bar{3}\bar{1}$) from the adjoining ($12\bar{4}$) reciprocal plane observable arrowed in the ($12\bar{5}$) photograph. Likewise there are a some ($12\bar{5}$) superlattice spots barely visible in the β" ($12\bar{4}$) photograph arrowed. This is because as the observed reciprocal lattice planes become more oblique, the planes are very close to each other near the $2\bar{1}0$-000-$\bar{2}10$ axis of rotation, and reciprocal lattice points in the rows immediately next to this axis may be extended enough in nature to protrude into an adjoining plane.

This phenomenonis not observable in the corresponding willemite ($12\bar{4}$) photograph as there are no 'superlattice' spots in the ($12\bar{5}$) photograph.

•

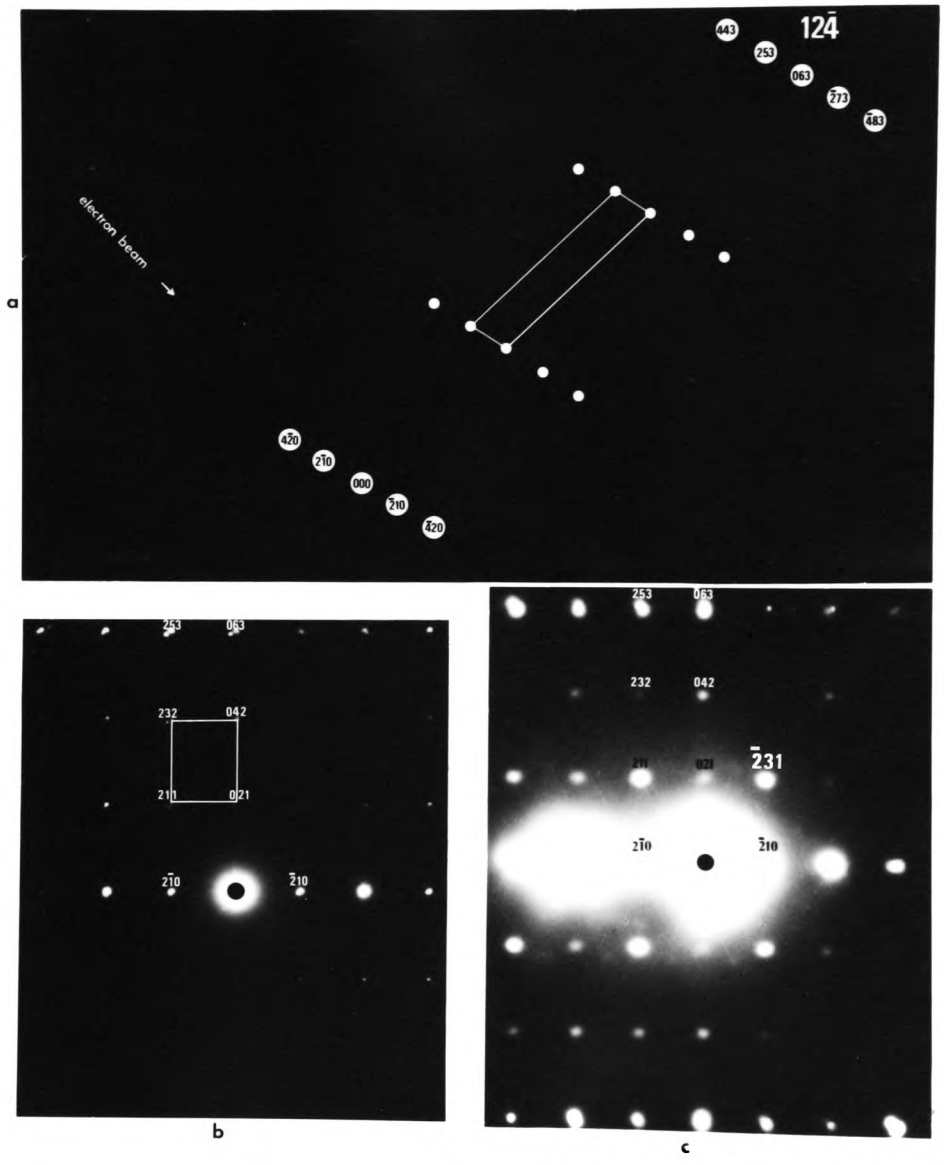

Figure 6.8

A schematic projection of the willemite ($12\bar{4}$) reciprocal lattice plane (a), and the corresponding electron diffraction photographs of willemite (b) and β" (c).

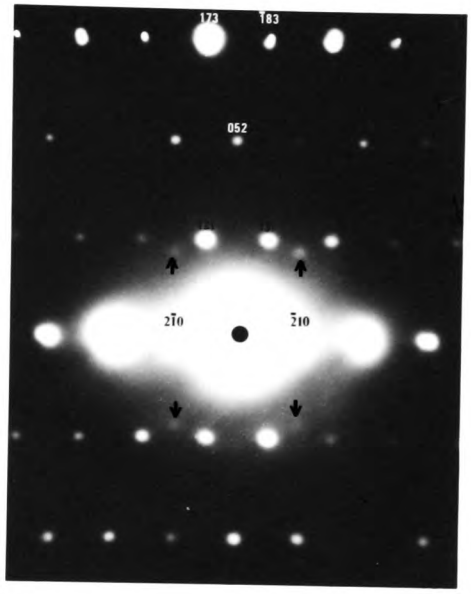

Figure 6.9

An electron diffraction photograph of the β" $(12\bar{5})$ pattern.

ORIENTATION (120) There are no 'superlattice' spots lying in the (120) willemite plane as can be seen in the schematic projection of the willemite (120) reciprocal lattice plane in fig 6.10 (a).

The β" (120) electron diffraction pattern is shown in fig 6.10 (b), with no superlattice spots present. Now starting from this (120) orientation, and by rotating the β" crystal a few degrees about its c-axis, which in effect involves rotating the reciprocal lattice about 006-003-000-00$\bar{3}$-00$\bar{6}$ row of spots, results in the disappearance of all the spots not in this particular row. This is illustrated by progressive rotations of a few degrees in photographs (c) and (d).

However, as can be clearly seen in (d), the 003 and 00$\bar{3}$ diffraction spots also disappear out of this particular row, showing that these two reflections are in fact absent (have zero structure factor) and that their presence in the β" (120) photograph is a result of multiple diffraction.

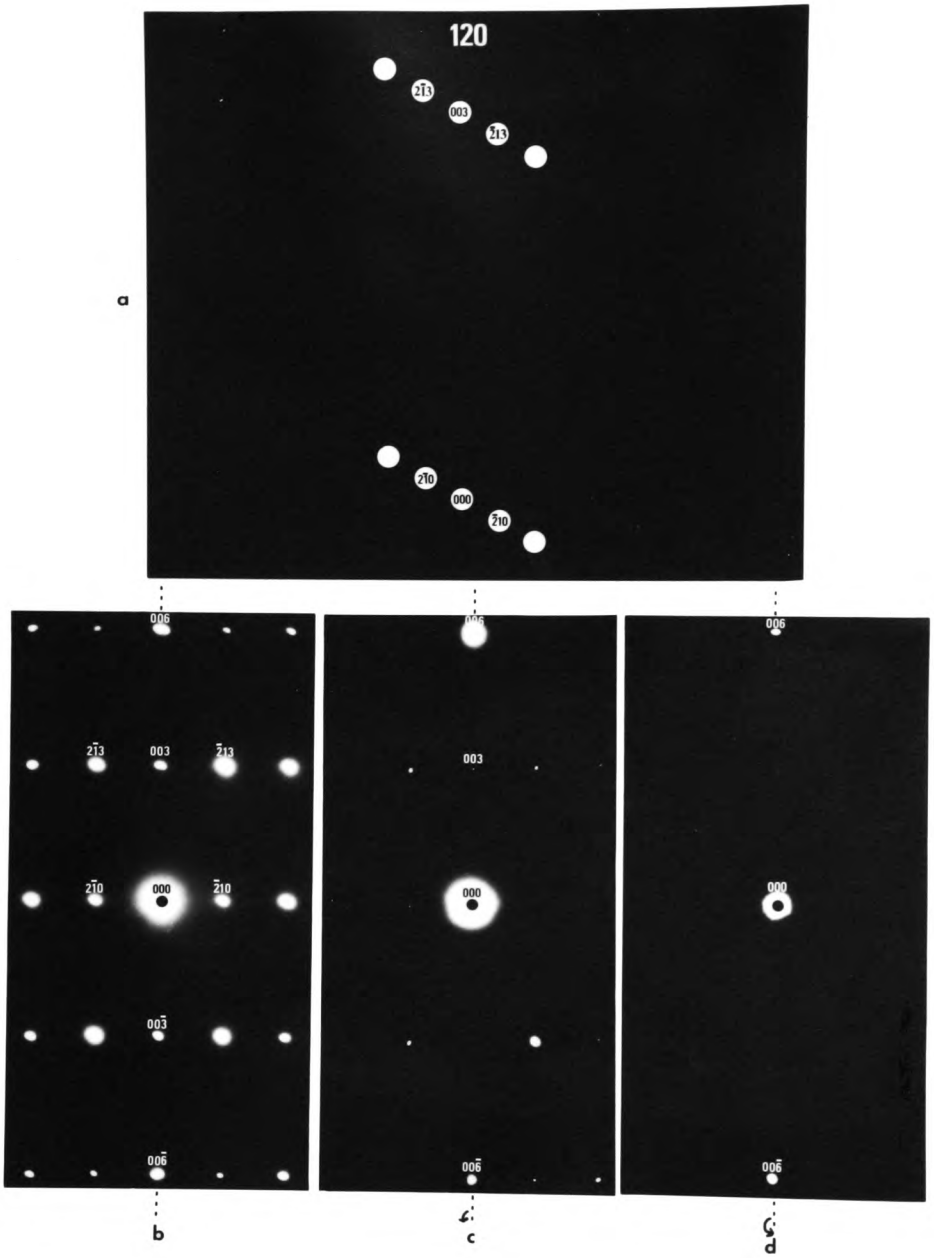

Figure 6.10

A schematic projection of the willemite (120) reciprocal lattice plane (a), and the corresponding (120) electron diffraction of M6 β" (b). (c) and (d) involve rotations of the β" (120) pattern about the 006-000-00$\bar{6}$ row.

Following are two examples of electron diffraction patterns obtained by rotation about the $3\bar{3}0$-000-$\bar{3}30$ row.

ORIENTATION ($11\bar{1}$) Fig 6.11

The ($11\bar{1}$) orientation involves a 56 degree rotation about the $3\bar{3}0$-000-$\bar{3}30$ row.

The β" ($11\bar{1}$) photograph has a 'V' pattern of 'superlattice' spots. There are diagonal rows of superlattice spots (eg. 202 and 101) obeying the rhombohedral criterion, and other diagonal rows of superlattice spots (eg. $3\bar{1}2$ and $3\bar{2}1$) not obeying this criterion.

ORIENTATION (110) Fig 6.12

The (110) reciprocal lattice plane involves a 90 degree rotation about the $3\bar{3}0$-000-$\bar{3}30$ axis of the basal plane.

The β" (110) photograph has an orthogonal array of 'superlattice' spots. This array of 'superlattice' spots both contains diagonal rows of spots obeying the rhombohedral criterion eg. $\bar{1}11$, and $\bar{2}22$, and also diagonal rows of spots not obeying this criterion eg. $\bar{2}12$ and $\bar{2}21$.

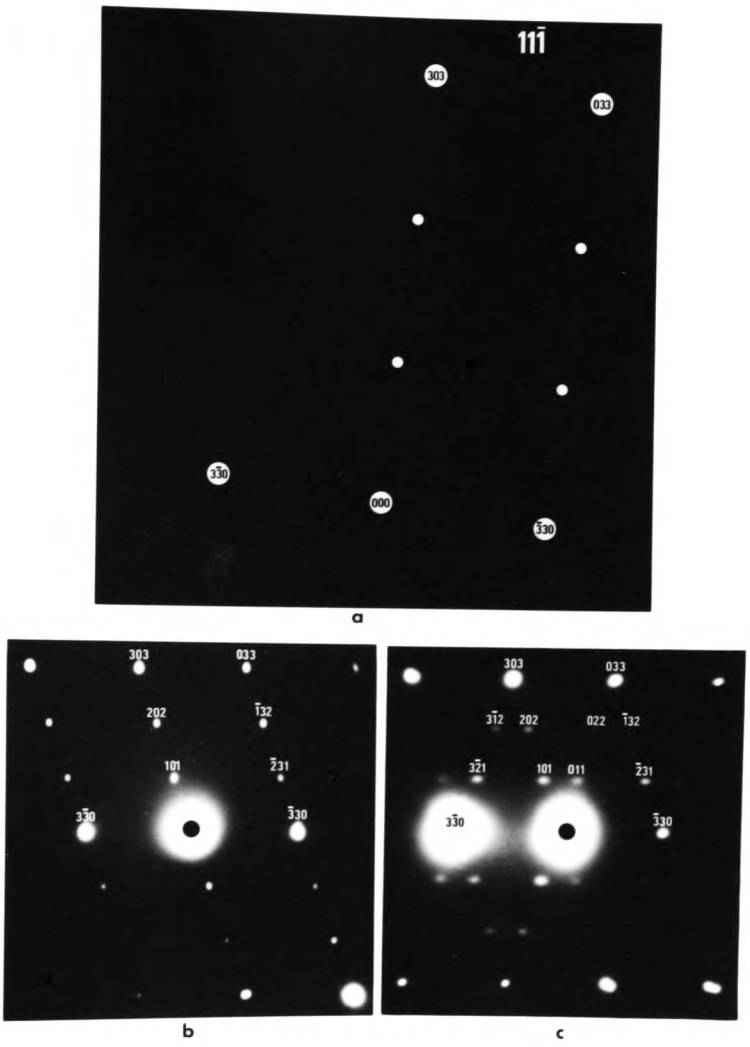

Figure 6.11

A schematic projection of the willemite ($11\bar{1}$) reciprocal lattice plane (a), and the corresponding electron diffraction photographs of willemite (b) and β" (c).

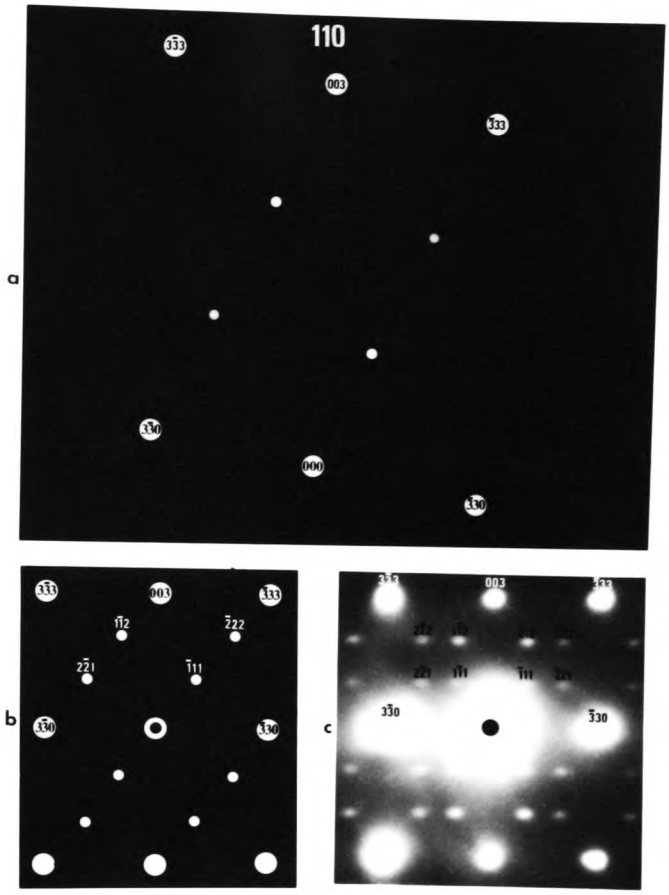

Figure 6.12

A schematic projection of (a) the willemite (110) reciprocal lattice plane and (b) a representation of the willemite (110) pattern, and the corresponding electron diffraction photograph of β" (c).

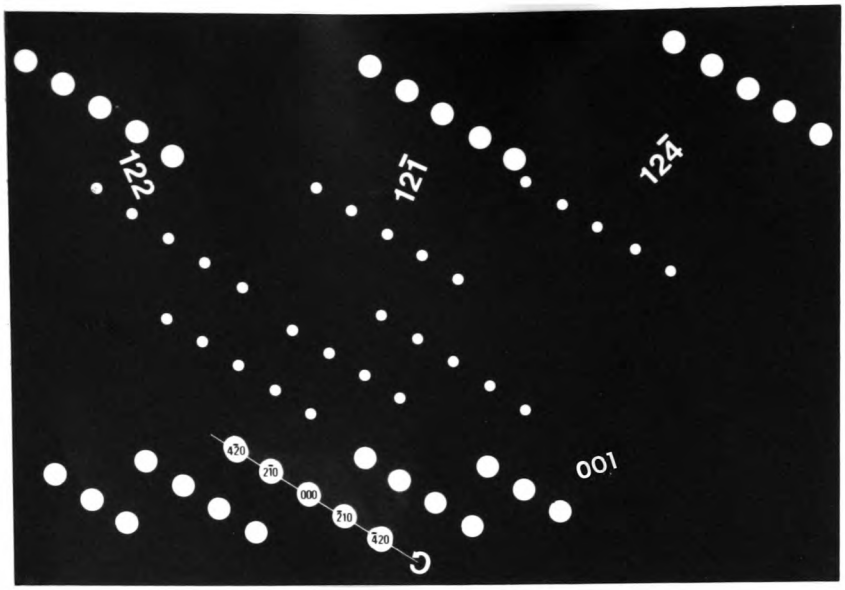

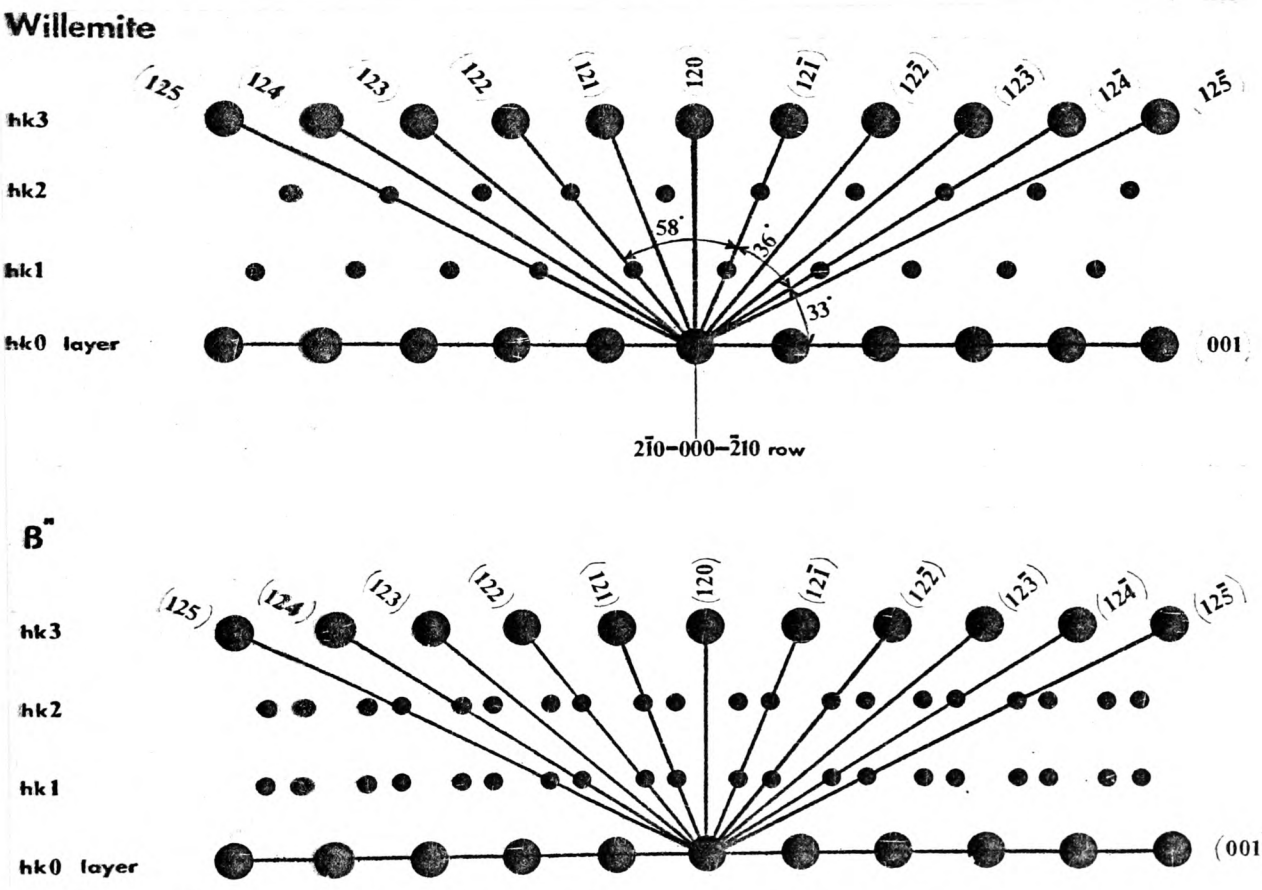

Figure 6.13

(a) A schematic projection of the willemite reciprocal lattice illustrating the (001), (122), (12$\bar{1}$), and (12$\bar{4}$) reiprocal lattice planes together.

Schematic projections of (b) the willemite reciprocal lattice and (c) the β" reciprocal lattice looking down the 2$\bar{1}$0-000-$\bar{2}$10 row normal to the page.

6.2.4 Summary of willemite and β" electron diffraction photographs.

As can be seen from the preceding section, in some orientations the patterns of 'superlattice' spots in the willemite and β" diffraction photgraphs are identical, eg. (122), (12$\bar{1}$) and (12$\bar{4}$).

However, in the (110) and (1$\bar{1}$1) electron diffraction photographs there is a marked difference in the patterns of the 'superlattice' spots obtained for willemite and the M6 β". There are some 'superlattice' spots present in these two β" photographs that do NOT obey the rhombohedral criterion, as discussed on page 171.

In the (12$\bar{2}$) and (12$\bar{5}$) β" electron diffraction photographs all the 'superlattice' spots do NOT obey the rhombohedral criterion, and in the corresponding willemite photographs there are of course no 'superlattice' spots at all.

For the (12ℓ) series of patterns this is summarized in fig 6.13 on page 174, where in (a) a schematic projection of the willemite reciprocal lattice illustrating the (001) basal plane and three of the willemite reciprocal lattice planes that do have 'superlattice' spots in them, (122), (12$\bar{1}$) and (12$\bar{4}$), are shown.

Between the basal hexagonal pattern and the (12$\bar{4}$) pattern there is a series of more and more oblique reciprocal lattice planes. However these become so extended in nature that due to the curvature of the Ewald sphere they become unobservable as plane sections.

Fig 6.13 (b) shows a schematic projection of the willemite reciprocal lattice looking down the 2$\bar{1}$0-000-$\bar{2}$10 row (normal to the page) showing edge on views of the (12$\bar{5}$)...(120)...(125) reciprocal lattice planes. This clearly illustrates which of the (12ℓ) willemite electron diffraction patterns contain 'superlattice' spots

and which do not; for willemite,

(125), (122), (12$\bar{1}$), (12$\bar{4}$), contain 'superlattice' spots.

(124), (123), (121), (120), (12$\bar{2}$), (12$\bar{3}$), (12$\bar{5}$) do NOT contain 'superlattice' spots because there are no such spots present with indices obeying the rhombohedral criterion.

Now in constructing a similar projection of the β" reciprocal lattice looking down the 2$\bar{1}$0-000-$\bar{2}$10 row, rows of spots with indices not obeying the rhombohedral criterion are included, as is shown in fig 6.14 (c). Now according to this projection; for β" (M6):

(125),(124), (122),(121), (12$\bar{1}$),(12$\bar{2}$), (12$\bar{4}$),(12$\bar{5}$) contain superlattice spots,

(123), (120), (12$\bar{3}$), do NOT contain 'superlattice' spots.

This is consistent with all the observed β" (12ℓ) electron diffraction photographs.

. . .

6.2.5 Conclusions.

The composition results from Chapter Four indicate the likelihood of metal atom ordering in the β" crystals grown from quenched MgSiAlON 3M/4X glasses. The similarity in structures between B-Si_3N_4 and the known 'phenacite' structure of willemite (ie. Zn_2SiO_4 , $(Mg,Al)_2Si(O,N)_4$) suggest that the ordering of the metal atoms in β" may be identical to that in phenacite.

X-ray diffraction results gave no indication of ordering, but this was not unexpected on the basis of the very small differences in X-ray scattering power between Mg, Al, and Si. By comparison the additional reflections due to the ordering of Zn and Si are easily visible on X-ray diffraction photograph of Zn_2SiO_4.

Electron diffraction has proved sufficiently sensitive to detect weak 'superlattice' reflections caused by metal atom ordering. The ability of electron diffraction techniques to detect these very weak reflections is mainly due to :

(i) Lack of background scatter in the electron diffraction photographs, which enables very weak reflections to show up against the surrounding clear film plate.

(ii) Multiple diffraction, which in general enhances weak reflections relative to the strong reflections.

(iii) The significant difference in electron scattering factors between Mg and Si at low angles where electron diffraction has an advantage over X-ray and neutron diffraction.

A number of significant conclusions may be drawn from a comparison of the willemite and M6 β" electron diffraction data.

(a) The patterns of β" and willemite are of similar dimensions confirming the close similarity in cell dimensions for the two structures.

(b) Reflections (hkl) for l≠3n are weak compared with those for l=3n.

In willemite this effect results from the ordering of the Zn and Si atoms along the c axis in the sequence Zn Zn Si Zn Zn Si Zn Zn Si. Exactly the same phenomena is observed for the M6 β" which confirms a similar form of arrangement of atoms along the c axis, and which results in a tripling of the c dimension of the hexagonal cell. Also, as one might expect, the relative intensities of the l≠3n reflections are weaker in β" than in willemite because of the smaller difference in scattering power between the metal atoms present.

(c) Although there is a remarkable similarity in the form of diffraction patterns obtained from the two materials there are also rather subtle differences.

The rhombohedral symmetry of willemite means that when indexing using the larger hexagonal cell only reflections for which -h+k+l=3n are allowed. As summarized in section 6.2.4, 'superlattice' reflections violating this condition are present in β".

From the preceding β" diffraction photographs, the conditions limiting possible reflections are:

hkil	for l=3n,	h-k=3n
	for l≠3n,	h-k≠3n
0001	l=6n	

This suggests that the β" crystal structure must either be hexagonal or trigonal. However there is conflicting evidence : a condition for reflection for a triple hexagonal unit cell is 'h-k=3n' and this does not apply to the M6 β" as can be seen from the observation of diffraction spots with indices of 101, $\bar{1}11$, and 012 in fig 6.6 (c) page 163. Now the 003 and $00\bar{3}$ reflections are shown to be caused by multiple diffraction in the β" (120) pattern, when in fact such reflections with l=3n are allowed for all trigonal space groups. It may be that the 003 and $00\bar{3}$ reflections are too weak to be observed.

Two possible reasons for these subtle differences could be that the M6 β" has a slightly different metal atom ordering scheme than willemite, or, that β" has the willemite structure but the presence of 'ordered microdomains' is giving rise to a pseudo-symmetry. These two alternatives are discussed as follows.

In Appendix One a structure factor analyse is presented for an alternative metal atom ordering scheme involving the trigonal space group $P\bar{3}$, different to the phenacite arrangement, but one that preserves the metal atom sequence ..$(Mg,Al)_2Si(Mg,Al)_2Si$.. along the the c-axis. This alternative ordering scheme involves Mg:Al ordering in a 5:1 ratio as well as the (Mg,Al):Si ordering in the 2:1 ratio. β-Si_3N_4 coordinates are transformed into the large hexagonal cell and structure factors calculated for a selection of reflections to give an indication of whether this ordering scheme, or schemes like them, might account for the differences in the electron diffraction photographs of willemite and β".

This alternative scheme does give low structure factors for all the

'superlattice' reflections not obeying the rhombohedral h-k+l=3n condition. However, it also gives low structure factors for reflections that do not appear in the ß" electron diffraction photographs, such as 001, 002, 004, 005, and 010, 100, 103 and 106 (see Table A4). Attempts to devise an ordering scheme which reproduces exactly the observed ß" diffraction phenomena have met with only this limited success.

An alternative explanation for the differences between the willemite and ß" electron diffraction photographs is that the M6 ß" has in fact the true willemite structure, but ordered microdomains are resulting in reflections not satisfying the rhombohedral condition appearing in the electron diffraction photographs.

For example if two ordered microdomains, each with the willemite structure, exist adjacent to each other and are related by a 60 degree rotation about the hexagonal c-axis, then the (122) and (12$\bar{2}$) electron diffraction patterns taken from this volume of crystal would be identical in form as they are in fig 6.7 (c) and (e) on page 165. Such 'microdomain twins or triplets' would normally be visible (imaged) in dark field if the 'superlattice' reflection was of sufficiently large intensity and the domain size was easily resolvable.

Whether the structure of M6 ß" is identical to that of willemite and the extra spots are a result of 'ordered microdomains', or whether there is a subtle difference in the two structures resulting from differences in cation ordering which give rise to the extra reflections in M6 B" is as yet unproven and more work is required to confirm one or other of these hypotheses. However there is no doubt that the two structures are very nearly identical.

. . .

CHAPTER SEVEN.

OVERVIEW.

7.1

This work confirms the existence of magnesium substituted β'sialons, termed β", with a range of compositions in the MgSiAlON 3M/4X plane. All the β" compositions specifically analysed in this work by EDAX (TEM) are plotted on the MgSiAlON 3M/4X phase diagram in fig 7.1

Jack's claim (34) of a significant degree of magnesium substitution in the β'sialon structure is confirmed, but only under certain conditions; while Gauckler's (35) conclusion that 'very little or no magnesium entered the β'-Si_3N_4 when he hot-pressed low level magnesium compositions in the 3M/4X plane of the MgSiAlON system is explained. This previously conflicting evidence for the existence of magnesium substituted B'sialons is resolved with the realisation that there exists in these systems metastable phases, which are formed as devitrification products of liquids or glasses.

Gauckler analyzed β' sialon crystals formed at a hot-pressing temperature of 1700°C, finding negligible magnesium present. Now Gauckler's specimens, if cooled rapidly should have contained a thin layer of β" on the outside of the β' sialon crystals resulting from crystallization of the residual liquid on cooling. That this was not observed was because any β" so formed was below the detection limit for X-ray diffraction analysis and not obvious by microscopy, or because a rapid cooling rate was not used. It is also unlikely that the liquid composition in Gauckler's specimens had a composition in the 3M/4X plane, which is crucial for β" formation.

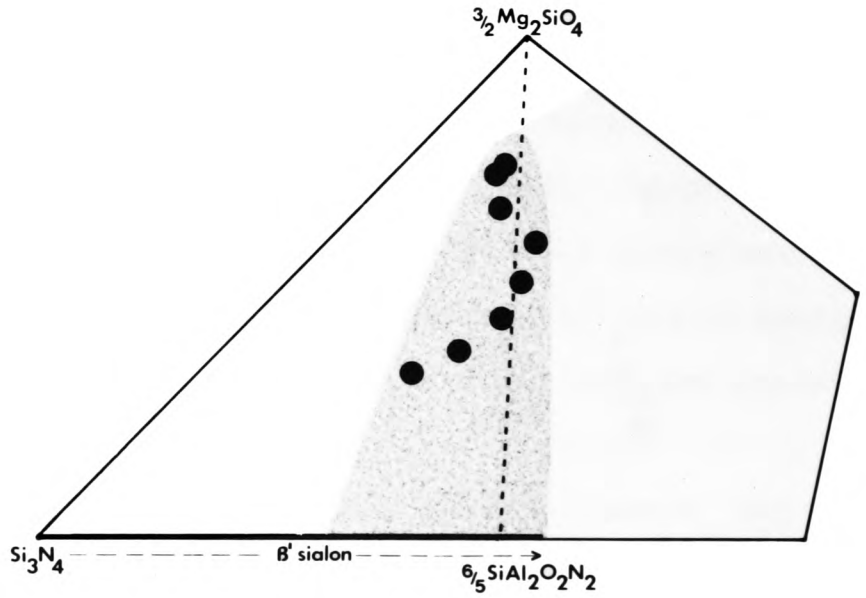

Figure 7.1

Magnesium substituted β'sialon, β", compositions plotted on the 3M/4X MgSiAlON composition plane. The general region of β" formation is shaded. These β" compositions here are a combination of those in fig 4.10 (page 95) and fig 5.11 (page 135).

The metastable nature of β" means that magnesium substituted β'sialons transform to stable crystalline products at high temperatures. The range of β" composition gives a corresponding range of thermal stability, with a high magnesium content β" stable only up to 1120°C, while β" crystals with lower magnesium levels are able to exist up to 1350°C.

β" formation is made possible by the ability of an undercooled liquid/glass to reduce its free energy in a stepwise process via intermediate metastable crystalline products. The growth of magnesium substituted β'sialons is a function of the liquid/glass composition that they are derived from and the crystallization mechanism. Two distinct crystallization mechanisms for β" growth are encounted in this work:

(i) Heterogenous nucleation and growth - where one phase, β", crystallizes at a similar composition to the glass matrix.

(ii) Coupled growth - where two phases, β" and forsterite, grow cooperatively.

7.2

The heterogenous nucleation and growth of high magnesium content β" is obtained by quenching a MgSiAlON liquid of appropriate composition to a glass followed by annealing at a temperature above the glass transition temperature. The conditions for β" growth in a MgSiAlON glass are that:

(a) The glass composition must be in the 3M/4X plane.

(b) β'sialon nuclei must be present to catalyze β" growth.

(c) The annealing temperature must be low enough to avoid the growth of competing stable crystalline phases eg.forsterite.

This means that the possible β" composition range is limited by the ability to form a MgSiAlON glass with such nuclei; that is to a composition sector bounded by the eutectic and the reaction temperature isotherm (1650°Cfor this work).

The degree of β" crystallization which can be achieved is very sensitive to both composition and impurity levels. The presence of calcium impurity which cannot be incorporated into the β" lattice, prevents the crystallization of the final glass and also appears to promote competing forsterite growth at temperatures over 1025°C. There is a tendency for high magnesium content β" to form at compositions along the Mg_2SiO_4-$Al_2SiO_2N_2$ line, as shown by the composition analyses of fig 4.10 , and by the (Mg,Al):Si ordering in the ratio of 2:1 for the M6 B" specimen shown by the electron diffraction work of Chapter Six.

These factors together with the difficulty of preparing a glass with a cation:anion ratio of exactly 3:4 and containing a fine dispersion of B' nuclei, mean that it is difficult to crystallize such a glass completely as β". A level of 91-93 %volume of β" was the best achieved in this work.

The driving force for the transformation of the M6 MgSiAlON glass to crystallize as β" comes from the improvement in long-range order obtained. Very little atomic rearrangement is necessary for this transformation as the β" and glass compositions are so similar. Such first-order solid-solid transformations which proceed by mechanisms involving the minimum atomic rearrangement are known as 'topotactic' transformations (77). In such transformations it is usually found that the anion framework tends to remain largely unchanged and that the smaller, highly charged cations tend to migrate most readily.

The crystallization of M6 β" at an annealing temperature of 910°C resulted in β" crystals with only weak diffuse additional 'superlattice' reflections (fig 6.1) indicative of partial ordering of Mg and Al with respect to silicon. However on annealing at 980°C these additional reflections were sharp, indicative long range ordering. This suggests that the diffusion paths for the glass to crystalline β" transformation are in fact shorter than the diffusion paths involved in the (Mg,Al)/Si ordering process, and, therefore when crystallization of the glass occurs at low temperatures there is a tendency for the cations to be disordered as they are in the glass.

The short diffusion paths involved in the crystallization of the β" in the M6 MgSiAlON glass provide an easy way for the system to reduce its free energy. However the rapid disappearance of the high magnesium content M6 β" at temperatures over 1120°C furnishes proof of its metastable character. This instability may result from the following factors:

(i) The relatively large magnesium atom may introduce considerable strain into the β' lattice.

(ii) Magnesium has a preference for octohedral coordination, such as in forsterite, rather than the tetrahedral coordination of the β' lattice.

In Chapter Six the existence of ordered microdomain twins was suggested as a possible explanation for the appearance of 'superlattice' spots in the M6 β" electron diffraction photographs violating the rhombohedral condition for reflection (page 180). Although this is hypothetical at this stage, the driving force for the formation of these twins in such a high magnesium content β" could be a

reduction in overall lattice strain energy achieved by the reversal of shear distortion across adjacent micro-twins, similar to that found in vanadium carbide (86).

7.3

The second mode of β" growth is via a coupled mechanism with forsterite from a eutectic (or near eutectic) liquid, producing a duplex eutectic structure, as discussed in Chapter Five. This growth mechanism is crucially dependent on the cooling rate employed, with a rate of roughly 10°C/min found suitable. Cooling rates appreciably faster than this do not give the liquid enough time to fully crystallize, and cooling rates appreciably slower tend to contain a third phase, Q phase.

This coupled growth produces β" of relatively low magnesium content with much of the available magnesium being incorporated in the forsterite, Mg_2SiO_4. β-Si_3N_4/β'sialon nuclei are not required for the nucleation of β" by this coupled mechanism. However, the inability of the β" to nucleate at small undercoolings results in a duplex microstructure with long anomalous forsterite crystals dispersed through it.

This tendency for the eutectic MgSiAlON liquid in the 3M/4X plane to form anomalous forsterite crystals, together with the frothing that occurs in these liquids on slow cooling producing a porous product, probably limits the production of a directionally solidified 'normal' eutectic forsterite/β" material.

7.4

The ability of MgSiAlON liquids in the 3M/4X composition plane to crystallize as β" or as a mixture of forsterite/β"/Q phase, means that the residual liquid in a β'sialon material (sintered using a MgSiAlON liquid) may be crystallized as a grain boundary phase. The effectiveness of this would depend on how closely the composition of the residual liquid could be maintained within the 3M/4X plane at the end of the sintering process.

Given that this is possible, a rapid cooling rate followed by annealing between 900-1000°C would crystallize the grain boundary phase almost completely as β" ; a crystalline phase, but one appreciably softer than β'sialon. This grain boundary phase would be stable up to about 1120°C.

A slow cooling rate, or annealing the quenched product material at temperatures above 1120°C, would crystallize the grain boundary material as a mixture of forsterite together with of one or more the following phases, low magnesium content β", Q phase or spinel. This grain boundary would be stable to at least the vicinity of the eutectic temperature of 1420°C.

The ability of these grain boundary phases to improve the thermomechanical properties of sintered β'sialon materials should be worthwhile investigating provided that the first objective of maintaining accurate control over the residual liquid can be realized.

The properties of a β" glass ceramic similar to the M6 MgSiAlON specimen (see fig 4.5 (b)) may also be worthwhile investigating.

. . .

APPENDIX A

Structure factor calculations for M6 β" Metal atom ordering schemes.

The electron diffraction photographs of the M6 β" presented in Chapter Six contain additional 'superlattice' reflections violating the '-h+k+l=3n' rhombohedral condition of the phenacite-type structure. Here, structure factor analyses for the β" (M6 composition) are calculated for the phenacite-type metal atom ordering and alternative ordering schemes. These are compared with the observed reflections in the M6 β" electron diffraction patterns to see if the occurrence of the additional reflections can be explained. A computer programme was written for calculation of structure factors.

The calculation of structure factors according to equation (13) page 45 requires the coordinates of all the atoms in the unit cell, and the atomic scattering factors for electrons of Mg, Si, Al, O, N.

A.1 Atomic coordinates.

The coordinates of β-Si_3N_4 (82) can be transformed from the small primitive hexagonal cell 'h' to the large hexagonal cell 'H' (83). The transformation matrix for this transformation is given in Table A.1.

Table A.1 (83).

	H1		
	x_1	y_1	z_1
	2/3	1/3	0
P	-1/3	1/3	0
	0	0	1

The structure of β-Si_3N_4 (see Wild et al (82)) is described by the hexagonal space group $P6_3/m$ (No.176 International Tables), in which :

(1) six silicon atoms in the unit cell occupy 6h positions with

$$x = 0.172,\ y = 0.769,\ z = 0.250,$$

(2) six nitrogen atoms occupy 6h positions with

$$x = 0.333,\ y = 0.033,\ z = 0.250,$$

(3) and two nitrogen atoms in 2h positions with

$$x = 0.333,\ y = 0.667,\ z = 0.250.$$

These positions transform to the large hexagonal cell as follows:

(A) $x_h = 0.8583,\ y_h = 0.3137,\ z_h = 0.2500$

(B) $x_h = 0.2110,\ y_h = 0.1220,\ z_h = 0.2500$

(C) $x_h = 0.0000,\ y_h = 0.3333,\ z_h = 0.2500$

In the phenacite structure (see Bragg and Zachariesen (78)), the space groupis $R\bar{3}$ (No.148 International Tables) and there are 126 atoms in the unit cell. The coordinates of the equivalent positions are :

$$(0,0,0;\ 1/3, 2/3, 2/3;\ 2/3, 1/3, 1/3)\ +$$
$$x,y,z;\quad -y,x-y,z;\quad y-x,-x,z;$$
$$-x,-y,-z;\quad y,y-x,-z;\quad x-y,x,-z.$$

Assuming initially that the atomic arrangement in β" (M6) is identical to that in phenacite, and using the β-Si_3N_4 coordinates transformed to the larger hexagonal cell, the coordinates for β" (M6) are shown in Table A.2.

Table A.2

β" (M6) 'atomic coordinates' (derived from β-Si_3N_4 coordinates and phenacite structure).

		x	y	z
18	Si in 18f at	0.8583	0.3137	0.2500
18	$(Mg,Al)_1$ in 18f at	0.8583	0.3137	0.5833
18	$(Mg,Al)_2$ in 18f at	0.8583	0.3137	0.9167
18	$(O,N)_1$ in 18f at	0.0000	0.3334	0.2500
18	$(O,N)_2$ in 18f at	0.2110	0.1220	0.2500
18	$(O,N)_3$ in 18f at	0.2110	0.1220	0.5833
18	$(O,N)_4$ in 18f at	0.2110	0.1220	0.9167

These coordinates are now taken as the basic atomic positions within which different ordering schemes are tried.

A.2 Electron atomic scattering factors.

The atomic scattering of electrons is due to two factors :

(1) The Rutherford scattering from the nucleus.

(2) Scattering from the electron cloud.

For covalent or metallic structures the wave function of the valency electrons may not be well known and so the accuracy of the calculated scattering factors is therefore limited. The table of atomic scattering factors for electrons shown below in Table A.3 gives an indication of the differences in scattering amplitudes of the atoms present in β"-MgSiAlON.

Table A.3

Atomic scattering factors for electrons (100 KV),(81).

El	z	(sin θ) / (A^{-1})				
		0.10	0.15	0.20	0.25	0.30
Mg	12	4.29	3.14	2.33	1.79	1.45
Al	13	5.07	3.74	2.75	2.07	1.63
Si	14	5.26	4.08	3.10	2.36	1.84
N	7	2.20	2.10	1.91	1.68	1.44
O	8	2.01	1.95	1.80	1.62	1.42

In the structure factor calculations for β" (M6) with the phenacite ordering scheme, the Mg and Al atoms are distributed randomly in positions $(Mg,Al)_1$ and $(Mg,Al)_2$ (see TableA.2), and hence the scattering factors used for these positions are a weighted average of the Mg and Al scattering factors according to the Mg/Al ratio in the β" (M6) composition.

Bacon et al (84) in a neutron diffraction investigation of some β'-sialons suggested that there is a tendency for the smaller oxygen atoms to preferentially fill the 2c positions, which are equivalent to the $(ON)_1$ positions in Table A.2. In the β" (M6) composition 13% of the non-metal sites are occupied with nitrogen atoms, and these may therefore tend to be in the 6h related positions ie. (ON_2), (ON_3), (ON_4). However it is assumed here that any such ordering would not produce reflections strong enough to be visible as the difference in atomic scattering factors between oxygen and nitrogen is negligible (

Table A.3). Hence the scattering factors used for the cation positions are a weighted average according to the O/N ratio in the β" (M6) composition.

The β" (M6) electron diffraction photographs presented in Chapter Six show a tripling of the c-axis dimension indicative of ordering of the metal atoms in a 2:1 ratio. Now compositions with a (Mg,Al):Si ratio of 2:1 lie along the line $Mg_4Si_2O_8$-$Si_2Al_4O_4N_4$. The composition of the M6 β", as analyzed by EDAX, lies close to this line as shown in fig 4.10 on page 95, but not exactly on it. The β" composition used in the structure factor calculations is however taken as the composition on this $Mg_4Si_2O_8$-$Si_2Al_4O_4N_4$ line lying closest to the M6 composition, that is :

Mg	Al	Si	O	N
3.28	0.72	2	7.28	0.72

As there are 126 atoms in the large (triply primitive) hexagonal unit cell, the formula, quoting compositions to the nearest whole number, is expressed as :

Mg	Al	Si	O	N
30	6	18	66	6

or

(Mg,Al)	Si	(O,N)
36	18	72

In considering the ordering of the metal atoms there are 54 metal atoms in the unit cell, 6 layers each of nine atoms.

A.3 Comparison of metal atom ordering schemes.

Structure factors are presented for an arrangement with the metal atoms disordered, phenacite-type ordering and for an alternative schemebased on the trigonal space group $P\bar{3}$.

The calculated structure factor, F, is given for a representative

selection of hkl reflections (the 00ℓ, 01ℓ, 10ℓ, and the 11ℓ sets of reflections). In the fourth column the observed diffraction spots on the M6 TEM diffraction photographs are listed as either 'strong' spots or 'weak' (superlattice) spots.

Table A.4

Structure factors for β" metal atom ordering arrangements.

	(1)	(2)	(3)	(4)
hkl	disordered	phenacite ($R\bar{3}$)	$P\bar{3}$	TEM
(h-k=3n)				
000				
001	0	0	-4.7	0
002	0	0	2.3	0
003	0	0	0	0
004	0	0	-1.1	0
005	0	0	1.3	0
006	-160.5	-160.5	-160.5	strong
(h-k≠3n)				
010	0	0	-1.4	0
011	0	0	2.3	weak
012	0	3.6	1.8	weak
013	0	0	1.6	0
014	0	0	-0.6	weak
015	0	-3.8	-4.1	weak
016	0	0	0.2	0
(h-k=3n)				
110	-35.4	-35.4	-35.4	strong
111	0	0	1.4	0
112	0	0	-1.7	0
113	88.1	88.1	88.1	strong
114	0	0	-0.7	0
115	0	0	0.2	0
116	12.3	12.3	12.3	strong
(h-k≠3n)				
100	0	0	-1.4	0
101	0	6.0	7.2	weak
102	0	0	1.3	weak
103	0	0	-1.5	0
104	0	-2.7	-0.5	weak
105	0	0	-0.6	weak
106	0	0	0.2	0

The structure factor analysis in column (1) is that of a completely disordered arrangement of metal atoms. As one would expect the only reflections allowed are hkl reflections with both l=3n and h-k=3n, that is the same reflections as for β-Si_3N_4, with no 'superlattice' reflections present.

The phenacite ordering scheme in column (2) has the (Mg,Al) atoms ordered with respect to the Si atoms. In addition to the identical strong reflections for (1), there are now reflections with very low structure factors where the hkl indices obey the rhombohedral criterion of h-k+l=3n, that is 'superlattice' reflections. However as previously shown in Chapter Six there are superlattice spots observed for β" (M6) not accounted for by this phenacite ordering, eg. the 011 and 014 reflections.

For the trigonal space group $\bar{P}3$ arrangement, the (Mg,Al) atoms are ordered with respect to the Si atoms in a 2:1 ratio. It is also possible that the Mg atoms are ordered with respect to the Al atoms as well as the (Mg,Al) to Si ordering. The coordinates of the equivalent positions of the $\bar{P}3$ space group were used to generate atomic coordinates allowing the Mg and Al atoms of the $(Mg,Al)_1$ and $(Mg,Al)_2$ metal atoms of Table A2 to be ordered on particular sites in a 5:1 ratio. The structure factors for such an arrangement give an indication of how this second level of ordering may affect the occurrence of 'superlattice' spots.

This arrangement presented in column (3) does give low structure factors for all the weak 'superlattice' spots observed in the diffraction patterns. However it also gives low structure factors for some reflections where no spots are observed ie. 001, 002, 004, 005, 111, 113 and 010, 100, 103, and 106. This is not strong evidence for a second

level of metal atom ordering between Mg and Al causing the occurrence extra 'superlattice' spots.... see discussions on page 180.

. . .

REFERENCES.

1. D.J.Godfrey, Proc.Br.Ceram.Soc. 22 (1973) 1.
2. F.F.Lange, 'Structural ceramic materials under Technical Paper,75-GT-107,(1975).
3. 'Nitrogen Ceramics', F.L.Riley (ed.), Leyden:Noordhoff,(1977).
4. G.G.Deeley, J.M.Herbert, N.C.Moore, Powder Metall. 8 (1961) 145.
5. G.R.Terwilliger and F.F.Lange, J.Mater.Sci. 10 (1975) 1169.
6. F.F.Lange, 'Silicon nitride polyphase systems: fabrication, microstructure, and properties', International Metals Review,1 (1980) 1.
7. S.Wild, P.Grievson, K.H.Jack and M.J.Latimer, 'The Role of Magnesia in Hot-Pressed Silicon Nitride', Special Ceramics 5 P.Popper (ed), Brit.Ceram.Res.Assoc. (1972).
8. I.C.Huseby and G.Petzow,'Influence of Various Densifying Additives on Hot-Pressed Si_3N_4 ', Powder Metall.Int. 6 (1974) 17.
9. K.H.Jack, 'The Fabrication of Dense Nitrogen Ceramics', 14th University Conference on Ceramic Science, North Carolina State University, (1977).
10. A.Arias, 'Effect of CeO_2,MgO and Y_2O_3 additions on the sinterability of a milled Si_3N_4 with 14.5 wt% SiO_2, J.Mater.Sci.16 (1981) 787.
11. S.Hampshire and K.H.Jack, 'The Kinetics of Densification and Phase Transformation of Nitrogen Ceramics',Special Ceramics 7 Brit. Ceram.Res.Assoc. (1980).
12. D.R.Messier, F.L.Riley, R.J.Brook, J.Mater.Sci. 13 (1978) 1199.
13. P.Drew and M.H.Lewis, 'The microstructures of silicon nitride ceramics during hot-pressing transformation'. J.Mater.Sci.9 (1974) 261.

14. A.J.Evans and J.V.Sharp, ibid. 6 (1971) 1292.

15. D.R.Clarke and G.Thomas, J.Amer.Cer.Soc. 60 (1977) 491.

16. L.K.V.Lou, T.E.Mitchell and A.H.Heuer, 'Impurity Phases in Hot-Pressed Si_3N_4', J.Amer.Cer.Soc. 61 (1978) 392.

17. K.H.Jack,'Ceramics for High Performance Applications', (ed.J.J. Burke ,H.E.Gorum and R.N.Katz), (1974) 285.

18. O.L.Krivanek, T.M.Shaw and G.Thomas, 'The Microstructure and Distribution of Impurities in Hot-Pressed and Sintered Silicon Nitrides', J.Am.Cer.Soc. 62 (1979) 585.

19. P.Popper, A.Giachello, P.C.Martinengo, G.Tommasini, 'Sintering of silicon nitride in a powder bed', J.Mater.Sci. 14 (1979) 2825.

20. F.F.Lange, J.Amer.Cer.Soc. 57 (1974) 84.

21. R.Kossowsky, D.G.Miller and E.S.Diaz, J.Mater.Sci.10 (1975) 983.

22. Salah Ud Din and P.S.Nicholson, J.Mater.Sci. 10 (1975) 1375.

23. J.L.Iskoe,F.F.Lange and E.S.Diaz, J.Mater.Sci. 11 (1976) 908.

24. K.H.Jack and W.I.Wilson, Nature , 238 (1972) 80.

25. Y.Oyama and O.Kamigaito, Jap.J.Appl.Phys. 10 (1971) 1637.

26. L.J.Gauckler, H.L.Lukas, G.Petzow, J.Am.Ceram.Soc. 58 (1975) 346.

27. L.J.Gauckler and G.Petzow, 'Nitrogen Ceramics', NATO Advanced Study Group, University of Kent, (1976).

28. R.J.Lumby, B.North and A.J.Taylor, 'Special Ceramics 6',ed. P.Popper, Brit.Ceram.Res.Assoc. (1974) 321.

29. P.M.Johnson, A.Hendry, 'The microtructure of hot pressed sialon polytypes', J.Mater.Sci. 14 (1979) 2439.

30. M.H.Lewis, B.D.Powell, P.Drew, R.J.Lumby, B.North, A.J.Taylor, 'The formation of single-phase Si-Al-O-N ceramics', J.Mater.Sci. 12 (1977) 61.

31. M.H.Lewis, A.R.Bhatti, R.J.Lumby and B.North, 'The microstructure of sintered Si-Al-O-N ceramics', J.Mater.Sc. 15 (1980) 103.

32. K.H.Jack, Review 'Sialons and related nitrogen ceramics', J.Mater. Sci. 11 (1976) 1135.

33. K.H.Jack, 'The role of additives in the densification of nitrogen ceramics', Final technical report to the European Research Office London, grant no DAERO-76-G-067 (1977) p.16.

34. K.H.Jack, 'Nitrogen Ceramics', Trans.and J.Brit.Ceram.Soc.8 (1973) 376.

35. L.J.Gauckler, J.Weiss and T.Y.Tien, 'Insolubility of Mg in β'-Si_3N_4 in the System Al-Mg-Si-O-N', J.Am.Ceram.Soc. 61 (1978) 397.

36. M.H.Lewis, A.R.Bhatti, R.J.Lumby and B.North, 'Crystallization of Mg-containing phases in β'-Si-Al-O-N ceramics',J.Mater.Sci.15 (1980).

37. I.C.Huseby, H.L.Lukas and G.Petzow, 'Phase Equilibria in the System Si_3N_4-SiO_2-BeO-Be_3N_2', J.Am.Ceram.Soc.58 (1975) 377.

38. C.Greskovisch, 'Hot-pressed β'-Si_3N_4 containing small amounts of Be and O in solid solution.

39. Y.Oyama, Jap.J.Appl.Phys. 11 (1972) 1572.

40. S.Prochazha and G.Greskovich, Bull.Am.Ceram.Soc.57 (1978) 579.

41. R.Kossowsky, 'Microstructure of Hot-Pressed Silicon Nitride', J.Mater.Sci. 8 (1973) 1603.

42. G.E.Gazza, 'Hot-Pressed Si_3N_4', J.Am.Ceram.Soc. 56 (1973) 662.

43. Rustrum Roy, 'Rational Molecular Engineering of Ceramics', J.Am. Ceram.Soc. (1977) 350.

44. A.Tsuge, K.Nishida, M.Komatsu, 'Effect of Crystallizing the Grain-Boundary Glass Phase on the High-Temperature Strength of Hot-Pressed Si_3N_4 Containing Y_2O_3', J.Am.Ceram.Soc.58,(1975) 325.

45. A.W.J.M.Rae, D.P.Thompson, N.J.Pipkin, K.H.Jack, Special Ceramics 6, ed.P.Popper, Brit.Ceram.Res.Assoc. (1975) 347.

46. G.E.Gazza, Ceram.Bull. 54 (1975) 778.

47. F.F.Lange,S.Singhal and R.C.Kusnick, J.Am.Cer.Soc.60 (1977) 249.

48. J.E.Weston, P.L.Pratt, B.C.H.Steele, 'Crystallization of grain boundary phases in hot-pressed silicon nitride materials', J.Mat. Sci. 13 (1978) 2137.

49. F.F.Lange, 'Eutectic Studies in the System Si_3N_4-Si_2N_2O-Mg_2SiO_4', J.Am.Ceram.Soc. 62 (1979) 617.

50. D.R.Clarke, 'Microstructure of a 12H Mg-Si-Al-O-N Polytype Alloy, Intergranular Phases and Composition Variations', J.Am.Ceram.Soc. 63 (1980) 208.

51. R.N.Katz and G.E.Gazza,'Processing of Crystalline Ceramics', (Materials Science Research, Vol 11.), (ed H.Palmour), R.F.Davis and T.M.Hare.Plenum, New York.

52. H.O.Mulfinger and H.Meyer, 'Physical and Chemical Solubility of Nitrogen in Glass Melts', Glasiech.Ber. 36 (1963) 481.

53. H.O.Mulfinger, 'Physical and Chemical Solubility of Nitrogen in Glass Melts', J.Am.Ceram.Soc. 49 (1966) 462.

54. H.O.Mulfinger and H.Franz, Glastech.Ber. 38 (1965) 235.

55. T.H.Elmer and M.E.Nordberg, J.Am.Ceram.Soc. 50 (1967) 275.

56. F.L.Harding and R.J.Ryder, Glass Techn. 11 (1970) 54.

57. S.Risbud, 'Analysis of bulk amorphous oxynitride structures using the network theory of glasses', Physics and Chemistry of Glasses, 22 (1981) 168.

58. K.R.Shillito, R.R.Wills and R.B.Bennett, 'Silicon Metal Oxynitride Glasses', J.Am.Ceram.Soc. 61 (1978) 537.

59. R.E.Loehman, 'Oxynitride Glasses', J.Non-Cryst.Sol. 42 (1980) 433.

60. R.A.L.Drew, S.Hampshire and K.H.Jack, 'Nitrogen Glasses', Special Ceramics 7,(ed D.Taylor/P.Popper),Proc.Brit.Ceram.Soc.31 (1980).

61. P.H.A.Roebuck, Ph.D. Thesis, University of Newcastle upon Tyne (1978).

62. T.M.Shaw and G.Thomas, 'Crystallization of Phase-Separated Mg-Si-O-N Glasses',

63. R.R.Wusirika and C.K.Chyung, 'Oxynitride Glasses and Glass-Ceramics', J.Non-Cryst.Solids. 38/39 (1980) 39.

64. 'Application of Transmission Electron Microscopy to Engineering Practice in Ceramics: Introduction, Fundamentals, and Application to Precipitation Phenonmena': A.H.Heuer, J.Am.Ceram.Soc., 62, (1979), 225.

65. 'Applications of Dedicated Scanning Transmission Electron Microscopy to Nonmetallic Materials': J.B.Vander Sande and E.L.Hall, J.Am.Ceram.Soc., 62, (1979), 246.

66. G.Cliff and G.W.Lorimer; Proceedings of the Fifth European Congress on Electron Microscopy, pp.140-141, Institute of Physics, London, England, (1972).

67. G.W.Lorimer and G.Cliff, 'Analytical Electron Microscopy of Minerals',ElectronMicroscopy in Mineralogy,H.R.Wenk(ed)(1976) 506.

68. I.C.Huseby, G.A.Slack and R.H.Arendt, 'Thermal Expansion of $CdAl_2O_4$, β-Si_3N_4, and Other Phenacite-Type Compounds, Ceram.Bull. 60 (1981) 919.

69. S.D.Stookey and R.D.Maurer, 'Catalyzed Crystallization of Glass-Theory and Practice.

70. Werner Vogel (ed), 'Structure and Crystallization of Glasses' (Permagon) 174.

71. M.L.Jackson and Mackensie, 'Soil Clay Mineralogy' (ed.Rich and Kunze) (1964) Chapel Hill, Univ. of North Carolina Press.

72. R.W.Rinke and E.F.Osborne, J.Am.Ceram.Soc. 37 (1954) 136.

73. F.R.N.Nabarro, Proc.R.Soc.(A) 175 (1940) 519.

74. J.K.Lee and W.C.Johnson, 'Rexamination of the elastic strain energy of an incoherent ellipsoidal precipitate', Acta.Met, 26 (1978) 541.

75. B.Chalmers (ed), 'Principles of Solidification', (1976) p199.

76. R.L.Ashbrook, 'Directionally Solidified Ceramic Eutectics', J.Am.Ceram.Soc. 63 (1977) 428.

77. J.Williamson and F.P.Glasser, 'Crystallization of ZnO-SiO_2 Liquids and Glasses', Phys. and Chem. of Glasses, 5 (1964) 53.

78. W.L.Bragg and W.H.Zachariasen, Z.Krist. 72 (1930) 518.

79. C.Hang, A.Simonov and N.V.Belov, 'Crystal structures of Willemite Zn_2SiO_4 and its Germanium analog Zn_2GeO_4', Soviet Physics-Crystallography, 153 (1970) 387.

80. L.S.Dent Glasser, 'Crystallography and its applications', (1977).

81. Hirsch et al, 'Electron Microscopy of ThinCrystals', p110.

82. S.Wild, P.Grievson, K.H.Jack, 'Special Ceramics', 5 P.Popper (ed), Brit.Ceram.Res.Assoc. (1972).

83. International Tables for X-ray Crystallography (1969).

84. L.Gillot, N.Cowlan, G.E.Bacon, 'A neutron diffraction investigation of some B'sialons', J.Mat.Sc. 16 (1981) 2263.

85. R.C Evans, 'An Introduction to Crystal Chemistry', Cambridge, 2nd Ed. (1966) p69.

86. M.H.Lewis, 'The crystal distortion resulting from long range order in vanadium carbide', Phil.Mag. 31 (1975) 173.

. . .

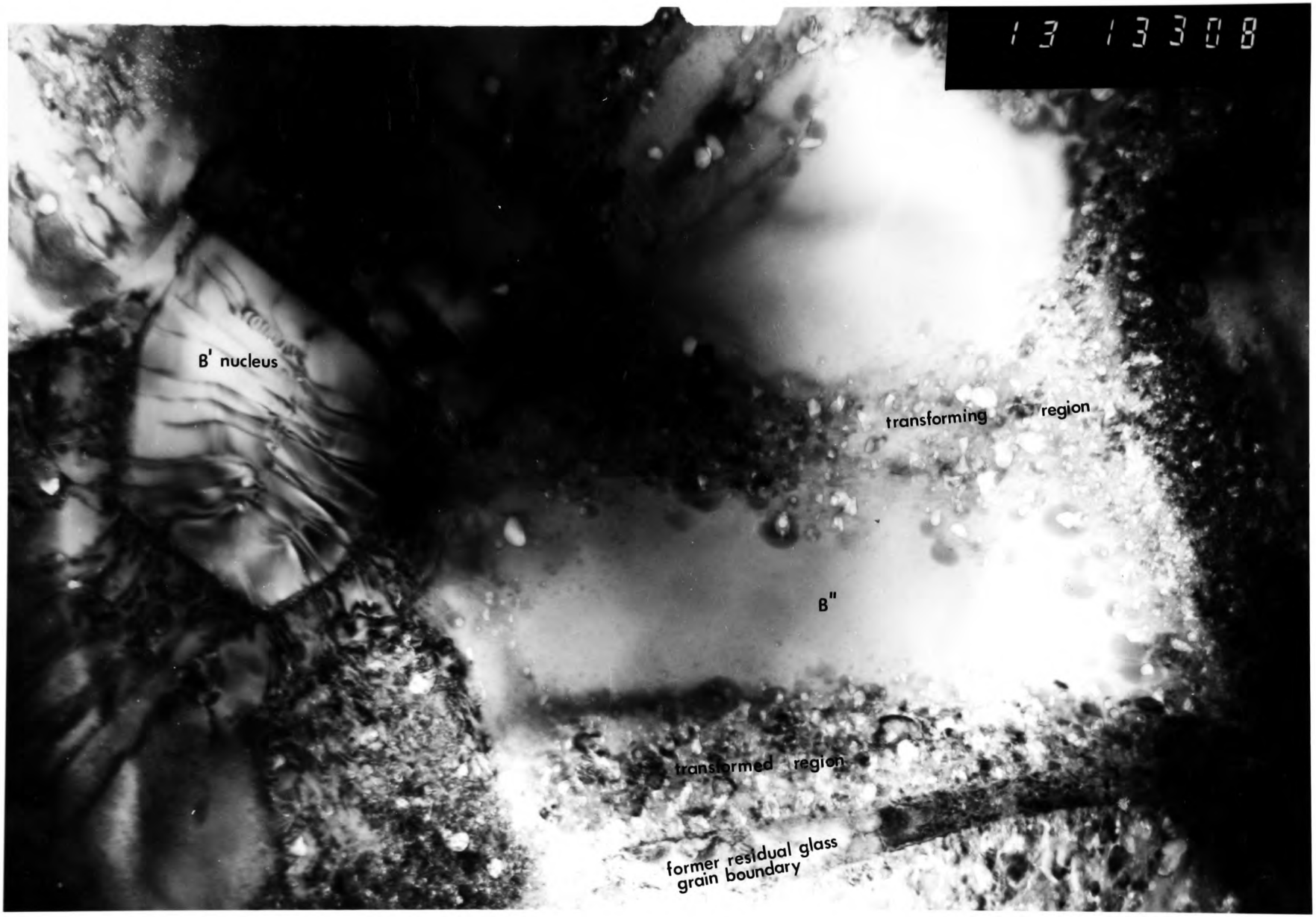
13 13308
B' nucleus
transforming region
B"
transformed region
former residual glass
grain boundary